NUMERICAL MODELING OF PROPELLER TIP FLOWS WITH WAKE SHEET ROLL-UP IN THREE DIMENSIONS

Sangwoo Pyo

DTIC
ELECTE
AUG 2 2 1995
G
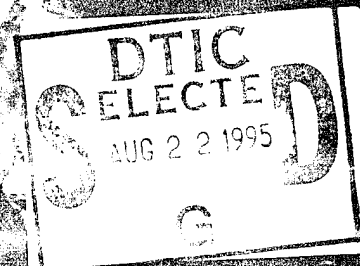
Report 95-6

MASSACHUSETTS INSTITUTE OF TECHNOLOGY
DEPARTMENT OF OCEAN ENGINEERING
CAMBRIDGE, MA 02139

Report No. 95-6

Numerical Modeling of Propeller Tip Flows with
Wake Sheet Roll-up in Three Dimensions

Accesion For	
NTIS CRA&I	☒
DTIC TAB	☐
Unannounced	☐
Justification	
By	
Distribution /	
Availability Codes	
Dist	Avail and / or Special
A-1	

Sangwoo Pyo

July 1995

DTIC QUALITY INSPECTED 3,

19950822 152

REPORT DOCUMENTATION PAGE		READ INSTRUCTIONS BEFORE COMPLETING FORM
1. REPORT NUMBER 95-6	2. GOVT ACCESSION NO.	3. RECIPIENT'S CATALOG NUMBER
4. TITLE *(and Subtitle)* Numerical Modeling of Propeller Tip Flows with Wake Sheet Roll-up in Three Dimensions		5. TYPE OF REPORT & PERIOD COVERED Technical Report
		6. PERFORMING ORG. REPORT NUMBER
7. AUTHOR(s) Sangwoo Pyo		8. CONTRACT OR GRANT NUMBER(s) N00014-95-1-0385
9. PERFORMING ORGANIZATION NAME AND ADDRESS Department of Ocean Engineering Massachusetts Institute of Technology 77 Mass. Ave., Cambridge, MA 02139		10. PROGRAM ELEMENT, PROJECT, TASK AREA & WORK UNIT NUMBERS
11. CONTROLLING OFFICE NAME AND ADDRESS Office of Naval Research 800 North Quincy St. Arlington, VA 22217-5660		12. REPORT DATE July 1995
		13. NUMBER OF PAGES
14. MONITORING AGENCY NAME & ADDRESS*(if different from Controlling Office)*		15. SECURITY CLASS. *(of this report)* Unclassified
		15a. DECLASSIFICATION/DOWNGRADING SCHEDULE

16. DISTRIBUTION STATEMENT *(of this Report)*

Approved for public release; distribution unlimited

17. DISTRIBUTION STATEMENT *(of the abstract entered in Block 20, if different from Report)*

18. SUPPLEMENTARY NOTES

19. KEY WORDS *(Continue on reverse side if necessary and identify by block number)*

Tip Vortex
Wake Sheet Roll-up
Propellers
Cavitation

20. ABSTRACT *(Continue on reverse side if necessary and identify by block number)*

A boundary element method is applied to the prediction of the flow around propeller blades, with emphasis at the tip region. The presented work is divided into three major parts. In the first part, a new panel arrangement, namely the FLow Adapted Grid (FLAG), is proposed. This grid is normal to the blade leading edge outline and adjusted to the force free wake geometry at the trailing edge. The location of the tip vortex detachment

point is determined by an iterative method. The effectiveness and robustness of the flow adapted grid are demonstrated through numerical validation tests and through comparisons with existing experiments. The flow adapted grid is found to improve: (a) the predicted velocity flow field and the pressure distribution at the tip, (b) the convergence of an iterative pressure Kutta condition, and (c) the overall numerical performance of the method and its consistency to lifting surface theory. The second part addresses an algorithm for predicting the three-dimensional vortex sheet roll-up. A higher order panel method, which combines a hyper- boloidal panel geometry with a biquadratic dipole distribution, is used in order to accurately model the highly rolled-up regions. For given radial circulation distributions, the predicted wake shapes are shown to be convergent and consistent to those predicted from other methods. In the final part of this thesis, the flow adapted grid and the three-dimensional wake sheet roll-up algorithm are combined in order to estimate the propeller loading/trailing wake interaction. Predicted forces, circulation distributions and tip vortex trajectories are shown to agree well to those measured in experiments.

Numerical Modeling of Propeller Tip Flows with Wake Sheet Roll-Up in Three Dimensions

by

SANGWOO PYO

B.S., Seoul National University (1986)
M.S., Seoul National University (1988)

Submitted to the Department of Ocean Engineering
in partial fulfillment of the requirements for the degree of
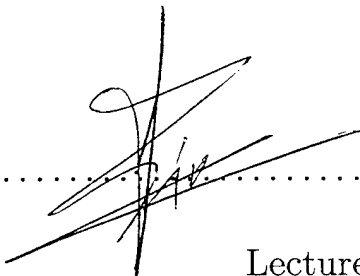
Doctor of Philosophy

at the

MASSACHUSETTS INSTITUTE OF TECHNOLOGY

July 1995

Author ....
Department of Ocean Engineering
July 31, 1995

Certified by...................................
Spyros A. Kinnas
Lecturer and Principal Research Engineer
Thesis Supervisor

Accepted by ....
A. Douglas Carmichael
Chairman, Departmental Committee on Graduate Students

Numerical Modeling of Propeller Tip Flows with Wake Sheet Roll-Up in Three Dimensions

by

Sangwoo Pyo

Submitted to the Department of Ocean Engineering
on July 31, 1995, in partial fulfillment of the
requirements for the degree of
Doctor of Philosophy

Abstract

A boundary element method is applied to the prediction of the flow around propeller blades, with emphasis at the tip region. The presented work is divided into three major parts. In the first part, a new panel arrangement, namely the FLow Adapted Grid (**FLAG**), is proposed. This grid is normal to the blade leading edge outline and adjusted to the force free wake geometry at the trailing edge. The location of the tip vortex detachment point is determined by an iterative method. The effectiveness and robustness of the flow adapted grid are demonstrated through numerical validation tests and through comparisons with existing experiments. The flow adapted grid is found to improve: (a) the predicted velocity flow field and the pressure distribution at the tip, (b) the convergence of an iterative pressure Kutta condition, and (c) the overall numerical performance of the method and its consistency to lifting surface theory. The second part addresses an algorithm for predicting the three-dimensional vortex sheet roll-up. A higher order panel method, which combines a hyperboloidal panel geometry with a biquadratic dipole distribution, is used in order to accurately model the highly rolled-up regions. For given radial circulation distributions, the predicted wake shapes are shown to be convergent and consistent to those predicted from other methods. In the final part of this thesis, the flow adapted grid and the three-dimensional wake sheet roll-up algorithm are combined in order to estimate the propeller loading/trailing wake interaction. Predicted forces, circulation distributions , and tip vortex trajectories are shown to agree well to those measured in experiments.

Thesis Supervisor: Spyros A. Kinnas
Title: Lecturer and Principal Research Engineer

Acknowledgments

including: Dr. David Keenan, Dr. Charles Mazel, Dr. Neal Fine, Dr. Michael Hughes, Dr. Tatsuro Kudo, Ms. Beth Lurie, Mr. Todd Taylor, Mr. Shige Mishima, Mr. Scott Black, Mr. Bill Milewski, Mr. Cedric Savineau, Mr. Wes Brewer, Mr. Bill Ramsey, and Ms. Brabara Smith. I will never forget the cast of propeller nuts.

Finally, I want to express my love to my two kids, Junghwan and Jiyeon (*"annabel"*) and my love and profound gratitude to my wife Sooyeong, and my parents, to whom this thesis is dedicated.

Contents

List of Figures

8

9

List of Tables

NOMENCLATURE

$a_{i,j}$ the velocity induced at i by unit strength dipole at j

A_{max} the highest radial point of the blade

A_{tip} the tip vortex detachment point

AR aspect ratio

$b_{i,j}$ the velocity induced at i by unit strength source at j

c propeller blade chord distribution

C_F propeller blade friction coefficient

C_p pressure coefficient : $= (p - p_\infty)/(1/2)\rho V_s^2$

D propeller diameter

f propeller blade camber distribution

G Green's function; $G(p; q) = 1//bR(p, q)$

J advance coefficient based on ship speed : $= V_s/nD$

J_A the design advance coefficient based on ship speed

K number of blades

K_T thrust coefficient : $= T/\rho n^2 D^4$

K_Q torque coefficient : $= Q/\rho n^2 D^5$

LDV Laser Doppler Velocimeter

n propeller revolutions

$\boldsymbol{n}$ unit normal to blade or wake surface

N_{BLADE} number of blades

N_W number of panels in the wake

N_{PANEL} total number of panels

p pressure on the blade

p_∞ pressure at infinity

P propeller blade pitch distribution

$\tilde{q}(z)$ the conjugate complex velocity

R propeller radius

Re Reynold's number

S_B the blade surface

S_W	the wake surface
$\boldsymbol{U}_{in}$	inflow velocity in the propeller fixed frame
V_s	ship speed
$\boldsymbol{V}_a$	axial velocity
$\boldsymbol{V}_r$	radial velocity
$\boldsymbol{V}_t$	tangential velocity
$\boldsymbol{V}_{TOTAL}$	total velocity on the blade
$W^K_{i,m,l}$	the velocity induced at i by unit strength dipole at (m,l) in the wake on the blade K
x_m	propeller blade rake distribution
(x,y,z)	cartesian coordinate system fixed on propeller
α	hydrofoil angle of attack
α_{ideal}	ideal angle of attack
β	undisturbed flow angle
$|\Delta C_p|_{TE}$	pressure difference at the trailing edge of the blade
η	propeller efficiency: $= (J/2\pi)(K_T/K_Q)$
$\gamma(s,t)$	the strength of the vortex sheet
Γ	the circulation around the blade section
ϕ	perturbation velocity potential
Φ	total velocity potential
ρ	fluid density
τ	propeller blade thickness distribution
$(\tau/c)_{max}$	maximum thickness/chord ratio
θ	propeller blade skew (in degrees)
(ξ,η,ζ)	local coordinate system with a origin at a control point of a panel
BEM	Boundary Element Method
BOG	Blade Orthogonal
FLAG	FLow Adapted Grid
IPK	Iterative Pressure Kutta condition

PSF-2   Propeller blade analysis code in Steady Flow by a vortex lattice method

PSF-10   Propeller blade analysis code in Steady Flow by a potential based panel method

VLM   Vortex Lattice Method

Chapter 1

Introduction

In most marine propeller applications cavitation usually occurs first in the strong vortical region in the vicinity of the blade tip. Inception at the tip may occur either on the blade or in the vortex core (downstream of the blade). Knowing the details of the flow on and/or behind the tip is thus *crucial* in determining cavitation inception. Tip vortex cavitation has been one of the loudest underwater noise sources. Due to this, tip vortex cavitation has been of great interest in naval propeller design. A tip vortex is most likely to cavitate when the blade tip is subject to off-design conditions, due to spatial non-uniformity of the inflow to the propeller, or due to flow inclination. In order to delay tip vortex cavitation inception, designers often unload the circulation distribution at the tip, thus by sacrificing on propeller efficiency. Therefore, in the design and assessment of propulsors for naval applications, it is essential to accurately predict and thus control tip vortex cavitation inception.

1.1 Objectives

The objective of this thesis is to develop a *robust* and *efficient* panel method applicable to general shape lifting surfaces, including propeller blades, with full wake alignment and wake sheet roll-up in three dimensions. The approach is to use a new panel arrangement on the propeller blades to obtain accurate prediction of the pressure distribution at the blade tip. In addition, a higher order panel method and a redis-

cretization scheme in the calculation of wake sheet roll-up are used to obtain more accurate and smoothly rolled-up geometry of the wake sheet. Emphasis is placed on obtaining accurate prediction of the tip vortex trajectory, the geometry of the wake sheet, and the pressure distribution at the tip. It is expected that such a solution will improve the prediction of tip vortex cavitation inception.

1.2 Previous Research

1.2.1 Tip Vortex Cavitation

The primary methods for predicting tip vortex cavitation inception are variations of the method by McCormick [51],[50]. He proposes a semi-empirical approach in which he considers that the minimum pressure depends on the near-tip loading and identifies the important role of the foil tip boundary layer. He then postulates a power law relation, $\delta \sim Re^{-r}$, between the boundary layer thickness δ and the local Reynold's number Re. The constant factor multiplying this scaling law as well as the exponent are geometry dependent and thus the method can provide predictions only for geometries which are close to those that have been tested in either model or full scale. More recently, from LDV measurements in the vicinity of the tip vortex for several planar wing configurations, at different tunnel facilities and flow conditions, Fruman et al. [15] have shown that the velocity field close to the core of the vortex depends on two parameters; (1) the strength of the tip vortex along its trajectory and (2) the radius of the vortex core. Having these parameters, the value of the minimum pressure inside the vortex core and its location along the vortex can be readily determined. The corresponding pressure coefficient should then be equal to the negative value of the cavitation number at inception. Recent attempts by Dupont and Cerrutti [9] to apply Reynolds Averaged Navier-Stokes solvers to the tip vortex flow have led to poor predictions of the minimum pressure in the vortex core, mainly due to gross overprediction of the size of the vortex viscous core . On the other hand, panel methods have been found to be useful in determining the minimum pressure

19

coefficient at the blade tip, which then can be correlated with the cavitation number at tip vortex cavitation inception. It is believed that a *robust* panel method, with full wake alignment , will not only improve the accuracy of the predicted pressure distributions at the blade tip, but also will provide the foundation for predicting the tip vortex evolution which will ultimately lead to more reliable estimates of tip vortex cavitation inception.

1.2.2 The Panel Method

Panel or Boundary Element methods(BEM) have been applied for the analysis of propeller flows. This method is well advanced and has been extensively described by Hess and Valarezo [20], Lee [42], Kerwin et al. [33] and Hoshino [23]. These methods employed a potential or a velocity based formulation. The investigation of different panel methods by Lee [42] showed that the perturbation potential based panel method is the best for propeller applications.

A perturbation potential based Boundary Element Method, including the presence of the hub and duct, was developed at MIT by Kerwin et al. [33] and Lee [42]. This method was a low-order BEM based on Green's formula with respect to the perturbation potential. The method discretized the propeller surface and wake with planar quadrilateral panels and constant strength sources and dipoles were distributed on the panels. The panel method has been applied successfully for the hydrodynamic analysis of marine propellers (Lee [42]). In most application, the BEM has been found to predict spanwise circulation distributions which are *consistent* to those predicted from Vortex Lattice Method(VLM) (Hsin [24]). This means that the circulation distributions predicted by BEM for lifting surfaces with thickness, smoothly (often linearly with thickness) extrapolate to the circulation distribution predicted by VLM for the same lifting surface with zero thickness. When this method is applied to a wide circular tip propeller, inaccurate solutions are obtained and an iterative pressure Kutta condition(Kerwin et al. [33]) has been found to diverge. Most importantly, the prediction of the pressure distribution in the tip region has been found to be inaccurate. The correct prediction of the pressure distribution is important not only

for the thrust and torque calculations by integration of the pressure distribution on the blade surface, but also for the cavitation inception estimation. A grid oriented along constant radii, namely the *conventional grid*, has previously been employed by the BEM. This grid arrangement results in high aspect ratio of the panels at the propeller tip. A blade orthogonal grid (BOG), which is orthogonal both at the leading edge and the trailing edge, was developed by Hsin et al. [25] in order to improve the resolution and to reduce panel distortion and aspect ratio near the tip. The blade orthogonal grid was found to improve the convergence of the computed pressure distribution at the tip, and consequently also the convergence of the iterative pressure Kutta condition (Hsin et al. [25]). Nevertheless, when the blade orthogonal grid was applied to lifting surfaces and propellers with wide circular tips, it was found that the circulation distribution behaves non-physically at the tip. To avoid this non-physical behavior of the method at the tip, the **FLow Adapted Grid** was introduced by Kinnas et al. [36], which is orthogonal at the leading edge and aligned with the resulting mean flow at the trailing edge. Pyo and Kinnas [64] showed that this grid improved the convergence of IPK condition and the behavior at the tip of propeller blades.

The Kutta condition may be enforced numerically via the Morino condition [59]. This condition requires that the dipole strength at the trailing edge in the wake to be equal to the difference of the potentials at the trailing edge panels on the blade. Lee [42] incorporated a correction to the Morino condition in two dimensions by applying the Kutta condition at the exact location of the trailing edge. Application of the Morino condition in three dimensions does not always guarantee equality of the resulting pressures at the trailing edge. An iterative pressure Kutta condition based on Newton-Rapson method was introduced by Kerwin et. al [33] and extended to unsteady propeller flows by Hsin [24], and Kinnas and Hsin [35].

The geometry of the trailing wake behind propeller blades was first calculated by Cummings [8], who determined the wake geometry by using a two-dimensional time domain approach in which the body effect was not included. In the BEM, the geometry of the trailing wake sheet is calculated via the lifting surface method of Greeley

21

and Kerwin [16] in an indirect way, where the geometry was determined from the requirement that the trailing vorticity at the trailing edge and far downstream should be aligned with the local flow. Since the local flow depended on the trailing wake geometry in a nonlinear way, an iterative procedure was employed. In the method of Greeley and Kerwin [16] the effects of coupling between the thickness and loading and the wake sheet roll-up were ignored. In addition the radial contraction and the ultimate radius of the trailing wake were assumed to be given from experiments. In summary, this method only included axial and circumferential velocities at the trailing edge and the ultimate wake, and thus suppressed the effect of wake sheet roll-up.

1.2.3 Vortex Sheet Roll-Up

In the past there have been a large number of attempts to model the vortex sheet motion by replacing the continuous vortex sheet with a finite number of discrete vortices or alternatively, by replacing the dipole sheet with segments carrying a piecewise constant dipole distribution.

Rosenhead [66] was the first to attempt this approach with an analysis of the nonlinear Kelvin-Helmholtz instability in a two-dimensional vortex sheet of constant strength. Westwater [74] first applied the discrete vortex method to the problem of vortex sheet roll-up behind an elliptically loaded wing. Attempts to improve Westwater's results by increasing the number of vortices representing the vortex sheet have not been successful. It appeared that this approach inevitably led to chaotic motion in the region of the tip vortex, which resulted in loss of the identity of the vortex sheet. Different approaches have been attempted to desingularize the solution. Chorin and Bernard [7] and Kuwahara and Takami [40] introduced a finite core model for the vortices, in which the velocity remains finite. Moore [56] used a process of amalgamation in which the vortices are combined when they approach each other too closely or when they have to represent high curvature regions in a spiraling sheet. Maskew[46] employed the sub-vortex technique. Despite all these improvements, the discrete vortex representation resulted inevitably in numerical instabilities when the

number of vortices was increased or the core radius was decreased. In the case of wing tip vortices, the method of rediscretization by Fink and Soh [14] has been more successful in obtaining smooth vortex sheet behavior over long periods than have been reported previously. However, recent investigations by Baker [4] on the stability of the rediscretization method for the case of double-branched spiraling vortex sheets demonstrated that this method eventually ended in chaos as well. As an alternative approach, Baker [3] suggested cloud-in-cell method. In this method, the velocity field due to the discrete vortices was computed by solving Poisson's equation for the stream function due to a grid-dependent region of distributed vorticity in the two dimensional plane. The main disadvantages of this method are that the method and its fine-scale behavior are sensitive to the size of mesh , the surface boundary conditions, the number of vortices and the time-step, as noted by Murman and Stremel [60]. From those attempts, it appeared that the discrete vortex method was not adequate to compute smooth vortex sheet roll-up reliably.

On the other hand, the use of dipole distributions for two and three dimensional attached flows is well advanced and has been extensively described in the past by Hess [19] and Johnson [28]. In its most general form, the body is represented by sources and dipoles and the kinematic boundary condition is applied on the body. Across the wake sheet the normal velocity is continuous but the tangential velocity is discontinuous by a "jump" corresponding to the strength of the vorticity sheet. Thus, the wake sheet can also be expressed via a distribution of dipoles. A complete description of this method was presented by Maskew [47]. Hoeijmakers et al. [22] developed high order panel methods based on the slender body approximation. In general, the panel methods produce smoother vortex sheets than those of the discrete vortex models of Maskew and Rao [48] and Fink and Soh [13]. A number of fully three dimensional flow models have been developed for the prediction of wake roll-up in order to overcome the limitations of the slender body approximation. The most well known methods among the high order panel methods are the Boeing's LEV-Model by Johnson et al. [29] and the VORSEP-Model by Hoeijmakers [22]. The comparison with experiments has been good to encouraging as far as the overall accuracy of the position of the

vortices is concerned. The local accuracy depended on the shape of the wing, angle of attack, number of panels and the type of smoothing applied. The calculated pressure distributions on the body compared reasonably well with those measured by Hummel and Redeker[26]. The only disadvantage of these methods is that an initial geometry of the vortex sheet had to be assumed or deduced from analytical solutions.

Recently, Reynolds-averaged Navier-Stokes (RANS) methods have been developed with an assumption that the flow at an infinitesimally small distance upstream is conically similar, which might be a valid approximation for viscous flows that vary slowly in the streamwise direction. Lee [43] applied this method to predict the roll-up of the leading edge vortex on delta wings. Eça et al. [11] solved the parabolized Navier-Stokes equations on elliptic wings. Stern et al. [71] applied their RANS solver on propeller blades. These methods have demonstrated capability to simulate *qualitatively* the physics of viscous dominated processes such as flows inside the core and vortex breakdown. However, the current status of turbulence and transition modeling is not yet adequate so that *quantitative* predictions(especially for the pressure distribution inside the vortex core) based on RANS are feasible.

There are numerous other applications which do not fit conveniently into the above categories. McCune and Tavares [53] solved the two-dimensional unsteady and large amplitude delta wing motion problem with leading edge separation. McCracken and Peskin [52] combined a finite-difference method with the vortex blob algorithm. McAlister and Carr [49] solved unsteady vortical flows with dynamic stall around an oscillating wing.

1.2.4 The Present Method

In the present method, a potential based boundary element method is applied for the analysis of propeller flows. The flow adapted grid (FLAG) is developed in order to solve the convergence problem for the typical grid arrangements and to improve the tip flow behavior. The geometry of the trailing wake is decided directly from the panel method without any assumption and the vortex sheet roll-up is included in the FLAG. In order to model the wake sheet roll-up in three dimensions, bi-quadratic

strength dipole distributions and hyperboloidal panel geometry are used. Throughout the numerical calculation, rediscretization is applied as a smoothing scheme.

The consistency and convergence of the results from the numerical method are validated first, and then the method is applied to several planar wing and propeller blade geometries and the numerical results are compared with existing experimental data.

Chapter 2

Boundary Element Method

2.1 Formulation

The fundamentals of the BEM are described by Kerwin and Kinnas [33], Lee [42], and Hsin et al. [25] and only a brief description will be given in this section. The method is based on the classical Green's third identity (applied on the body surface S_B):

$$
\begin{aligned}
2\pi\phi &= \int_{S_B} \left[\phi \frac{\partial G}{\partial n} - G \frac{\partial \phi}{\partial n} \right] dS \\
&+ \int_{S_W} \Delta\phi \frac{\partial \phi}{\partial n} dS
\end{aligned}
\tag{2.1}
$$

where the Green's function G is the unit strength source in three dimensions; ϕ is the perturbation potential; S_W is the trailing wake surface as shown in Figure 2-1.

The BEM implementation involves:

- Constant strength dipole and source panels on the blade and in the wake.

- Hyperboloidal panel geometry (critical for highly twisted body geometries).

- An Iterative Pressure Kutta (IPK) condition which determines the appropriate strength $\Delta\phi$ in the wake in order for the pressure jump across the trailing edge

26

to be equal to zero at all spanwise locations.

Two panel arrangements have been used in the past: the conventional grid by Kerwin and Kinnas [33] and Lee [42] and the blade orthogonal grid (BOG) by Hsin et al. [25].
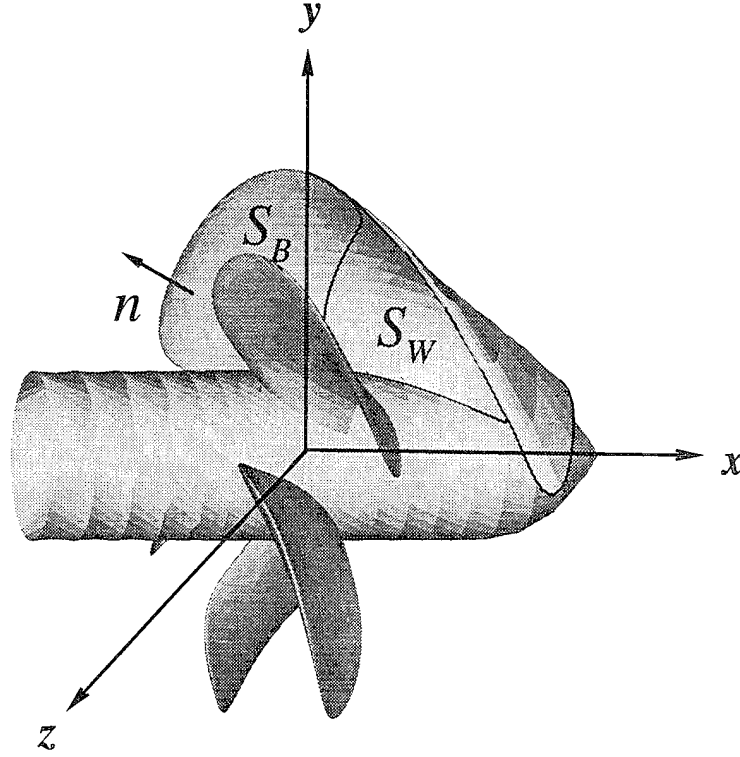
Figure 2-1: Global coordinate system fixed on the propeller blade.

The former of the two grids and the proposed flow adapted grid (FLAG) will be described in the next sections.

2.2   The conventional grid

The conventional grid has been used traditionally for vortex-lattice applications on 3-D wings and propeller blades by Lan [41] and Greeley and Kerwin [16]. It has also been called the "constant radii" grid. The panel edges are located along the

intersections of the blade with cylinders concentric with the axis of propeller rotation. The geometry of the trailing wake is found by following the Greeley and Kerwin [16] procedure :

- The tip vortex trajectory starts on the blade at the highest radial position.

- The wake gridlines are aligned with the axial and tangential velocities in the wake.
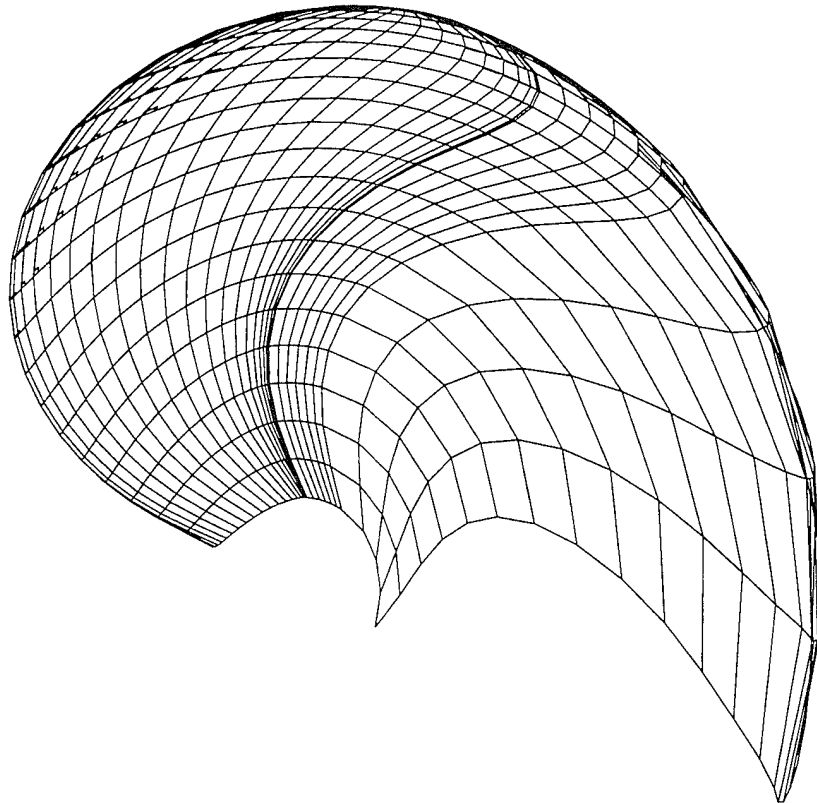
Figure 2-2: The conventional grid on a propeller blade and its trailing wake.

- The radial contraction of the wake at the tip is an input parameter, given from experimental information (usually equal to 30 degrees).

- The radius of the ultimate wake geometry is also an input parameter, given from experimental information (usually equal to $0.83R$).

The corresponding panel arrangement for one of the three propeller blades (with 40 chordwise and 20 spanwise panels) is shown in Figure 2-2. The spanwise circulation distribution predicted by applying the BEM on the described grid for propeller N4119 [27] is shown in Figure 2-3. In this particular case it took 14 iterations for the IPK condition to converge ($|\Delta C_p|_{TE} \leq 10^{-3}$).
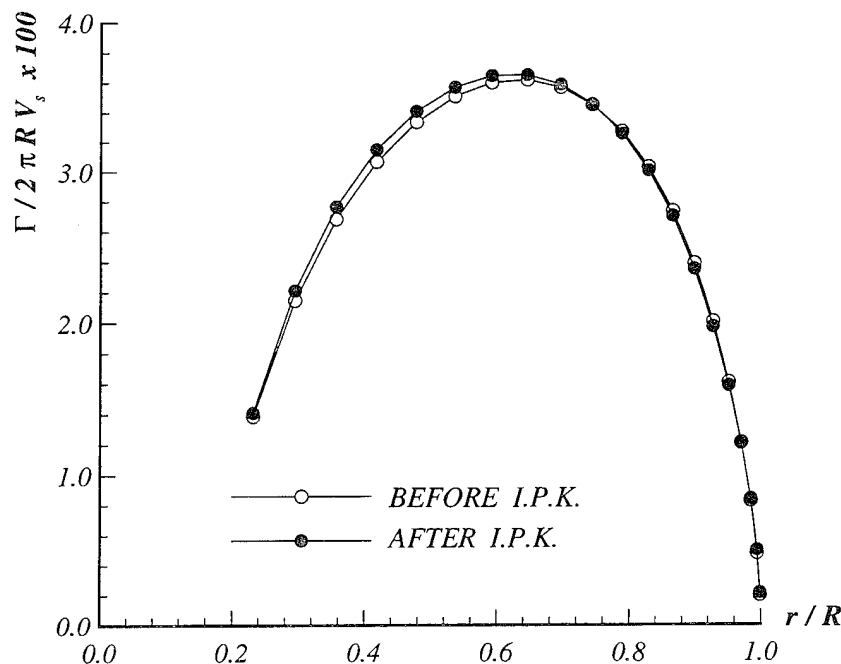
Figure 2-3: Circulation distribution on the propeller N4119; $J = 0.833$. Predicted by applying the BEM on the conventional grid; before and after applying the Iterative Pressure Kutta condition.

The circulation distribution "before" the IPK corresponds to the Morino [59] Kutta condition in which the dipole strength in the wake is taken equal to the difference of the potentials at the panels at the two sides of the trailing edge. This condition has been found to produce pressure distributions which do not match at

the trailing edge, especially in the vicinity of the tip. The circulation distribution "after" the IPK corresponds to the modified wake dipole strength which ensures pressure equality at the trailing edge. This panel arrangement has been successful for conventional geometries. However, when this grid is applied to extreme geometries such as a highly skewed propeller and a propeller with large tip chord, inaccurate and divergent solutions are obtained.
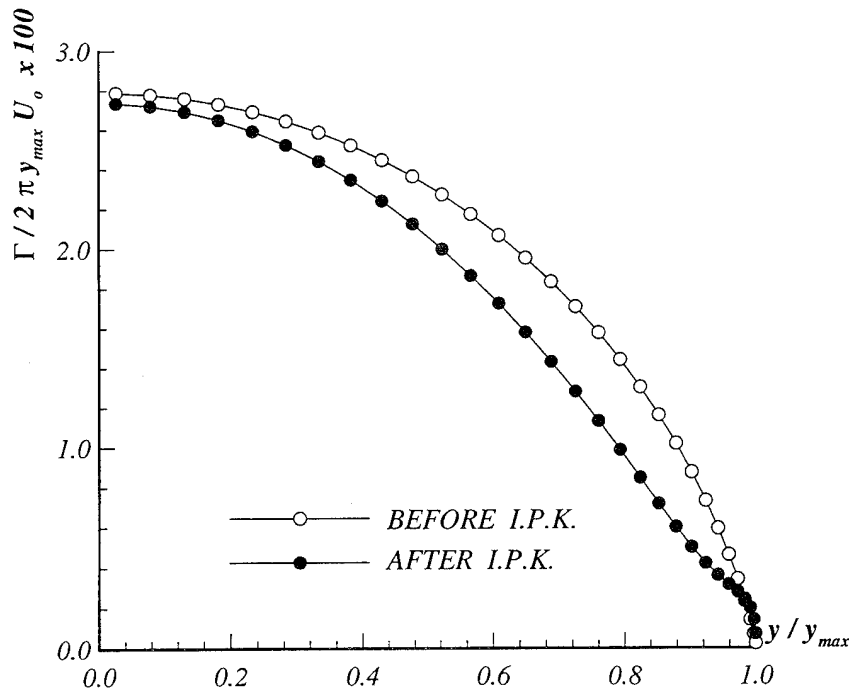
Figure 2-4: Circulation distribution on a circular wing planform hydrofoil; $\alpha = 5.73^o$, Modified NACA66 thickness distribution with $[\tau/c]_{max} = 0.2$. Predicted by applying the BEM on the conventional grid ; before and after applying the IPK condition.

This is because the conventional grid arrangement results in high panel aspect ratios and highly skewed and twisted panels at the propeller tip. For a circular wing, which has extremely large tip chord, the circulation distribution is show in Figure

30

2-4. Notice the large difference over the span between the circulation distributions before and after IPK condition. Especially near the tip the *peculiar* behavior of the circulation distribution after IPK condition. In addition, for a propeller with large tip chord , the pressure distributions at three spanwise locations and the mean velocity vectors at the first control points in the wake along the trailing edge are shown in Figures 2-5 and 2-6, respectively.
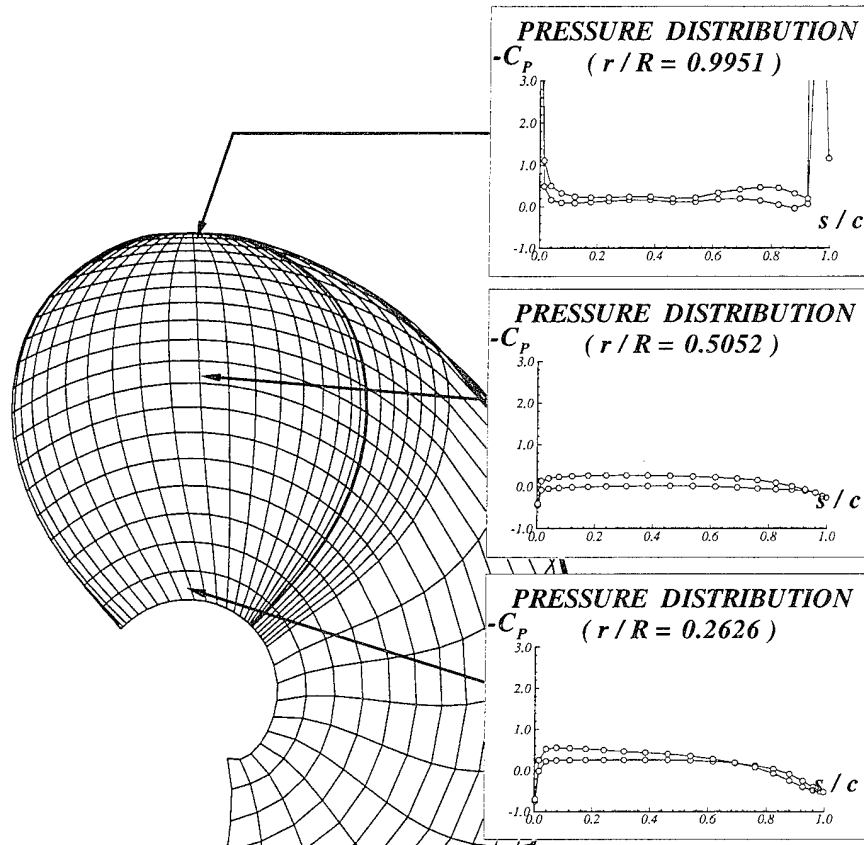
Figure 2-5: Pressure coefficients predicted from BEM applied on the conventional grid (after IPK condition); propeller N4119, J=0.833.

The velocity vectors are computed from the superposition of the inflow velocity, U_{in}, and the velocities induced by all dipoles and sources on the blades and all dipoles in the wakes of the blades. Notice the singular behavior of the pressures and the mean

31

velocity vectors in the vicinity of the tip.

2.3   The blade orthogonal grid

To improve the resolution and to reduce panel distortion near the tip, the blade orthogonal grid was introduced by Hsin et al. [25].
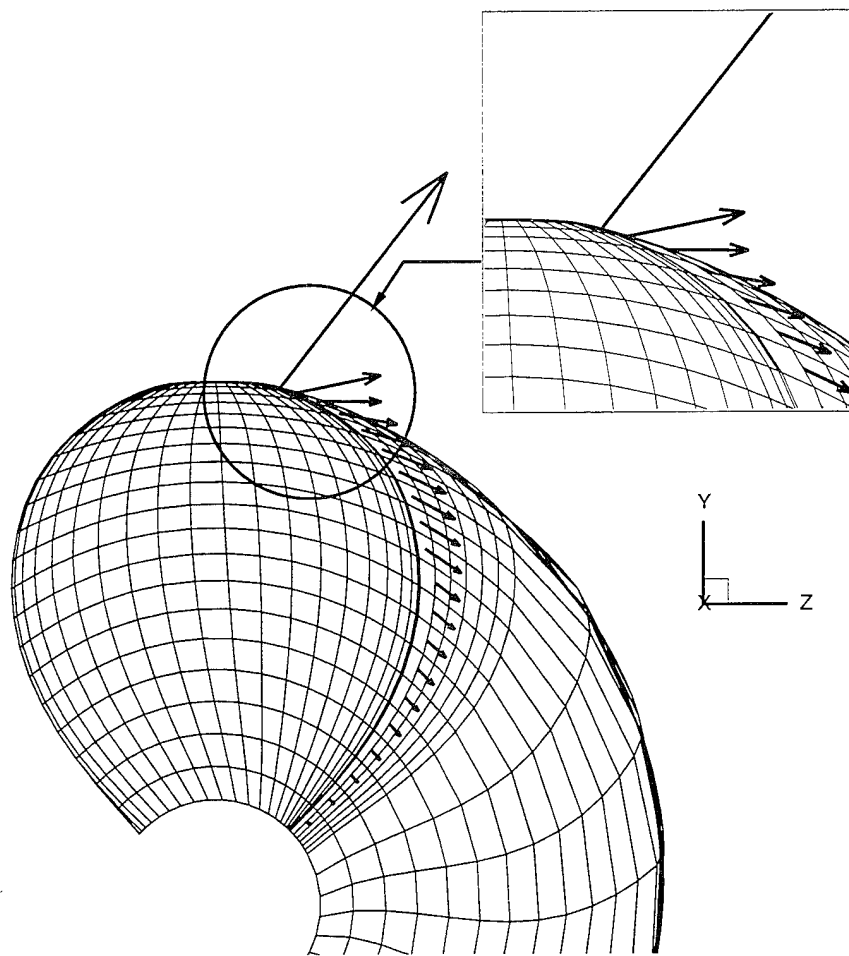
Figure 2-6: Mean velocity vectors along the trailing edge of the propeller N4119 ; $J = 0.833$. Predicted by applying the BEM on the conventional grid.

In this grid, the expanded blade outline is assumed to be given as a cubic B-spline curve. Then, the arclength along this outline is expressed as a function of parametric

variable, which is zero at the intersection of the leading edge with the hub and reaches to the maximum value at the intersection of the trailing edge with the hub. With the tip point defined, the outline of the blade is divided. Finally, the divided points are connected by cubic B-spline curves with four vertices, by putting the second and third interior vertices along the normals to the edge. The orthogonality of the curves can be obtained. Figure 2-7 shows a simple example of this grid for a circular planform wing. One can see that the grid lines are orthogonal to the outline of the wing and the panel aspect ratios remain small near the tip.
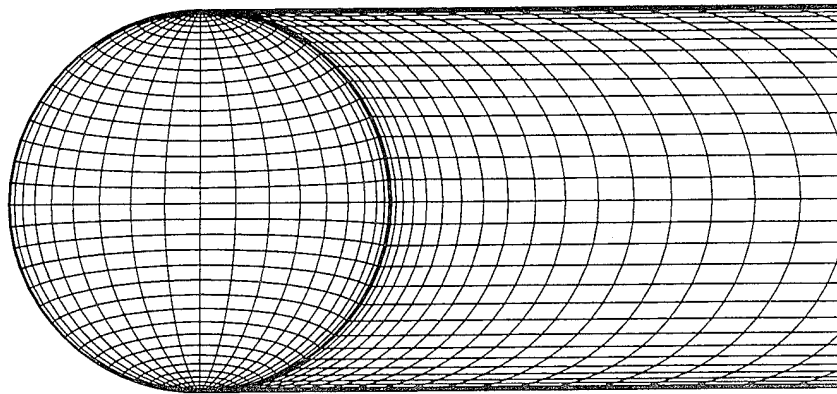
Figure 2-7: The blade orthogonal grid on a circular planform hydrofoil and its trailing wake.

When the BEM was applied on this grid, it is found that the surface pressures at the tips of non-lifting bodies were computed more accurately than when the BEM was applied on the conventional grid. This is the consequence of concentrating more panels at the tip as well as of producing much less distorted panels (of which the sides are of comparable size and almost orthogonal to each other) than the conventional grid. The blade orthogonal grid is also found to improve the convergence of the IPK condition in the case of lifting hydrofoils or propeller blades. This is a direct consequence

of the fact that the trailing edge pressures (which drive the IPK condition) at the tips were computed more accurately now than in the case of the conventional grid. The circulation distributions for the circular planform wing are shown in Figure 2-8. Notice that the difference between the circulation distributions before and after the IPK condition is now larger than that for the conventional grid. An explanation for this will be given in Appendix A.
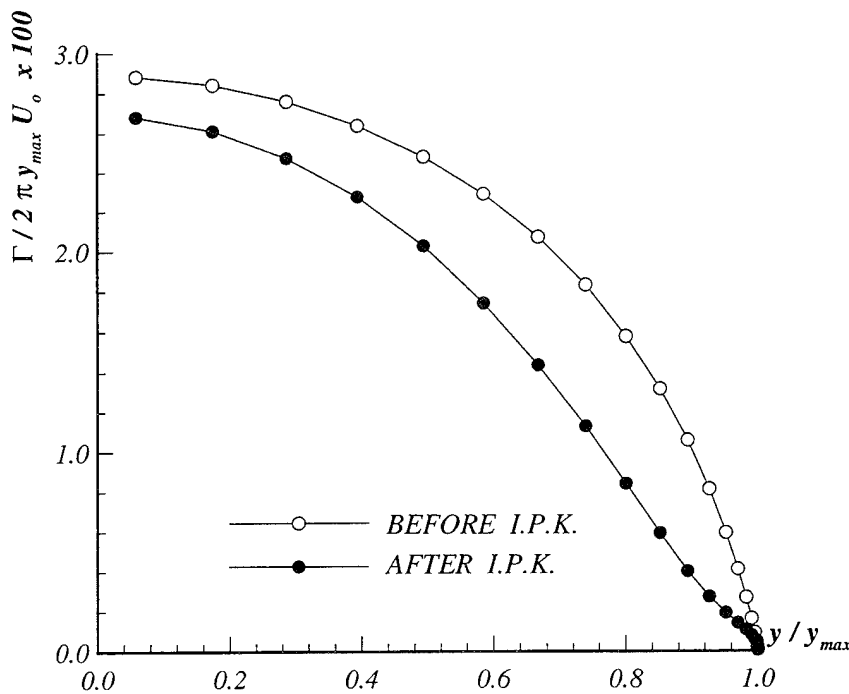
Figure 2-8: Circulation distribution on a circular planform hydrofoil; $[\tau/c]_{max} = 0.2$, $\alpha = 5.73^\circ$. Predicted by applying the BEM on the blade orthogonal grid; before and after applying the IPK condition.

Also notice that the circulation distribution after the IPK condition is very similar (also "peculiar") to that in the case of the conventional grid. The results shown in this and the previous section indicate that there must be something fundamentally

wrong either with the implementation of the IPK condition and/or with the utilized grids.

2.4 The flow adapted grid (FLAG)

As explained in Appendix A, the difference in circulations between before and after IPK condition will be decreased if the grid on the blade is aligned with the mean velocity vector at the trailing edge. This means that if the grids on the blade and in the wake are aligned with the mean velocity at the trailing edge, the number of iteration for the IPK condition will be decreased and the solution will converge after fewer iterations. From this examination, the new grid arrangement, namely the "FLow Adapted Grid (**FLAG**)", is developed. The flow adapted grid will be introduced and applied on three dimensional wings and propellers in this section.

2.4.1 Construction of the grid

The flow adapted grid is constructed by satisfying the following characteristics:

- The grid on the blade is adapted to the resulting flow in the wake. This decreases the number of iterations for the IPK condition and the difference in the circulation distributions between before and after IPK condition as explained in Appendix A.

- The grid on the blade is smoothly connected to that in the wake at the trailing edge.

- The grid on the blade is orthogonal at the leading edge. This results in improvement in resolution near the tip and more accurate pressure predictions at the leading edge.

- The grid on the blade includes the effect of the resulting flow on the location of the tip vortex detachment point (also called the "computational tip").

The procedure for implementing the flow adapted grid on propeller blades consists of the following steps (also shown in the flow diagram of Figure 2-9).

```
                        ┌─────────────┐
                        │    START    │
                        └─────────────┘
                               │
                               ▼
              ┌──────────────────────────────────────┐
              │             READ INPUT               │
              │ ( BLADE GEOMETRY , WAKE PARAMETERS ,  │
              │          NUMBER OF BLADES )           │
              └──────────────────────────────────────┘
                               │
                               ▼
              ┌──────────────────────────────────────┐
              │           RUN PANEL CODE             │
              │        WITH CONVENTIONAL GRID        │
              └──────────────────────────────────────┘
                               │
                               ▼
              ┌──────────────────────────────────────┐
              │     COMPUTE RADIAL INDUCED VEL.      │◄───┐
              │     AT T.E. & GET THE ANGLE θ        │    │
              └──────────────────────────────────────┘    │
                               │                           │
                               ▼                           │
              ┌──────────────────────────────────────┐    │
              │     FIND THE POSITION OF THE TIP      │    │
              └──────────────────────────────────────┘    │
                               │                           │
                               ▼                           │
              ┌──────────────────────────────────────┐    │
              │           CONSTRUCT FLAG             │    │
              └──────────────────────────────────────┘    │
                               │                           │
                               ▼                           │
                        ◇ CONVERGE ? ◇ ──────────────────┘
                               │
                               ▼
              ┌──────────────────────────────────────┐
              │       RUN PANEL CODE WITH FLAG        │
              └──────────────────────────────────────┘
```
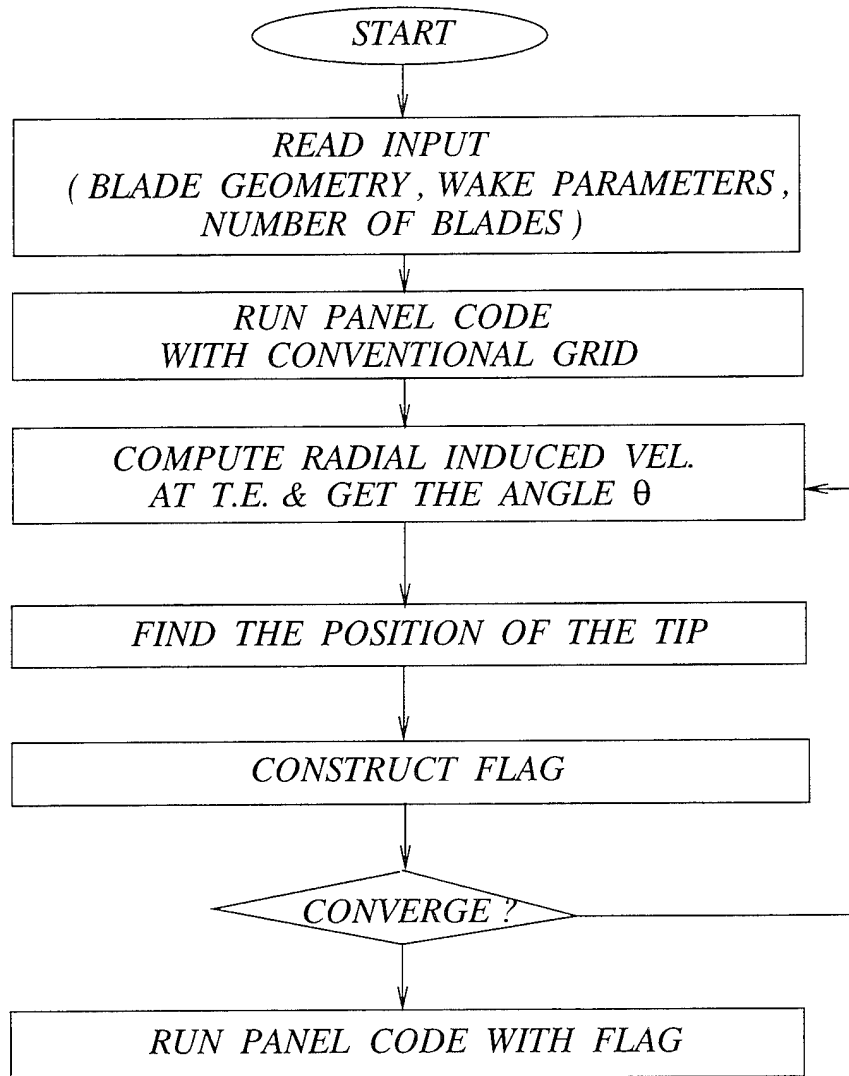
Figure 2-9: Flow diagram for construction of FLAG.

STEP 1

- Solve the boundary value problem by applying the panel method with the conventional grid and straight wake for the wings and purely helicoidal wake for

36

the propellers (no contraction). Determine the dipole and/or source strengths on the blade, hub and wake panels.

- Compute the total mean velocity vectors, V^M_{WAKE}, at the first control points in the wake at each radius, via the following superposition, also shown in Figure 2-10:
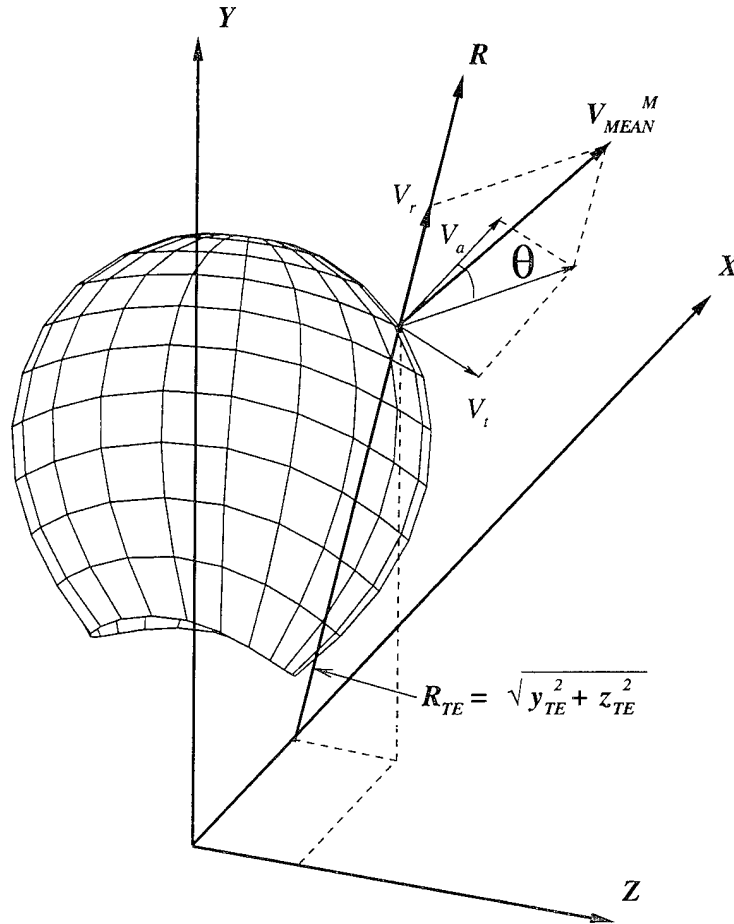
Figure 2-10: The contraction angle of the blade gridlines along the trailing edge.

$$V^M_{WAKE} = V_t + V_a + V_r + U_{in} \qquad (2.2)$$

where V_t, V_a, V_r are the tangential(circumferential), axial and radial velocities, respectively; U_{in} is the inflow velocity in the propeller fixed frame.

The velocities V_t and V_a are computed by using a method similar to that of Greeley and Kerwin [16], where a tip vortex with finite core is utilized. The core radius and the radial contraction angle of the tip vortex at the blade are given from experimental information. On the other hand, V_r is computed by using the superposition of the radial velocities induced by the blade, hub and wake singularities resulting from applying the panel method on the conventional grid.
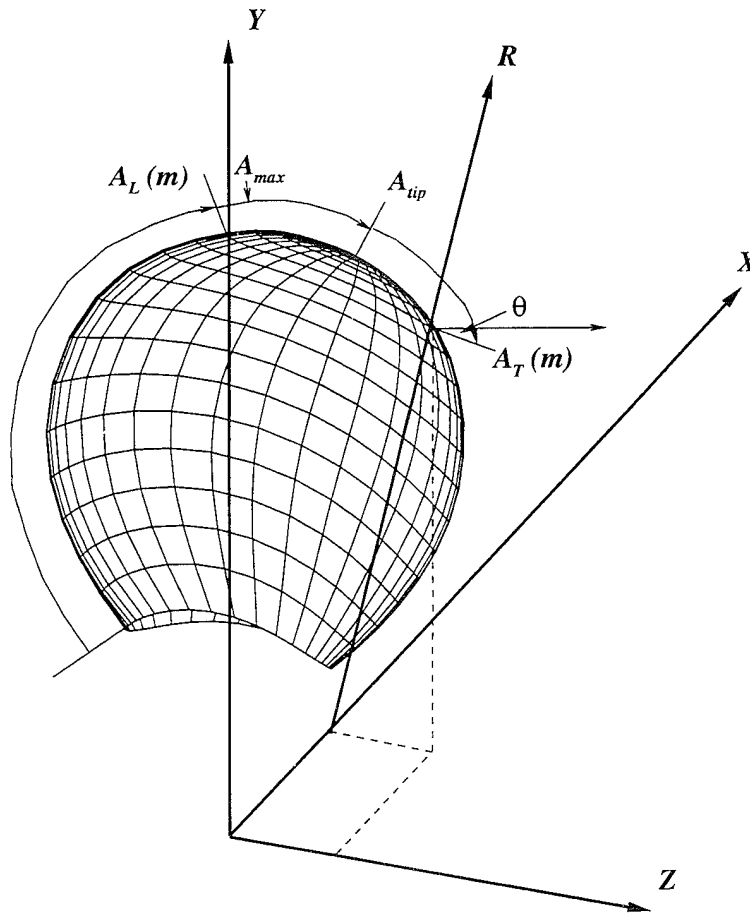
Figure 2-11: The geometry of grid lines. The tip vortex detachment point, A_{tip}, is taken downstream of the actual tip due to the contraction of the wake.

STEP 2

- Calculate the contraction angle, θ, of the gridlines along the blade trailing edge by using the following equation, as shown in Figure2-10.

$$\theta = \sin^{-1}\left(\frac{|V_r|}{\left|V_{WAKE}^M\right|}\right) \tag{2.3}$$

with V_{WAKE}^M and V_r computed in STEP 1.

- Find the location of the tip vortex detachment point (also called the "computational" tip), A_{tip}, shown in Figure 2-11. At first, the tip is determined by searching among the streamlines (corresponding to V_{WAKE}^M) for the one which starts at the largest blade radial location and *does not* intersect the propeller blade. Due to the contraction of the wake, the location of the computational tip will be downstream from the actual tip. The details of the location of the tip will be discussed in the following chapters.

- Construct the flow adapted grid on the blade. Having determined the location of the tip vortex detachment point, A_{tip}, the grid on the blade is determined, by modifying the algorithm on which the blade orthogonal grid was based, as follows:

First, the arclengths from the hub to the tip along the blade leading edge and trailing edge are divided into M half-cosine intervals, with M being the number of "spanwise" panels as shown in Figure 2-11. The corresponding arclengths are given as

$$
\begin{aligned}
a_{le}(m) &= A_{tip}\cos\beta_m \\
a_{te}(m) &= A_{max} - (A_{max} - A_{tip})\cos\beta_m
\end{aligned}
$$

$$\text{for} \quad m = 1, 2, \cdots, M$$

where $a_{le}(m)$, $a_{te}(m)$ are arc length from the leading edge of the hub to $A_L(m)$ and from the trailing edge of the hub to $A_T(m)$, respectively, with β_m defined as

$$\beta_m = \frac{\pi}{2}\left(1 - \frac{m-1}{M}\right) \tag{2.4}$$
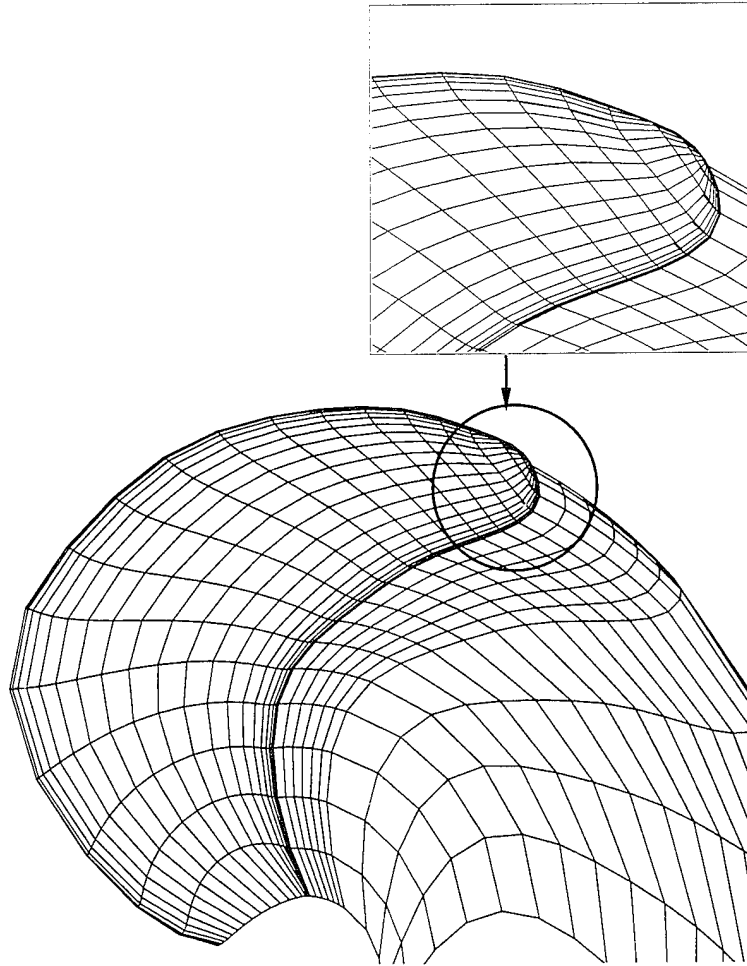
Figure 2-12: FLow Adapted Grid on N4990 propeller blade;$N = 40$, $M = 20.J = 1.270$.

In the case of the blade orthogonal grid, each $A_L(m)$ is connected with $A_T(m)$ via B-spline curves with four vertices which are normal to the blade outline. In the present case, the grid lines are still normal to the blade outline at the leading edge, but now they form an angle at the trailing edge, which is equal to the corresponding wake contraction angle θ, defined earlier. The arcs of these

grid lines are then divided into $N/2$ full-cosine spaced intervals, with N being the number of "chordwise" panels.
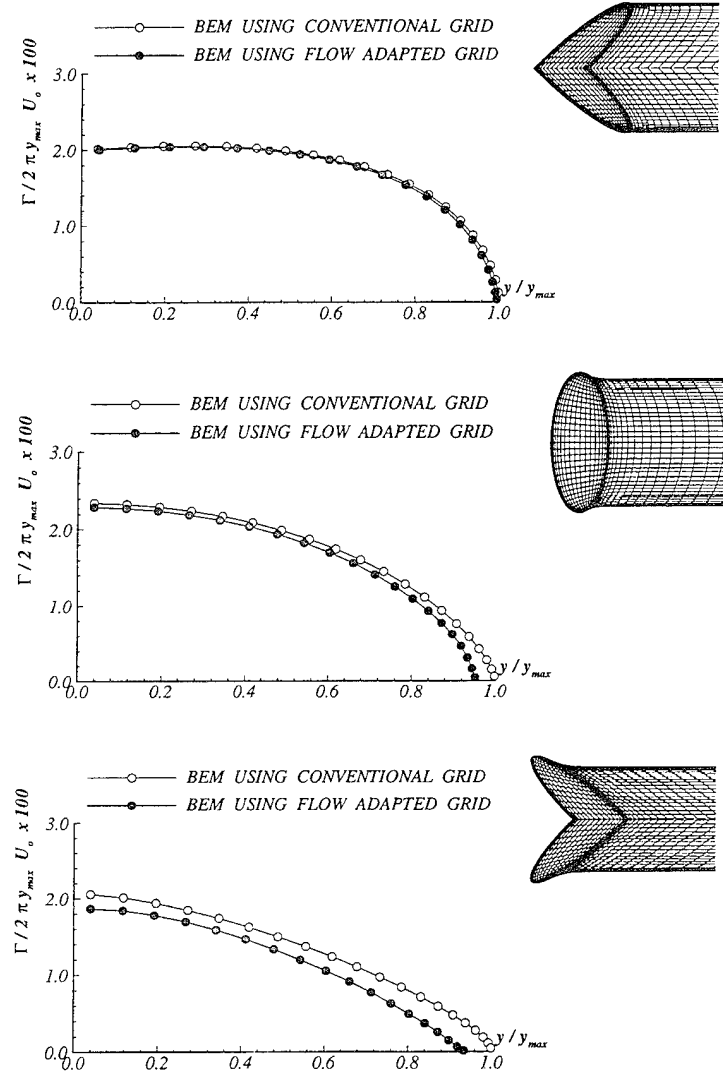
Figure 2-13: Effect of wake geometry on circulation predicted by BEM for three hydrofoils with elliptic chord distribution along the span; $[\tau/c]_{max} = 0.2$, $\alpha = 5.73^o$, aspect ratio AR=3. 45° backward sweep (top) no sweep (middle) 45° forward sweep (bottom). The corresponding flow adapted grids are also shown. Contraction of wake is approximated with that due to wing thickness effect.

The grid on both sides of the propeller blade is then determined by moving the grid of the blade normal to the three dimensional blade camber surface by an amount equal to $\pm t/2$.

- Construct the new trailing wake grid based on the contraction angle, θ, at the tip. The ultimate wake geometry is kept the same to that of the conventional grid.
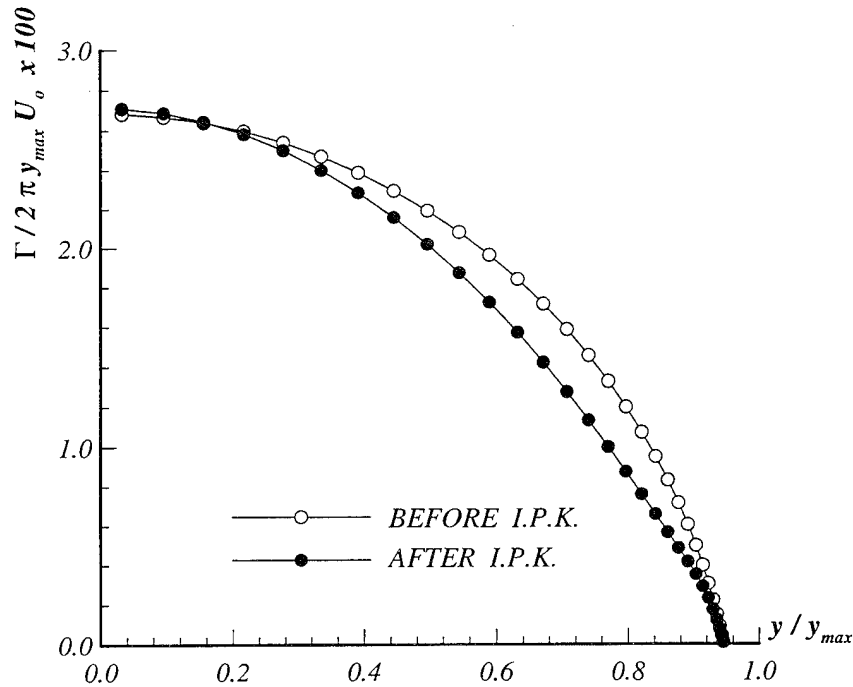
Figure 2-14: Circulation distribution on a circular planform hydrofoil; $[\tau/c]_{max} = 0.2$, $\alpha = 5.73^o$. Predicted by applying the BEM on the flow adapted grid; before and after applying the IPK condition.

STEP 3

- Apply the panel method on the FLAG which was generated in STEP 2. Determine the perturbation potential distribution and calculate the contraction angle at the trailing edge.

Repeat STEPS 2 and 3 until the contraction angle is converged. Usually 2 or 3 iterations are enough. Finally, calculate spanwise circulation distribution, pressure coefficient and thrust/torque on the blade. This grid for propeller N4990 is shown in Figure 2-12. This iterative procedure for determining FLAG has been applied for several wings and propellers and the results will be shown in the next section.
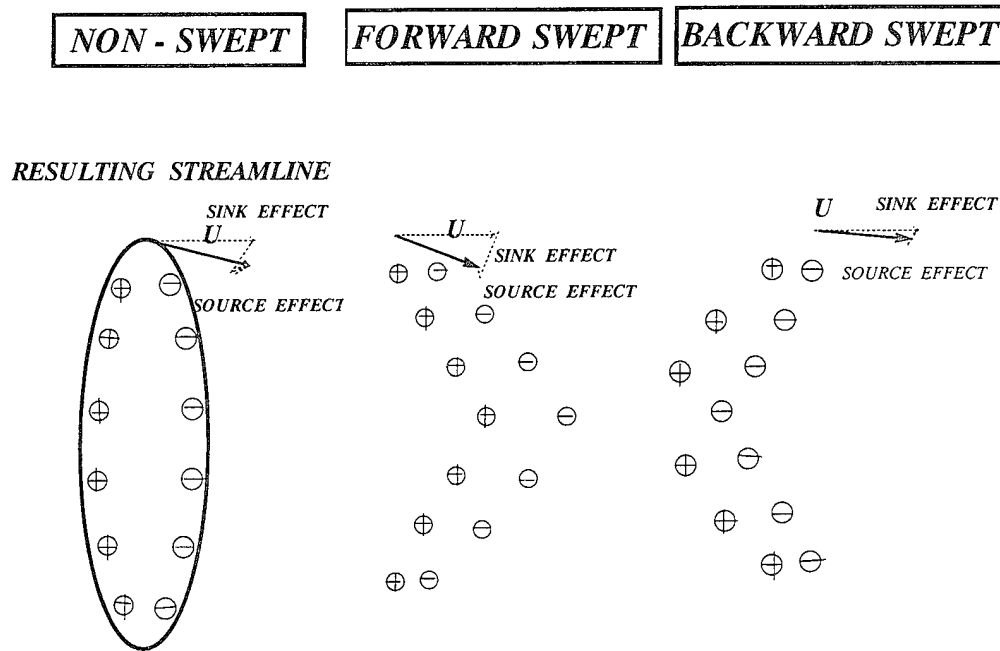
Figure 2-15: The effects of thickness sources/or sinks on the flow field in the wakes of elliptic planform hydrofoils. The effect of sinks on the wake is stronger than that of sources.

2.4.2 The FLAG on Wings

The BEM is applied on three hydrofoils with the following characteristics:

- Elliptic chord distribution in the spanwise direction.

- Aspect Ratio AR=3.

- Modified NACA66 thickness distribution with 20% maximum thickness to chord ratio (constant in the spanwise direction)

- Sweep angle varying from -45° (forward sweep) to 0° and 45°.
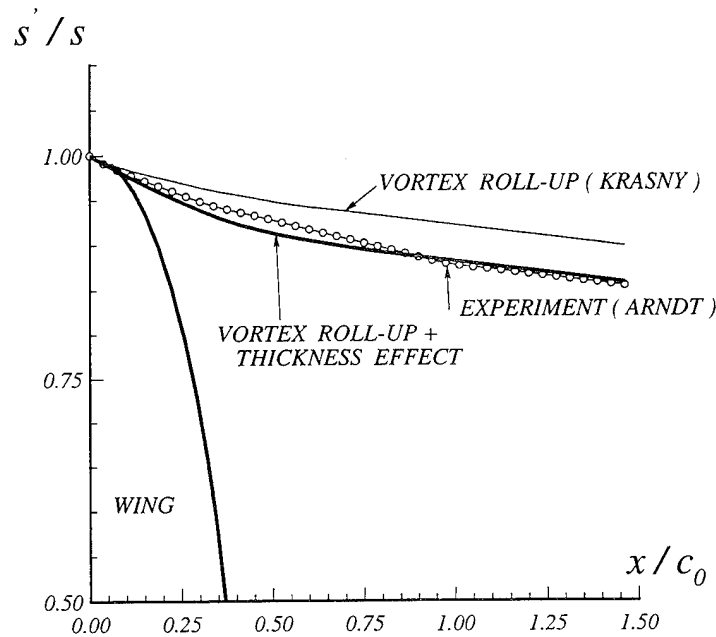
Figure 2-16: Tip vortex trajectories predicted from analysis and measured in experiment. Elliptic planform hydrofoil; $\alpha = 15.5^o$, $[\tau/c]_{max} = 0.15$, aspect ratio $AR = 3$.

The circulation distributions predicted from applying the BEM on the conventional and the flow adapted grid are shown in Figure 2-13. Notice that as the sweep angle decreases the difference between the two circulation distributions increases. This is due to the drastic contraction of the wake geometry, also shown in Figure 2-13, as the planform is swept forward. The wake contraction is increasing as the planform is swept forward, because the thickness sinks at the aft part of the planform, shown in Figure 2-15, have a stronger effect on the wake streamlines at the tip than the sources at the forward part. In addition, the circulation distributions before and after applying the IPK condition for a circular wing planform hydrofoil are shown in Figure 2-14.

44
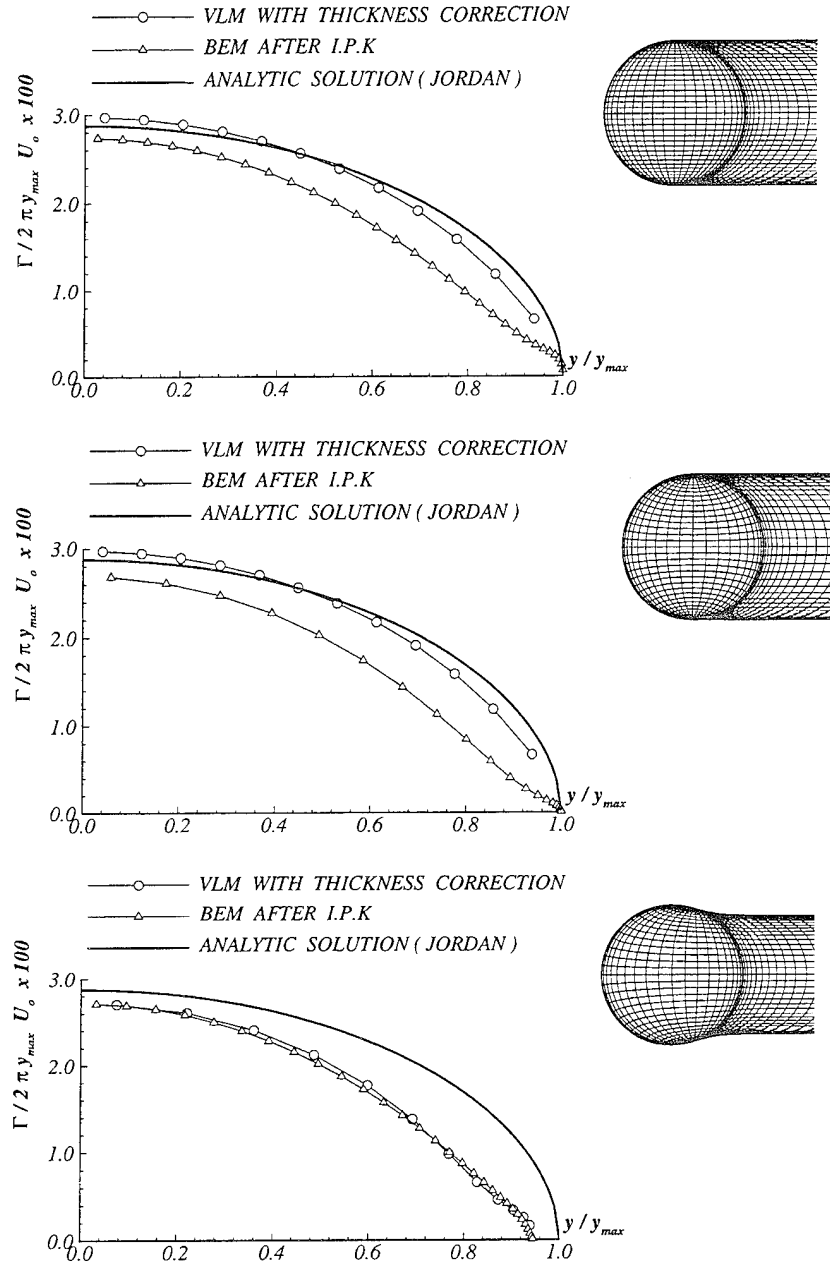
Figure 2-17: Circulation distributions predicted from BEM (after IPK condition) and Vortex-lattice Method (including the thickness loading coupling) for different grid arrangements. The analytical solution of zero thickness (Jordan, 73) is also shown. Circular planform hydrofoil ; $[\tau/c]_{max} = 0.2, \alpha = 5.73^o$. Conventional grid(top), BOG(middle), FLAG(bottom).

45

Notice that the two curves are closer to each other than they were in the case of the conventional and the blade orthogonal grid as shown in Figures 2-4, 2-8.
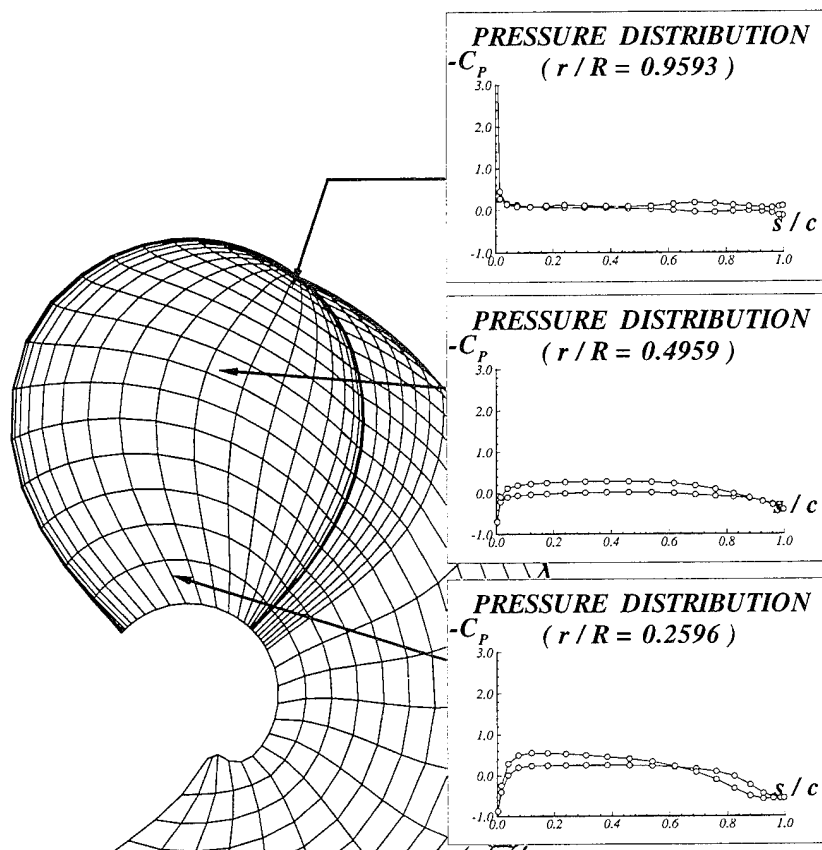
Figure 2-18: Pressure coefficients predicted from BEM applied on the flow adapted grid (after IPK condition) ; propeller N4119, $J = 0.833$, where r/R is defined at the trailing edge.

Finally, the elliptic planform hydrofoil used in the experiment by Arndt et al. [2] is analyzed by the present method. In particular, the trajectory of the tip vortex is determined, by considering only the effect due to hydrofoil thickness. The spanwise coordinates of this trajectory are then superimposed to those of the tip vortex trajectory predicted by Krasny [37], who only included the effects of the wake sheet roll-up. The results are shown, together with the experimental results, in Figure 2-

16. Notice that, under the examined condition, the effects of the wake sheet roll-up and that of the hydrofoil thickness on the predicted tip vortex trajectory are equally important, and that when both are included, the trajectory of the tip vortex matches the observed very well.
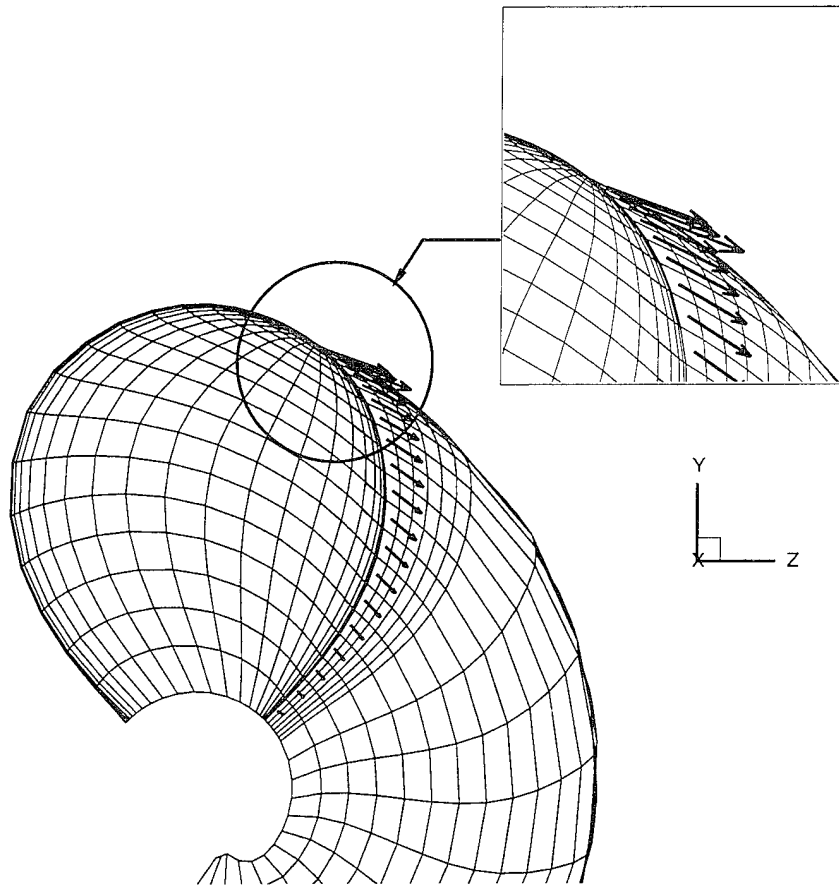
Figure 2-19: Mean velocity vectors along the trailing edge of the propeller N4119 ; $J = 0.833$. Predicted by applying the BEM on the flow adapted grid.

However, in order to validate the prediction methods completely, more comparisons with experiments at several conditions are required. In addition, further computations which also include the effects of viscosity on the hydrofoil loading, thus on the strength of the wake vortex sheet, must be carried out.

When the flow adapted grid was applied on a circular planform hydrofoil, the performance of the boundary element method was found to improve substantially. In addition, the results from applying a vortex-lattice method on the same grid were found to be in very good agreement to those from the boundary element method as shown in Figure 2-17 [36].
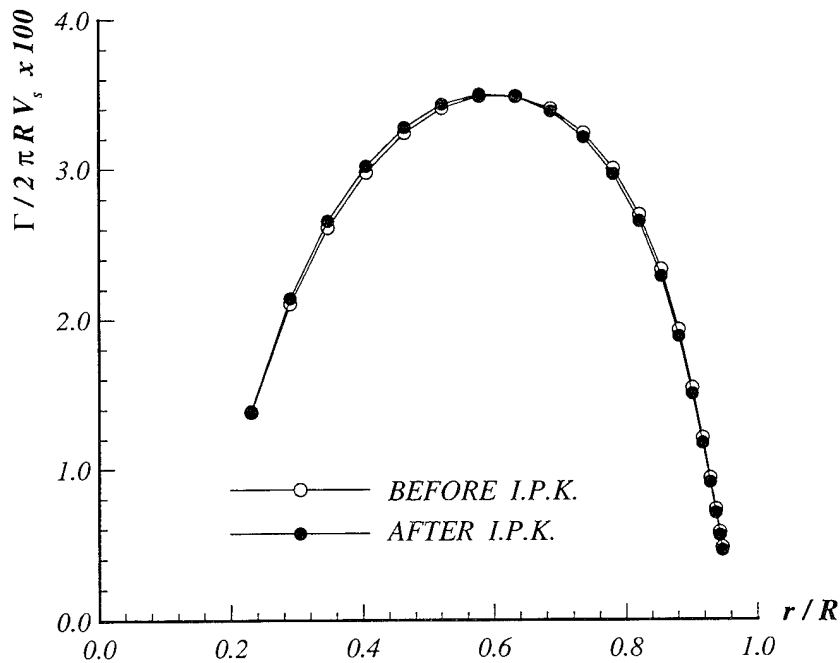
Figure 2-20: Circulation distribution on the propeller N4119; $J = 0.833$. Predicted by applying the BEM on the flow adapted grid; before and after applying the Iterative Pressure Kutta condition.

Thus, previous differences between the results from the boundary element and the vortex-lattice method have been reconciled when the flow adapted grid was incorporated. In this comparison, the Vortex-Lattice Method (VLM) is modified to include FLAG as well as the effect of coupling between thickness and loading from Kinnas

[34].

2.4.3 The FLAG on Propellers

The BEM with FLAG is applied to several propeller blades and the results are compared with experimental data.
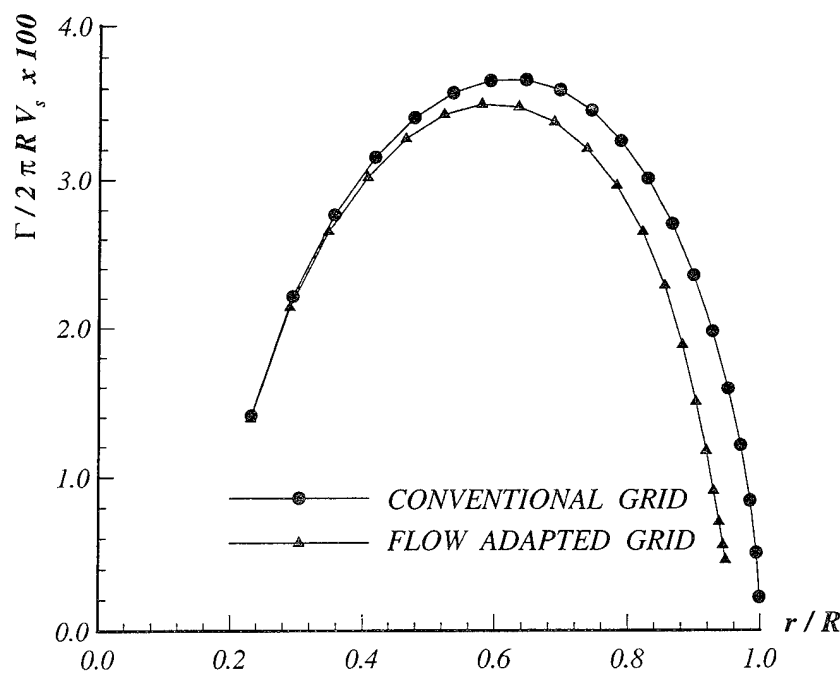
Figure 2-21: Circulation distributions predicted by the BEM applied on the conventional and the flow adapted grid.

● PROPELLER N4119

N4119 is a typical propeller with large tip chord and no skew. The resulting pressure distributions are shown in Figure 2-18. In this figure it can be seen that the pressure distribution near the tip region obtained by using the flow adapted

grid is less singular than that from the conventional grid, shown in Figure 2-5. The resulting total mean velocity vectors along the trailing edge are shown in Figure 2-19. Comparing Figure 2-19 to 2-6, we notice that the singular behavior of the velocity vectors at the tip has disappeared and that the resulting flow in the wake is aligned with the wake gridlines. Figure 2-20 shows the predicted circulation distributions before and after the iterative pressure Kutta condition to be practically identical. In the case of the conventional grid, the difference between the circulation distributions (before and after IPK), shown in Figure 2-3, appears to be slightly larger. In addition, the number of iterations for the iterative pressure Kutta condition to converge (about 4-5) is much smaller than that in the case of conventional grid. The circulation distributions from the conventional and the flow adapted grids are shown in Figure 2-21. They appear to be very different, not only at the tip but over a large part of the propeller radius.

Number of Blades   : 5
Hub/Diameter Ratio   : 0.3
Section Meanline   : NACA a=0.8
Section Thickness Form : NACA66 (Modified)

r/R	P/D	x_m/D	$\theta(degree)$	c/D	f/c	t/D
0.30	1.183	-0.0004	0.00	0.1776	0.00202	0.04442
0.35	1.360	-0.0123	-4.53	0.2099	0.00533	0.03820
0.40	1.516	-0.0237	-7.53	0.2412	0.01059	0.03377
0.45	1.642	-0.0338	-9.21	0.2714	0.01657	0.03121
0.50	1.731	-0.0414	-9.75	0.3020	0.02297	0.03041
0.60	1.795	-0.0458	-7.69	0.3620	0.02980	0.02929
0.70	1.719	-0.0395	-3.12	0.4200	0.02834	0.02780
0.80	1.547	-0.0278	4.12	0.4690	0.02036	0.02533
0.90	1.341	-0.0141	13.41	0.4650	0.00932	0.02102
0.95	1.245	-0.0072	18.82	0.3900	0.00333	0.01642
1.00	1.163	-0.0000	24.74	0.0000	-0.00270	0.00000

Table 2.1: The geometry of the propeller N4990.

Notice that the values of the circulation distribution from FLAG extend up to the radius of the computational tip, which in this case was at $0.95R$. Had the circulation distribution from FLAG been scaled with respect to its corresponding tip radius, it would result into a circulation distribution which would be practically identical to that from the conventional grid.
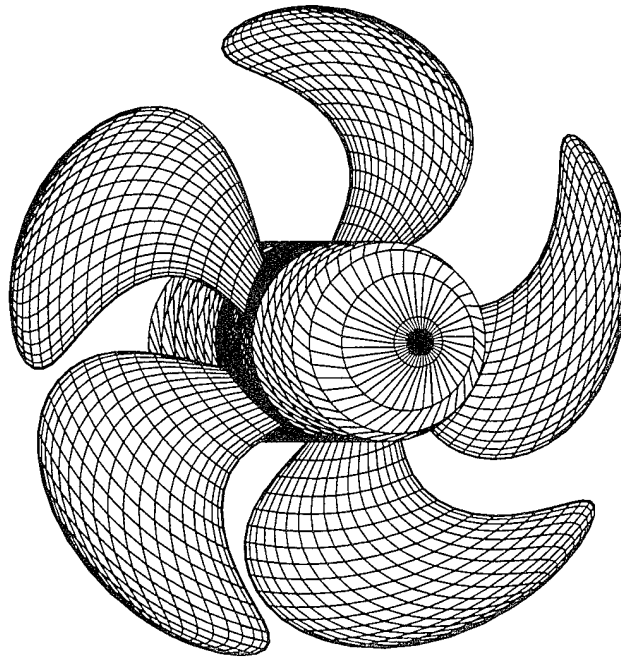
Figure 2-22: Panel arrangement for propeller N4990.

⊚ PROPELLER N4990

N4990 is a highly skewed propeller. The geometry of propeller N4990 is given in Table 2.1. The panel arrangement on the blades and hub are shown in Figure 2-22. This propeller combines a wide tip geometry and a high skew at the tip. The pressure distribution, predicted from the BEM applied on the conventional and

the flow adapted grids, are shown in Figures 2-23 and 2-24, respectively. Notice the singular behavior of the pressure at the tip in the case of the conventional grid. It should be noted that the circulation distributions (not shown) from the two grids are almost identical.
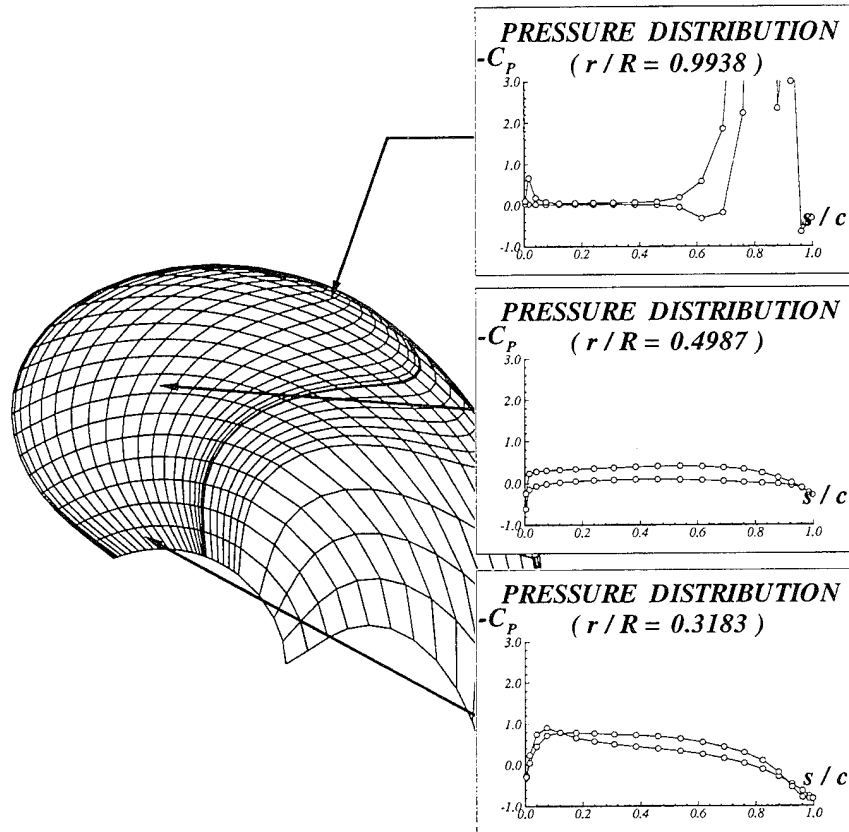
Figure 2-23: Pressure coefficients predicted from BEM applied on the conventional grid (after IPK condition); propeller N4990, $J = 1.270$.

This is attributed to the negligible change in the radial location of the computational tip, due to the combination of high skew (which may be seen as equivalent to the "backward" sweep in the case of wings as shown by Kinnas et al. [36]) and wide chord at the tip. The convergence of inviscid values of K_T, K_Q and η with number of panels is shown in Table 2.2 for the design J. It should be noted that the effect of hub was not included in this convergence

test. A 60 × 30 grid seems to be adequate for this high skew geometry case. In order to compare the results to those from experiment (supplied by Dr. Jessup of DTMB) we carried out a calculation with a 60 × 30 grid in which the paneling on the hub was also included.
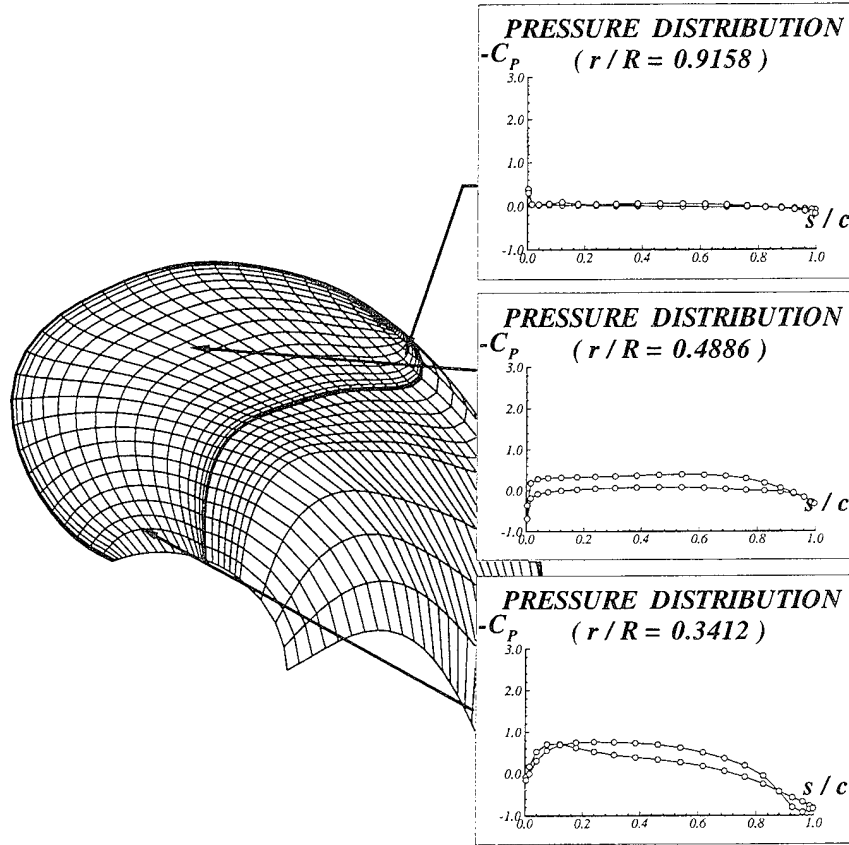
Figure 2-24: Pressure coefficients predicted from BEM applied on the flow adapted grid (after IPK condition); propeller N4990, $J = 1.270$.

The viscous effects on the forces were estimated via a constant friction coefficient C_F, assumed to be equal to 0.005. The viscous force was computed by the following equation ;

$$\boldsymbol{F}_V = \frac{1}{2} \rho \, C_F \int_S |\boldsymbol{V}_{TOTAL}| \, \boldsymbol{V}_{TOTAL} dS$$

where V_{TOTAL} is the total velocity on the surface of the blade. Table 2.3 shows K_T, K_Q and η with and without viscous effects, versus the measured values. The differences between the experimental and the computational results are within 5%.

PROPELLER N4990 (J=1.270)
($C_F = 0.0$& With Leading Edge Suction)

CONVENTIONAL	K_T	$K_Q \times 10$	η
$40c \times 20s$	0.2319	0.5519	0.8492
$60c \times 30s$	0.2406	0.5759	0.8442
$80c \times 40s$	0.2384	0.5718	0.8430
$90c \times 40s$	0.2379	0.5693	0.8448

Table 2.2: Convergence of K_T and K_Q ($C_F = 0$).

PROPELLER N4990 (J=1.270)
(With Hub)

CONVENTIONAL	K_T	$K_Q \times 10$	η
$C_F = 0.0000$	0.2392	0.5753	0.8403
$C_F = 0.0050$	0.2292	0.6732	0.6851
EXPERIMENT	0.243	0.691	0.709

Table 2.3: K_T and K_Q with and without viscous effect.

GRID	J	K_T	ERROR	$K_Q \times 10$	ERROR
CONVENTIONAL	0.833	0.149	2%	0.306	9%
	1.100	0.033	3%	0.114	8%
FLAG	0.833	0.143	2%	0.286	2%
	1.100	0.034	0%	0.113	7%
EXPERIMENT	0.833	0.146		0.280	
	1.100	0.034		0.106	

Table 2.4: Force coefficients of propeller N4119 ($C_F = 0.005$).

These force parameters were compared to those from the flow adapted grid for different J's, as shown in Figure 2-25 and Table 2.4. The coefficients from the flow adapted grid were much closer to the experimental values. Especially, the value of K_Q was much closer to the experimental value as shown in Table 2.4.
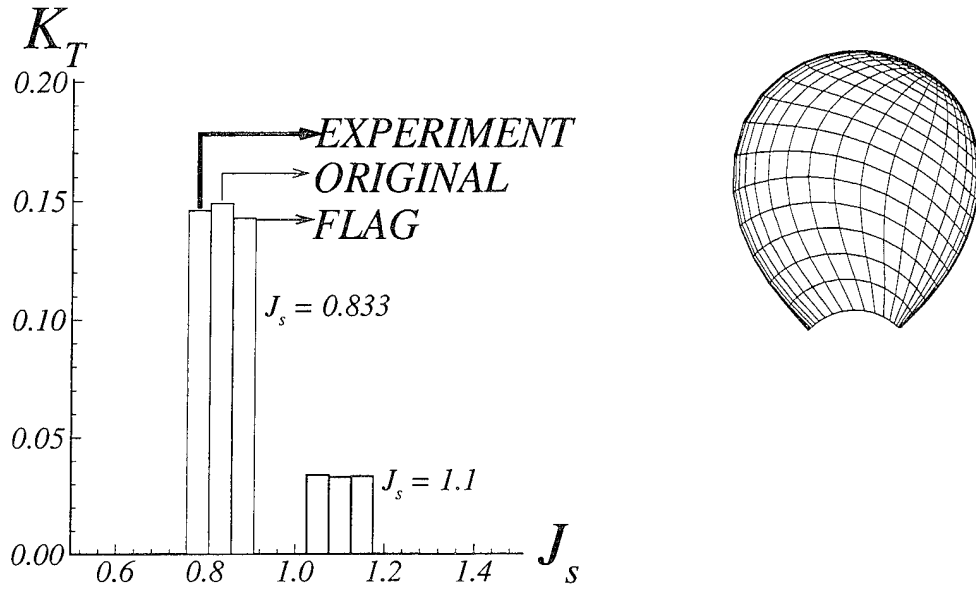
Figure 2-25: ; Force coefficients of propeller N4119.: with hub effect, $C_F = 0.005$, $J = 0.833, 1.1$.

2.4.4 Numerical Validation

In this section in order to validate the results of panel method with FLAG, a convergence test of the results from the method for a wide tip propeller (N4119) and the consistency test of the method, also for a wide tip propeller (N4118) are performed.

⊛ **Convergence Test for Propeller N4119.**

In this test, the convergence of the circulation distributions is examined, as the number of panels in both chordwise and spanwise directions are increased. The

convergence of the resulting circulation distribution from applying the BEM on FLAG with varying numbers of chordwise and spanwise panels is shown in Figure 2-26. A 40 × 20 grid appears to produce convergent results.
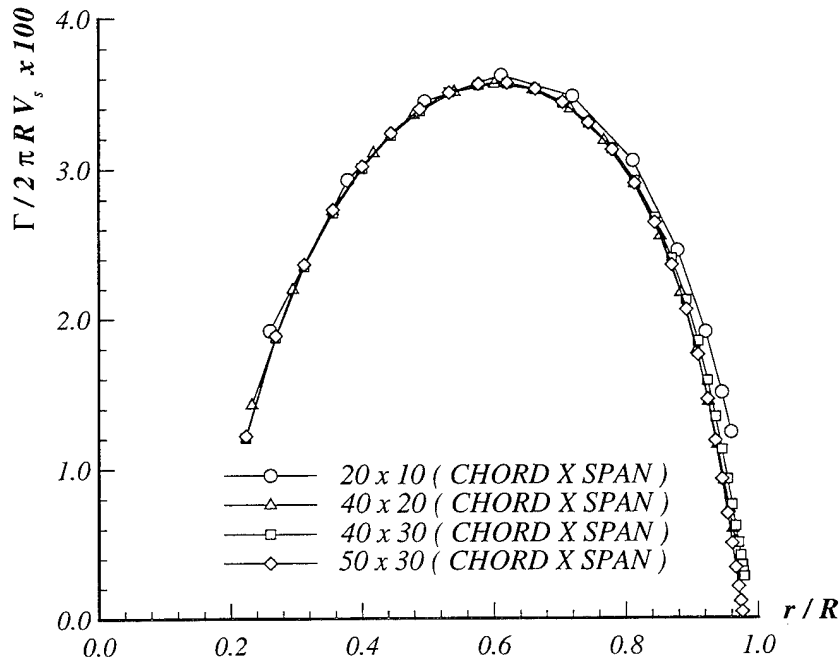
Figure 2-26: Convergence test for N4119 propeller.

- **Consistency Test for Propeller N4118**

A test of the consistency of lifting surface and panel method can be made by linearly extrapolating to zero thickness the results of a sequence of panel calculations for different thickness ratios. The panel calculations are made for a set of geometries which are identical except for a constant scale factor applied to the thickness. The circulation distribution for zero thickness is then determined by linearly extrapolating with thickness the circulation from the panel method.

This zero thickness "panel method" result is then compared to the result from the lifting surface analysis method by Greeley and Kerwin [16]. The results for the N4118 propeller are shown in Figure 2-27. The circulation distributions from the panel method (applied on FLAG) for different thickness scale factors (100% corresponds to the original thickness distribution) appear to extrapolate smoothly (linearly) to the circulation distribution from the lifting surface method.
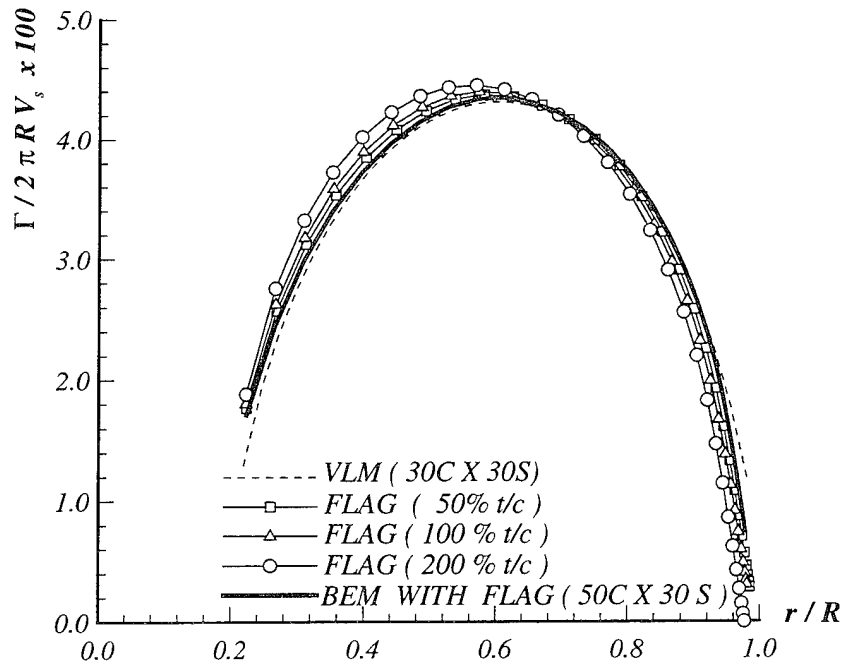
Figure 2-27: Consistency test for N4118 propeller.

Notice that as the thickness decreases the location of the computational tip approaches the actual tip. The extrapolated panel method result versus the lifting surface result is shown at the bottom part of Figure 2-28. The consistency test in the case of applying the panel method on the conventional grid has been

performed by Hsin [24] and the results are shown at the top part of Figure 2-28. A 3% difference between the maximum circulation from the panel method and the lifting surface method was reported by Hsin [24]. This difference appears to become smaller in the case of the flow adapted grid, as can be seen in Figure 2-28.

In this chapter, the flow adapted grid was incorporated in an existing BEM for the analysis of propeller tip flows. The proposed grid has been found to predict the flow and pressures at the tip more reliably than when employing the conventional grid. For wide tip blades with zero skew (N4119) the predicted circulation distributions were found to be different from those employing the conventional grid, primarily due to the change of location of the tip detachment point in the case of the flow adapted grid. On the contrary, for wide tip blades with high skew (N4990) the proposed grid did not affect the predicted circulation distribution even though it improved the predicted pressures at the tip substantially. In addition, the flow adapted grid was found to improve the validity of the consistency test between the boundary element and vortex lattice method for the N4118 propeller.
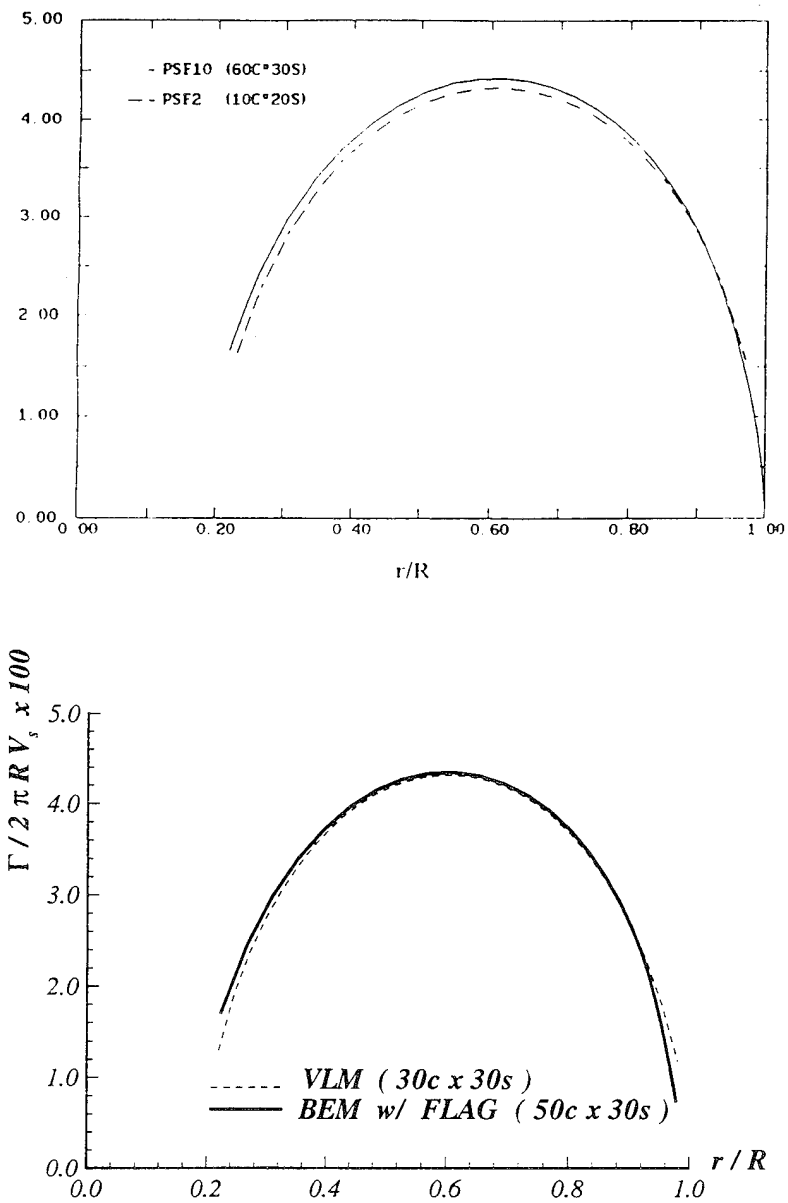
Figure 2-28: Consistency test for N4118 propeller. Top ; Conventional grid (from Hsin,1990), Bottom ; Present method (FLAG).

Chapter 3

The Vortex Sheet Roll-Up

In the previous chapter, the trailing wake sheet was assumed to be aligned with the velocities at the trailing edge in the wake. The effect of wake sheet roll-up was ignored. In reality, the trailing wake sheet is rolling up into a core containing the vorticity shed from the tip region. This roll-up effect is considered to be of the primary mechanism of the tip vortex structure. In addition, when the propeller is heavily loaded or the circumferential velocity due to the rotation of the propeller is large compared to the forward velocity of the ship, the sheet passes very close to the following blades and the wake sheet roll-up results in a change in loading, velocity field and pressures on the propeller blades. In this chapter, the vortex sheet roll-up will be calculated in two and three dimensions by using various methods, and the results will be compared with each other. In Chapter 5, the wake sheet roll-up will be included in the flow adapted grid.

3.1   Two-Dimensional Method

3.1.1   Vortex Blob Method

The conjugate complex velocity $\tilde{q}(z)$ induced by a two-dimensional vortex sheet of strength $\gamma(s,t) = \partial\Gamma/\partial s$ situated on the curve $C(s)$ is given by the Rott-Birkhoff [67], [6] nonlinear integro-differential equation ;

$$\tilde{q}(z) \quad = \quad u - iv = \frac{1}{2i\pi} \int_C \frac{\gamma(s',t)ds'}{z - z(s',t)} + U_e - iV_e \tag{3.1}$$

where U_e and V_e are the components of the incoming flow evaluated at z as shown in Figure 3-1.
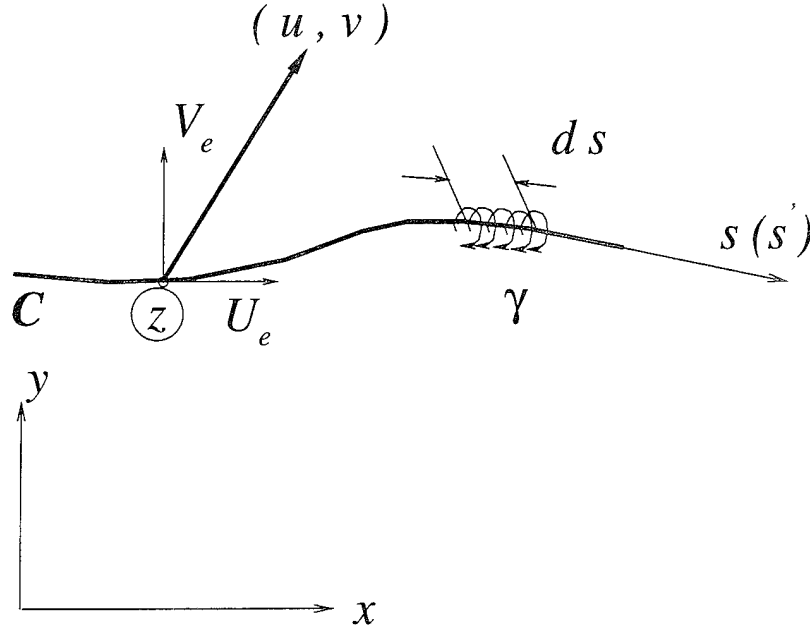
Figure 3-1: Velocity and vorticity diagram.

The Cauchy principal value is assumed for the integral in equation (3.1) in order to calculate the velocity at points on the sheet. Equation (3.1) has been generalized to the case of a vortex sheet with small thickness by Moore [57]. If the circulation Γ is chosen as the Lagrangian variable, equation (3.1) may be written from Birkhoff [6] as,

$$\frac{\partial \tilde{z}}{\partial t}(\Gamma, t) \quad = \quad u - iv = \frac{1}{2i\pi} \int_C \frac{d\Gamma'}{z(\Gamma, t) - z(\Gamma', t)} + U_e - iV_e \tag{3.2}$$

61

Equations (3.1) and (3.2) ensure the continuity of pressure across the sheet and the conservation of circulation around a segment lying between any two points moving with the sheet. Equation (3.2) must be solved numerically, since an analytic solution does not exist.

In the vortex blob method, the vortex sheet is replaced by a finite number of points, namely "blobs", which are assumed to be rigid. Then the motion of the sheet is approximated by calculating the trajectories of the blob. For example, when the trailing vortex sheet of a wing is represented by an array of N line vortices, equation (3.2) reduces to an initial value problem, consisting of a set of $2N$ first order ordinary differential equations whose solution requires suitable smoothing technique. Many numerical attempts have been made with different smoothing techniques, such as amalgamation by Ham [17] and Fink and Soh [13], subvortex model by Maskew [46], rediscretization by Fink and Soh [14] and Sarpkaya [69], and cut-off scheme by Krasny [37] and Kuwahara [39].

In this section, Krasny's method [37] will be described briefly. The discretized form of the equation (3.2) may be expressed as,

$$u_k - iv_k = \frac{1}{2i\pi} \sum_j \frac{\Gamma_j}{z_k - z_j} + (U_e)_k - i(V_e)_k \qquad (3.3)$$

In desingularizing the vortex sheet equation (3.3), an artificial smoothing parameter, δ, is applied at the right-hand side of equation (3.3).

$$u_k - iv_k = \frac{1}{2i\pi} \sum_j \frac{\Gamma_j}{z_k - z_j} \cdot \frac{|z_k - z_j|^2}{|z_k - z_j|^2 + \delta^2} + (U_e)_k - i(V_e)_k \qquad (3.4)$$

The equation (3.4) is no longer singular at $z_k = z_j$ for $\delta > 0$. As δ goes to zero, equation (3.4) converges to the original equation (3.3). Krasny [37] demonstrated that the numerical solutions of the vortex blob equations (3.4) for different values of δ converge to a limit curve as $\delta \to 0$ and this curve can be interpreted as a weak

solution of the original vortex sheet evolution equation (3.1).
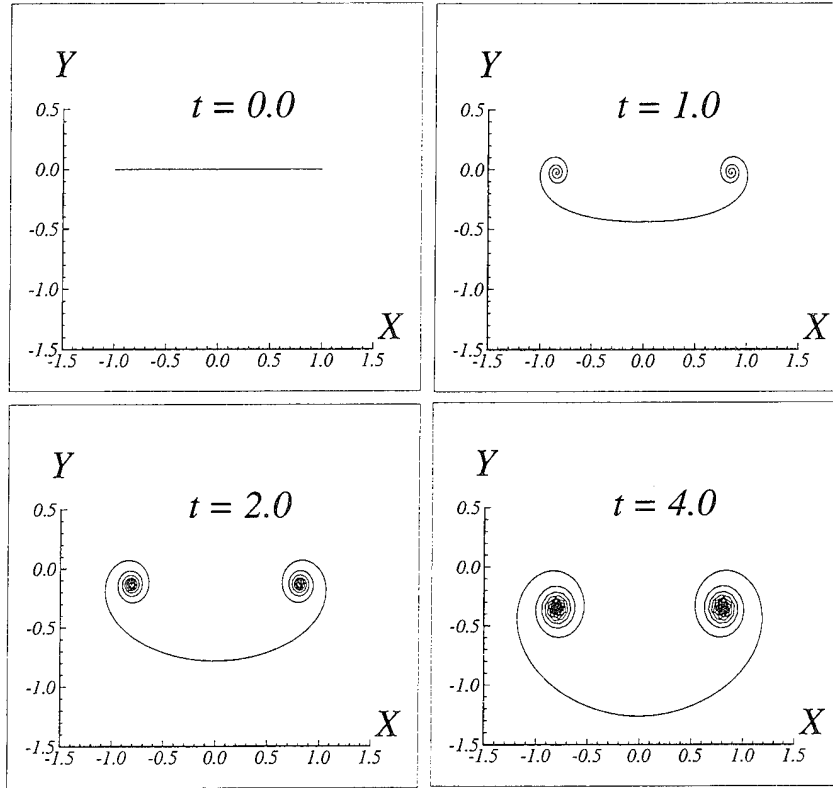
Figure 3-2: Roll-up behind a lifting line with elliptic loading predicted by Krasny(1987) ; $\delta = 0.05, N = 200, \Delta t = 0.01$.

Two examples are shown in Figures 3-2 and 3-3. The cases studied are the vortex sheet roll-up for a lifting line with elliptic loading and an embedded vortex sheet in two-dimensional uniform flow. The methods predict the vortex sheet roll-up very smoothly even in the late stage because δ provides the damping of short waves. The method also shows good convergence with number of panels. However, the use of vortex blobs has the following problems :

- Mathematically, the linear sum of vortices cannot constitute an exact solution of the nonlinear equations of motion.

- Near the core, each blob is not allowed to distort because the blob is assumed to have an invariable core shape and size.

- Finally, it is time consuming and difficult to extend to three dimensions.
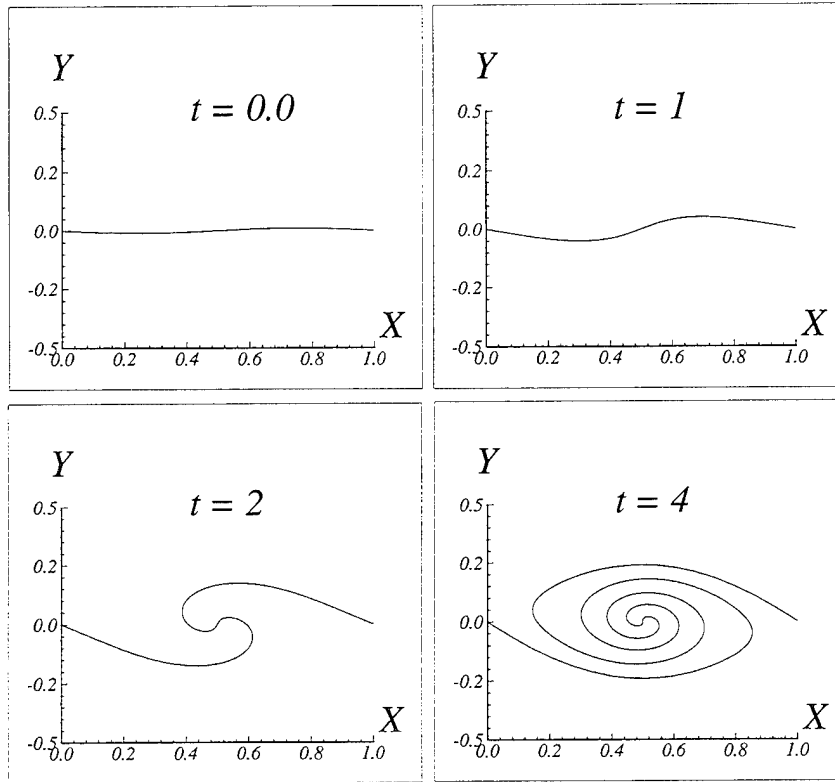
Figure 3-3: A vortex sheet embedded in two-dimensional uniform flow; $\delta = 0.5, N = 400, \Delta t = 0.1$. Predicted by Krasny [37].

3.1.2   Discrete Vortex Method

The velocity induced by the vorticity concentrated in a bounded region is given by Bachelor [5]

$$u(\boldsymbol{r}, t) = -\frac{1}{4\pi} \int \int \int \frac{(\boldsymbol{r} - \boldsymbol{r}') \times \omega(\boldsymbol{r}', t)}{|\boldsymbol{r} - \boldsymbol{r}'|^3} dV(\boldsymbol{r}') \qquad (3.5)$$

where $\boldsymbol{r}$ is a position vector from a point in a bounded region to a field point.
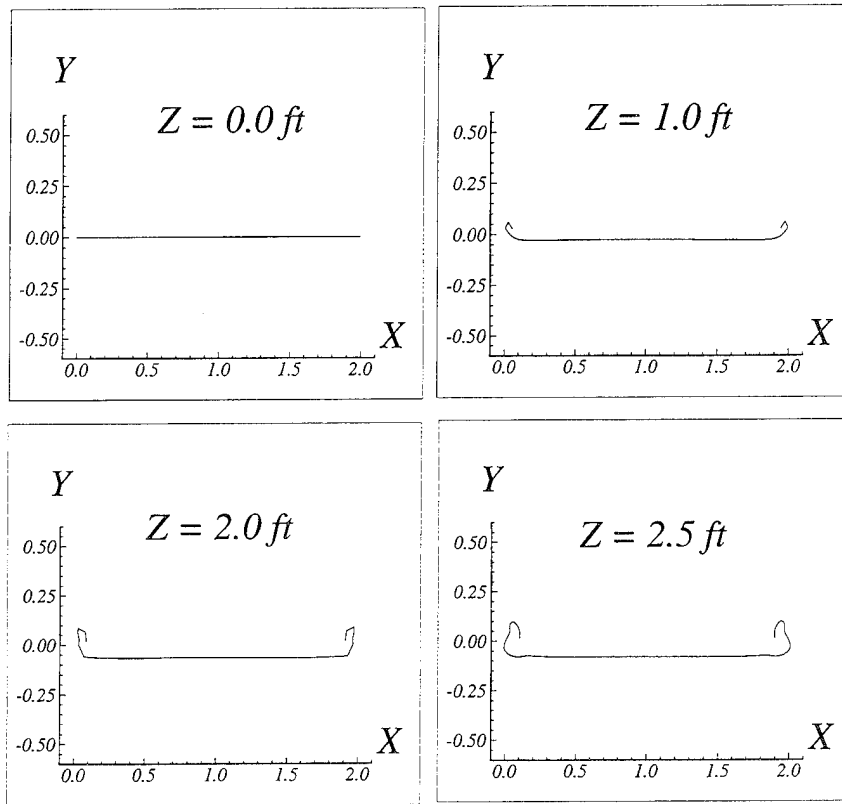
Figure 3-4: Cross section of the wake sheet behind a lifting line of 2 ft span with elliptic loading. The circulation at midspan is $3ft^2/sec$. 99 trailers are taken at even spacing.

If the vorticity is concentrated in a single curved filament of circulation Γ, equation (3.5) reduces to the Biot-Savart law

$$u(\boldsymbol{r}, t) = -\frac{\Gamma}{4\pi} \int_C \frac{(\boldsymbol{r}(s) - \boldsymbol{r}'(s')) \times d\boldsymbol{r}'(s')}{|\boldsymbol{r}(s) - \boldsymbol{r}'(s')|^3} \tag{3.6}$$

where $\boldsymbol{r}(s)$ describes a position vector of the filament centerline in terms of the arclength s.

Equation (3.6) yields an infinite self-induced velocity if the filament is curved and zero induced velocity if it is straight as explained by Bachelor [5]. Several methods have been introduced to handle this, such as the Local Induction Approximation by Hama [18]. However, the only way to get the desired shape of the roll-up, is to ignore this term.

In this section, the vortex sheet is represented by a series of discrete line vortices. The calculations are done midway between vortices to avoid an infinite self-induced velocity. For each location, the velocity due to each element is calculated and summed to obtain the total induced velocity V at each point on the sheet. Starting at the trailing edge, a new location of the sheet is formed by

$$\boldsymbol{x}_{(n,p)} = \boldsymbol{x}_{(n,p-1)} + \boldsymbol{V}_{(n,p-1)} \cdot \Delta t.$$

where n describes the number of iteration and p is the index for station along the streamwise direction. The result for the lifting line with elliptic loading is shown in Figure 3-4. This method seems to predict the shape of the roll-up smoothly. The method can very easily be extended to three dimensions. However, the choice of vortex spacing has an effect on the ultimate shape of the roll-up and also, there are difficulties with this method even for two-dimensional flow simulation. First, the vortex filaments are singularities and hence create large velocities in their neighborhood. This causes instabilities and physically impossible sheet crossings along and near the edges of the sheet. The second difficulty is in the CPU per time step. The number of operations required for the velocity calculation is proportional to N^2, where N is the number of vortices. Thus, the CPU time increases significantly as the number of vortices increases.

3.1.3 Panel Method

There have been a large number of attempts to model the vortex sheet motion by replacing the continuous vortex sheet with a finite number of discrete vortices. However, it appears that despite these various attempts, the discrete vortex representation results inevitably in numerical instabilities, i.e. chaotic motion, when the number of vortices is increased. It must also be noticed that the question of the existence and uniqueness of the solutions for equations describing vortex sheet motion has not yet been fully resolved as mentioned by Moore [58]. So, it can be said that the discrete vortex method is not adequate to compute vortex sheet roll-up reliably. Recently, panel methods have been applied in order to get more reliable and accurate representations of the vortex sheet roll-up in two dimensions. The method has been extensively described by Faltinsen and Petterson [12] and Hoeijmakers [22]. The earlier attempt by Mokry and Rainbird [55] using a low-order panel method seemed promising, but numerical instabilities still appeared. It has been suggested that the use of a high-order panel method is more accurate than the low-order panel method or the discrete vortex method to compute the velocity field, since it precludes the appearance of instabilities in the vortex sheet due to the spurious numerical effects introduced by a too crude representation.

In this section, a high order-panel method is used to compute the velocity field induced by the multiple segmented vortex sheet in two dimensions. The vortex sheet is modeled by piecewise continuous dipole distributions. The velocity, q, at a point (x, y) induced by a dipole distribution $\Gamma(t)$ on a sheet $C(t)$ is written as

$$q = \nabla\phi(x,y) = -\frac{1}{2\pi} \int_{C(t)} \frac{d\Gamma(t)}{dt} \nabla\left(\frac{\partial}{\partial n}\log r\right) \, dl \qquad (3.7)$$

where t is a parametric variable along the sheet $C(t)$ and dl is a differential element of length along $C(t)$.

The curve $C(t)$ is divided into number of panels as shown in Figure 3-5. Then, equation (3.7) becomes

$$\boldsymbol{q}_i \;=\; \nabla\phi(x_i,y_i) = -\frac{1}{2\pi}\sum_j \int_{C(t_j)} \frac{d\Gamma(t_j)}{dt}\nabla\left(\frac{\partial}{\partial n_j}\log r_{i,j}\right)\; dl_j \qquad (3.8)$$

where subscript i is an index for a field point and j denotes the functions on the j-th segment. On each panel, the function $\Gamma(t)$ is approximated by piecewise quadratic representations. Let $\Gamma(t) = a_0 + a_1 t + a_2 t^2$.
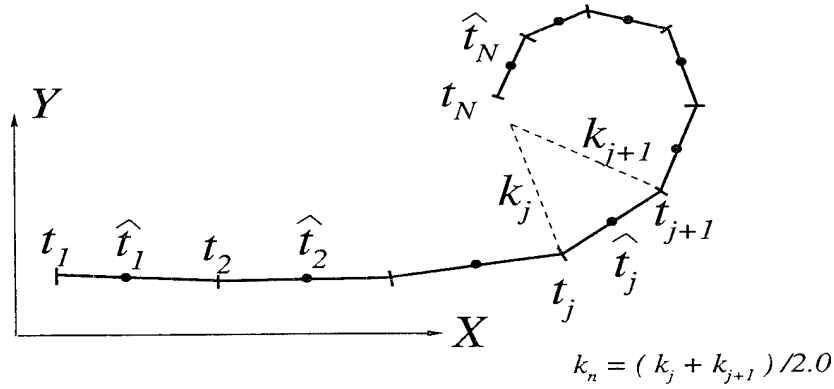
Figure 3-5: Vortex sheet arrangement.

Then, equation (3.8) can be expressed as :

$$\boldsymbol{q}_i \;=\; \nabla\phi(x_i,y_i) = -\frac{1}{2\pi}\sum_j \int_{C(t_j)} (a_1 + 2a_2 t_j)\,\nabla\left(\frac{\partial}{\partial n_j}\log r_{i,j}\right)\; dl_j \qquad (3.9)$$

The integrals in equation (3.9) can be expressed in closed form. For a field point in the far field, the computation time is saved by using the multipole expansion rather than the closed form. To avoid spurious effects from the panel edges where the geometry and the dipole distribution may be discontinuous, the panel midpoints are

chosen as the control points.

The detailed computational scheme is as follows.

1. For a given position and strength of the sheet at time τ, the induced velocity components (U_j, V_j) are computed at the panel midpoints $(\hat{t}_j)$.
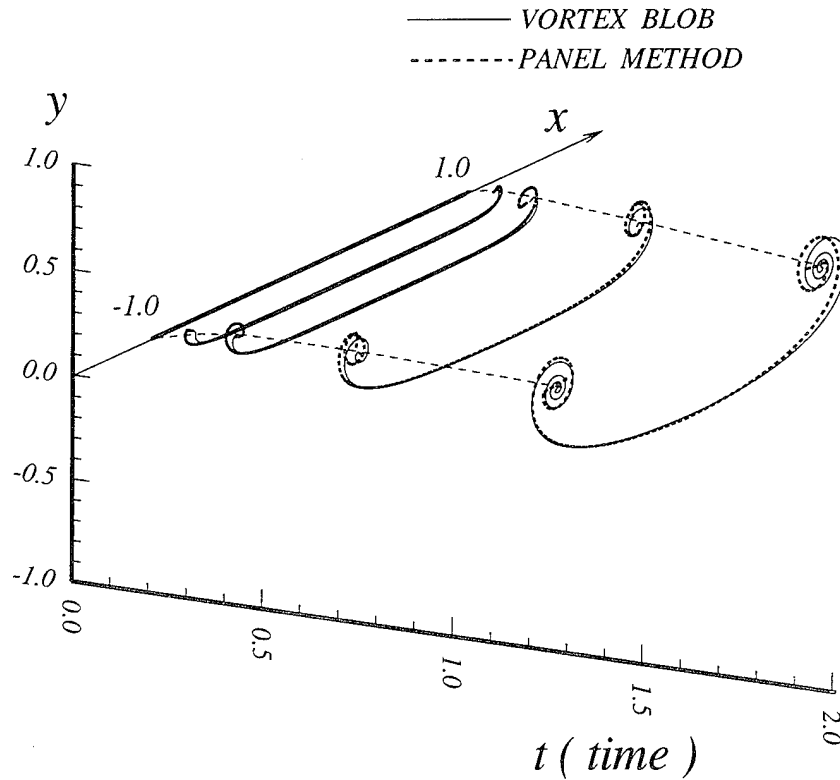
Figure 3-6: The shape of the roll-up behind a lifting line with elliptic loading.

2. The panel midpoints are advanced in time by a simple Euler scheme, i.e. by an amount of $(U_j \Delta\tau, V_j \Delta\tau)$, where $\Delta\tau$ is chosen such that each midpoint is not moved more than Δt_j. The new position of the end points t_1 and t_N are found by a quadratic extrapolation from the new values of the three nearest midpoints.

3. The new values of $x(\hat{t}_j)$, $y(\hat{t}_j)$ and $\Gamma(\hat{t}_j)$ are then the input data for a cubic spline procedure.
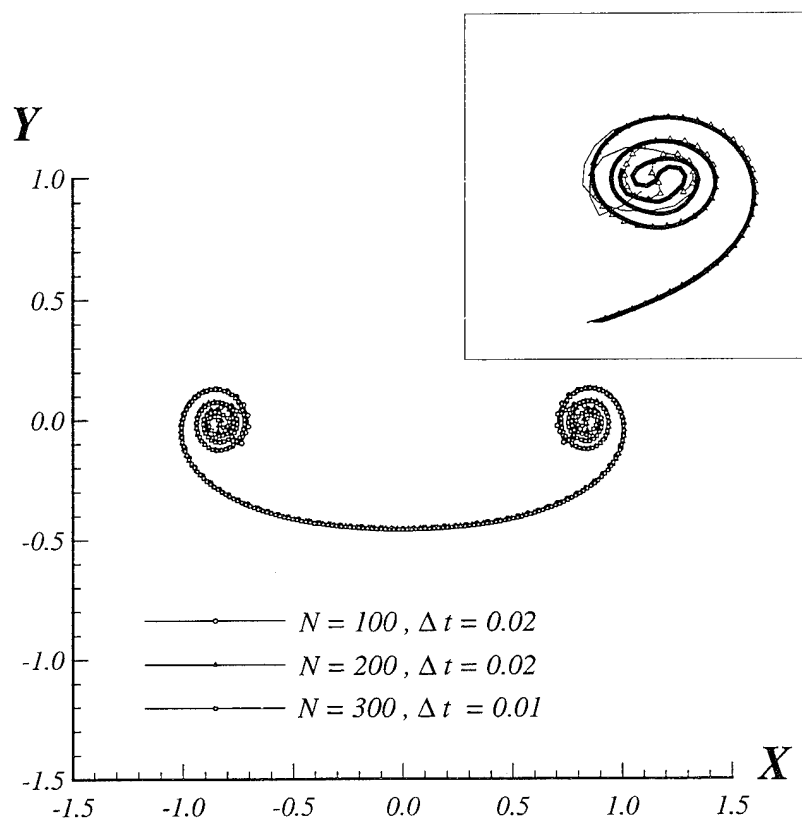
Figure 3-7: Convergence test of the results from the panel method. The vortex sheet at t = 1.0 behind the lifting line with elliptic loading.

4. With the cubic spline representation for $x(t)$, $y(t)$ and $\Gamma(t)$, a rediscretization scheme, called "adapted curvature-dependent" [22], is applied, which computes the values of the panel edges (t_j). Using the rediscretization method, the panel edge points are computed such that $t_{j+1} = t_j + \Delta_{max}$ unless Δt_j spans an arc of more than θ_{max} degrees of a circle with a radius equal to the average radius of curvature within $[t_j, t_{j+1}]$. In the latter case, $t_j = \theta_{max}/k_n$, where k_n is the average radius of curvature in the interval. The value of Δ_{max} and θ_{max} are user specified. For example in this chapter, Δ_{max} and θ_{max} are set equal to the ratio

70

of total arclength of the sheet to the number of panels and 45°, respectively.

5. Finally, the new values of $x(t_j)$, $y(t_j)$ and $\Gamma(t_j)$ are computed via the cubic spline approximation.
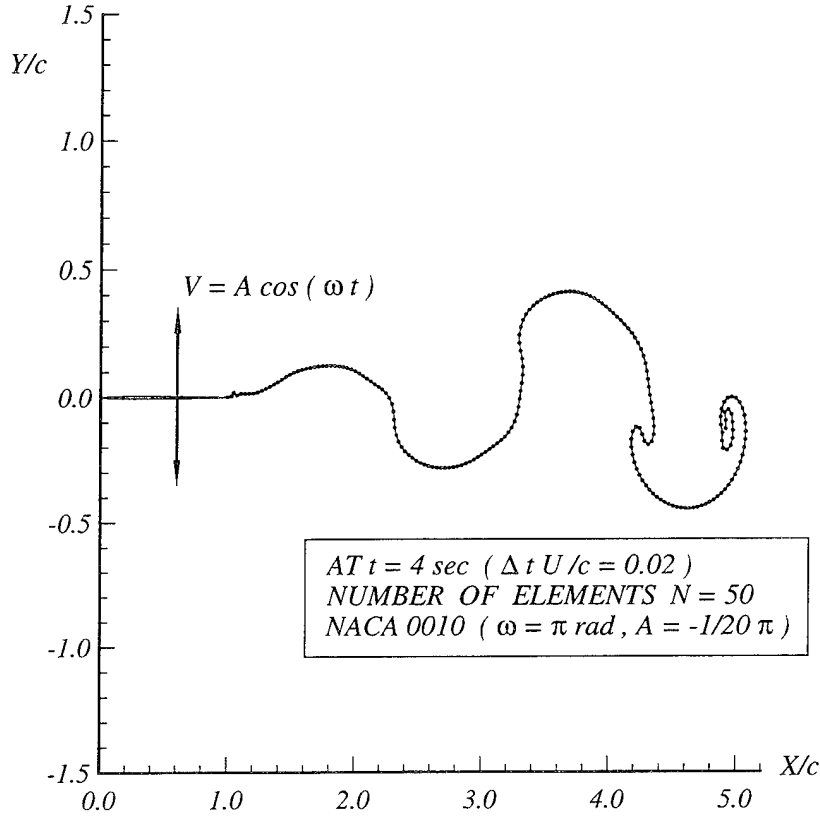
Figure 3-8: The wake profile for a heaving hydrofoil.

This procedure is repeated until the geometry of the vortex sheet is converged. As a test of this method, the same problem as that shown in Figure 3-2 is solved and the result is compared to that from applying the vortex blob method, described in Section 3.1.1. The resulting geometries of the vortex sheet roll-up predicted by the two methods are shown in Figure 3-6. The comparison shows that the results from the two methods agree well to each other except inside the core. This discrepancy in the core will be discussed in section 3.2.3. A convergence test of the results from

71

this method is shown in Figure 3-7. Figure 3-7 shows a clear convergence trend with increasing number of panels. This method is also applied to the two-dimensional unsteady hydrofoil problem for the purpose of extension to the three-dimensional unsteady propeller problem.
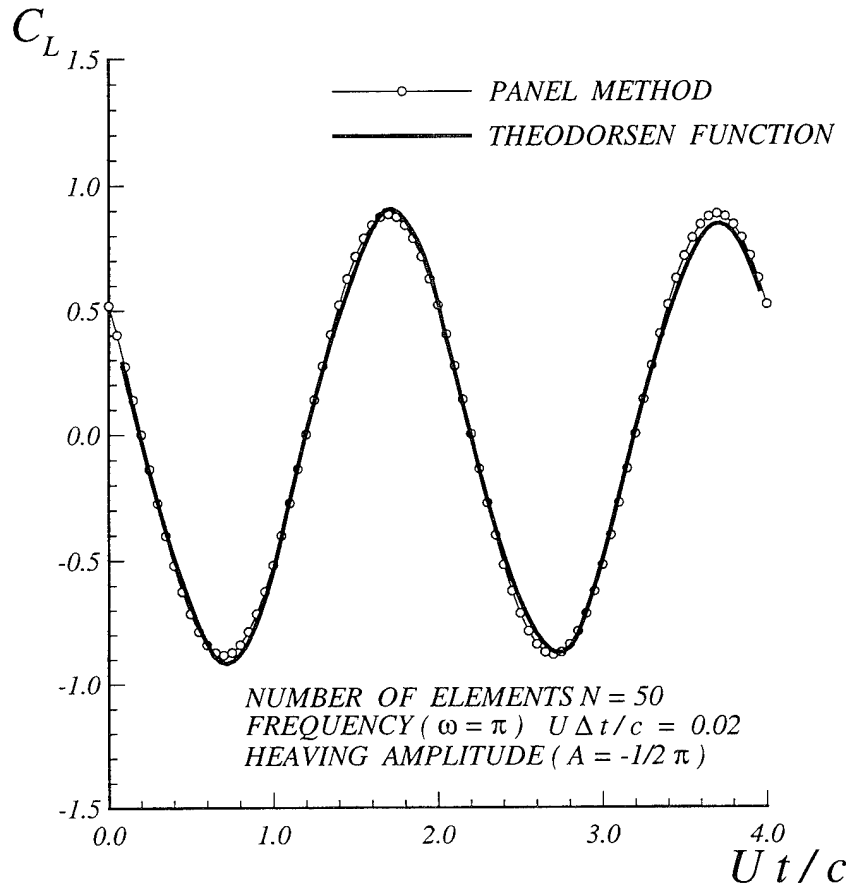
Figure 3-9: Comparison of analytic and numerical solutions for the heaving hydrofoil.

Figure 3-8 shows the wake shape behind a heaving hydrofoil. In Figure 3-9, it is shown that the lifting coefficient from the present panel method agrees very well with that from the analytic method, given by the well known "Theodorsen function" (Newman [62]). For a two-dimensional calculation of the vortex sheet roll-up, it is shown that the high-order panel method predicts the geometry of the vortex sheet roll-up reliably and smoothly. In addition, this method is much faster than the vortex blob method and is very easy to extend to three dimensions.

3.2 Three-Dimensional Methods

A number of three-dimensional flow models have been implemented for the prediction
of wake sheet roll-up. These consist of the discrete vortex/strip theory methods,
vortex lattice methods and panel methods. Existing models will be summarized first,
and then a new high-order panel method will be described.
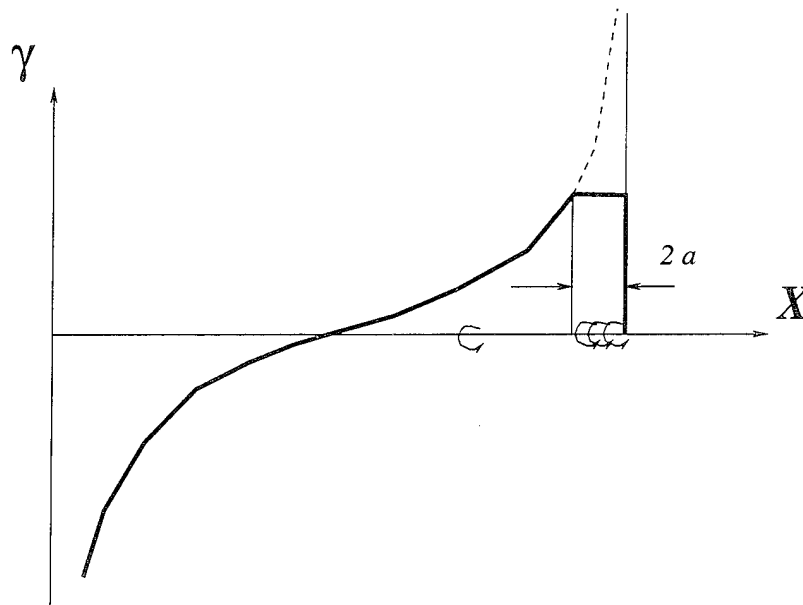
Figure 3-10: A model of the tip vortex core.

3.2.1 Discrete Vortex/Strip Theory Method

The discrete vortex method can be easily extended to three dimensions in a strip-
wise sense. This method can predict the geometry of the vortex sheet. However,
the method does not include three-dimensional effects such as the concentration of
vorticity in the core region because the streamwise velocity is assumed to be constant.
This three-dimensional effect was first modeled by Cummings [8]. In this section, his
modeling and numerical implementation will be discussed. The classical discrete vor-
tex method as mentioned earlier suffers from lack of convergence. The ultimate shape

computed in the tip region depends on the choice of the vortex spacing. To avoid this problem, a model of the tip vortex core is introduced. The tip vortex core model assumes that the tip vorticity is spread out over a finite thickness $(2a)$, as shown in Figure 3-10, where a is a boundary layer thickness at the pressure side of the tip. Within this model, even if the spacing becomes fine, the resulting shape of the vortex sheet will not be singular at the tip. As for the modeling of the three-dimensional effect, it will be impossible for any concentration of vorticity (in addition to that due to the two dimensional roll-up) to occur in a model which assumes that the streamwise velocity is constant. A concentration of vorticity implies a concentration of fluid since the vortices move with the fluid. The only model which can produce a concentration of fluid is a sink in the core, which increases the axial velocity and decreases the core pressure. Far downstream, a concentration of vorticity can occur in two ways. The roll-up of the vortex sheet increases the circulation surrounding the core and any flow into the core brings in circulation from the sheet. The first effect, due to the vortex sheet roll-up, is small in any case, because the sheet vorticity is small compared to that in the core. The second effect is a major source of increasing core circulation due to absorbing of the trailing vortex sheet into the core. This effect can be modeled as follows. A length Δx of the core is considered with a pressure force F acting on it in the axial direction as shown in Figure 3-11. The radial velocity V is assumed at first to be zero. Consider the continuity and momentum equations in the x-direction over a control volume of radius a and length Δx. As explained in Appendix B, a can be assumed to be constant and the flow inside the core(as defined in Appendix B) to be inviscid.

From the continuity equation,

$$ u_2 \;=\; u_1 + \frac{2V}{a} \cdot \Delta x \tag{3.10} $$

where U_0 is an inflow velocity outside of the core; u_1 and F_1 are the induced velocity and the acting force on the upstream side of the core, respectively; u_2 and F_2 are the same variables on the downstream side of the core.

From the momentum equation in the x-direction,

$$\rho \pi a^2 u_2^2 + F_1 = \rho \pi a^2 u_1^2 + 2\pi a \rho V U_0 \Delta x + F_2$$

$$F = F_1 - F_2 = \rho \pi a \left(a u_2^2 - a u_1^2 - 2\Delta x V U_0 \right) \qquad (3.11)$$

Combining equation (3.10) and (3.11),

$$V = \frac{a}{4\Delta x} \left[U_0 - 2u_1 + \sqrt{(U_0 - 2u_1)^2 + \frac{4F}{\rho \pi^2 a^2}} \right]$$
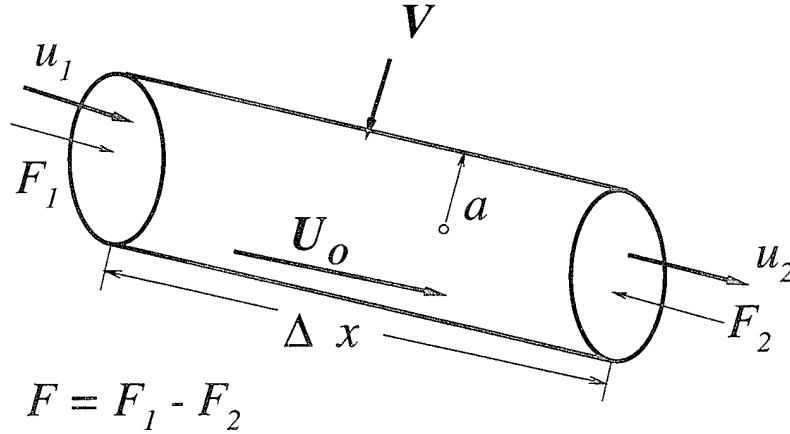
Figure 3-11: Control volume of the vortex core.

The resulting radial velocity V means that a sink of strength $2\pi a V$ per unit length is pulling fluid and sheet vorticity with it toward the core. In this calculation, the stretching effect of the vortex sheet is neglected. This model predicts a decreased pressure on the downstream end and a resultant increase of axial velocity and sink strength. The calculation is repeated until the radial velocity converges within a desired tolerance. The new vortex positions may now be calculated and the process

moves to the next downstream position. Figure 3-12 shows the geometry of the vortex sheet roll-up behind an elliptically loaded lifting line by applying the core and sink model. In this figure, the assumed core is also shown. In Figures 3-4 and 3-12, it is shown that the concentration of the vorticity does not give an effect on the geometry of the vortex sheet. Only the pressure and the trajectory of the tip vortex are affected. The calculation of pressure in the core is explained in Appendix B. The use of the strip theory model in the discrete vortex method provides savings on the computation time.

Y

0.5

CROSS SECTION At Z = 1.0 ft

ELLIPTIC LOADING, $\Gamma_o = 3ft^2/sec$
NO. OF ELEMENT = 19, $\Delta X = 0.025$
SPAN = 2.0 ft
BOUNDARY LAYER THICKNESS a = 0.05 ft

0.4

0.3

0.2

0.1

0.0

0.0   0.2   0.4   0.6   0.8 X

Figure 3-12: Cross section behind an elliptically loaded lifting line with a core and sink model. Predicted by using the model of Cummings[8].

The described core model predicts both the minimum pressure in the tip vortex core and the motion of the sheet with reasonable accuracy. On the other hand, the

velocity and pressure distributions on the body can not be accurately predicted with this model. In addition, this method is not fully three-dimensional.

3.2.2 Vortex Lattice Method

This method approximates the bound vortex sheet by a bound vortex lattice and the free vortex sheet by a set of segmented free vortex lines. Each element is associated with a horseshoe vortex. Discrete line vortices trail to infinite downstream along the trailing and side edges. Their alignment with the local flow direction provides the necessary boundary conditions on the vortex sheet. The strengths of vort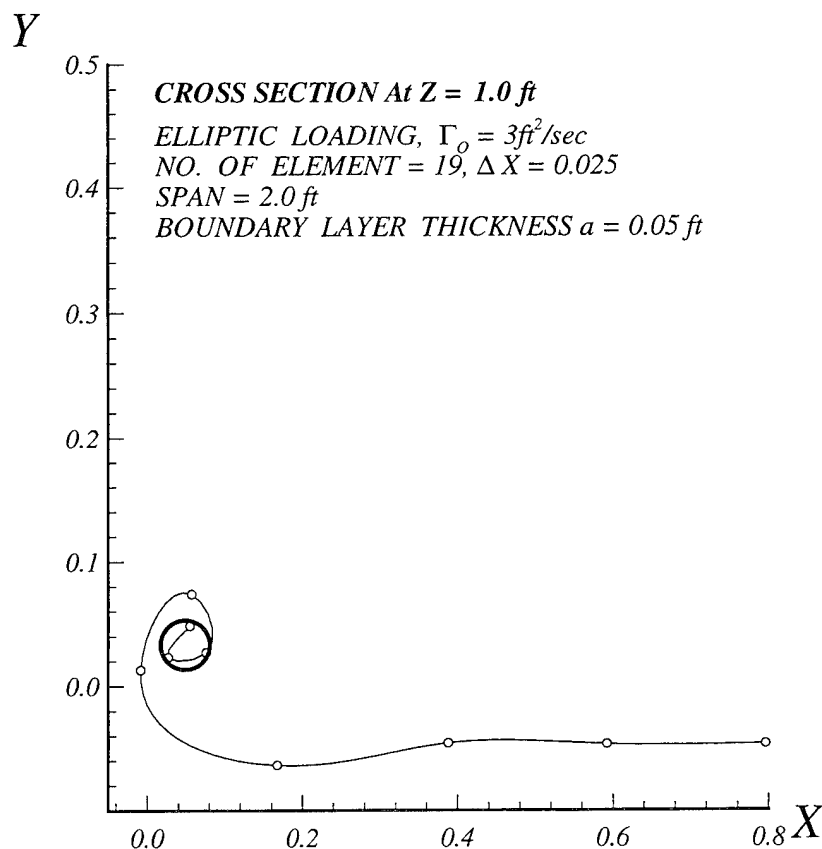ices are determined through the use of an iterative technique by imposing the kinematic condition at the midpoint of the 3/4 chord line of the elements. This method has been widely used and considerably improved by Kandil [30], Rom [65], Almosnino [1], and Keenan [31]. The results have shown that the model is rather crude and exhibits undesirable singular behavior. Even though overall forces are predicted well, the local velocity or pressure distribution on the body and the vortex sheet geometry are not sufficiently accurate. In addition, increasing the number of vortices makes the matter worse as shown by Rusak et. al [68].

3.2.3 Panel Method

In the panel method, the vortex sheet is modeled by a piecewise continuous dipole distribution, thus reducing the singular behavior, which is present in the case of line vortices. Many attempts have been made with this method, such as Suciu and Morino [72], Johnson et al. [29], and Hoeijmakers [21]. In this section, a new high-order panel method will be introduced.

Assuming that the circulation is given as $\Gamma(t)$ along the arclength (t) , then the dipole strength on the vortex sheet can be found from,

$$\gamma(t) \;=\; -\frac{d\Gamma}{dt} = u^+ - u^-$$

77

$$= \frac{\partial \phi^+}{\partial t} - \frac{\partial \phi^-}{\partial t} = \frac{\partial \Delta \phi(t)}{\partial t}$$

Therefore,

$$\Gamma(t) = -\Delta \phi(t)$$

where t is a parametric variable along the lifting line, and u^+ and u^- are velocities on the upper and lower surface, respectively as shown in Figure 3-13.
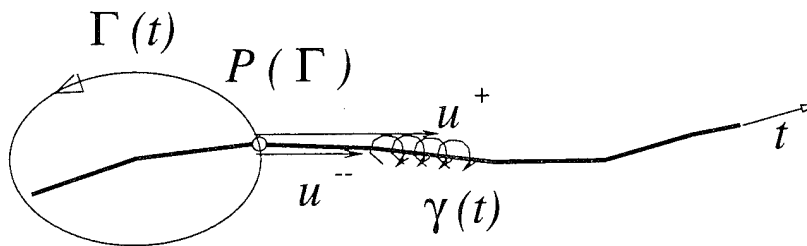
Figure 3-13: Velocity diagram on a lifting surface.

Equation (3.7) can be generalized to the three-dimensional problem by replacing the two-dimensional source expression $\log r$ and 2π by the three-dimensional source expression $1/r$ and -4π.

$$\boldsymbol{q} = \nabla\phi(x,y) = \frac{1}{4\pi} \int_S \Gamma(t)\nabla\left(\frac{\partial}{\partial n}\frac{1}{r}\right) \; dS \qquad (3.12)$$

where S is the surface of the vortex sheet.

The vortex sheet is divided into a number of panels as shown in Figure 3-14. The control point is set at the centroid of the panel. Then, equation (3.12) becomes

$$
\nabla \phi_i = \frac{1}{4\pi} \sum_j \int_{S_j} \Gamma(t_j) \nabla \left(\frac{\partial}{\partial n_j} \frac{1}{r_{i,j}} \right) \; dS_j \qquad (3.13)
$$

INITIAL GEOMETRY

AFTER 2-ND ITERATION

AFTER 3-RD ITERATION
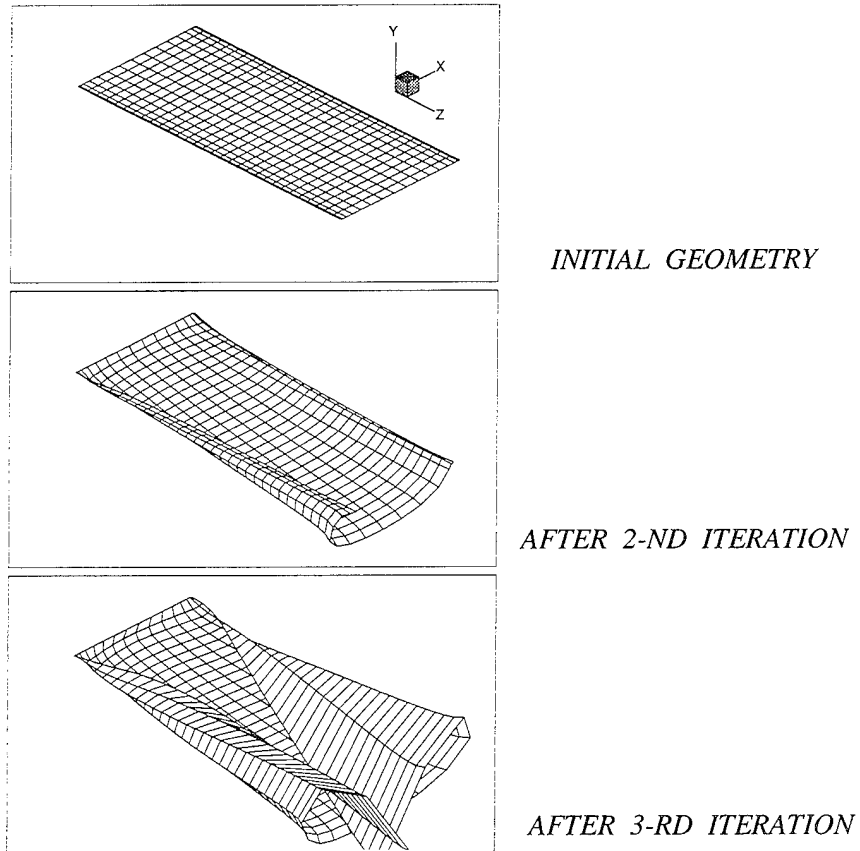
Figure 3-14: The geometry of the trailing vortex sheet for a lifting line with elliptic loading; $U_0 = 1$, $\Delta t = 0.15$ and $\Gamma_0 = 1.0 ft^2/sec$. The low-order panel method is used with 16 and 31 spanwise and streamwise number of panels, respectively. Notice divergence of roll-up shape at the 3-rd iteration.

If a planar quadrilateral panel and a constant strength dipole on the panel are assumed, equation (3.13) can be rewritten as

$$\nabla \phi_i \;\; = \;\; (u, v, w) = \frac{1}{4\pi} \sum_j \Gamma(t_j) \int_{S_j} \nabla \left(\frac{\partial}{\partial n_j} \frac{1}{r_{i,j}} \right) \; dS_j \qquad (3.14)$$

The integrals in equation (3.14) can be computed analytically by using the expressions developed by Newman [63].
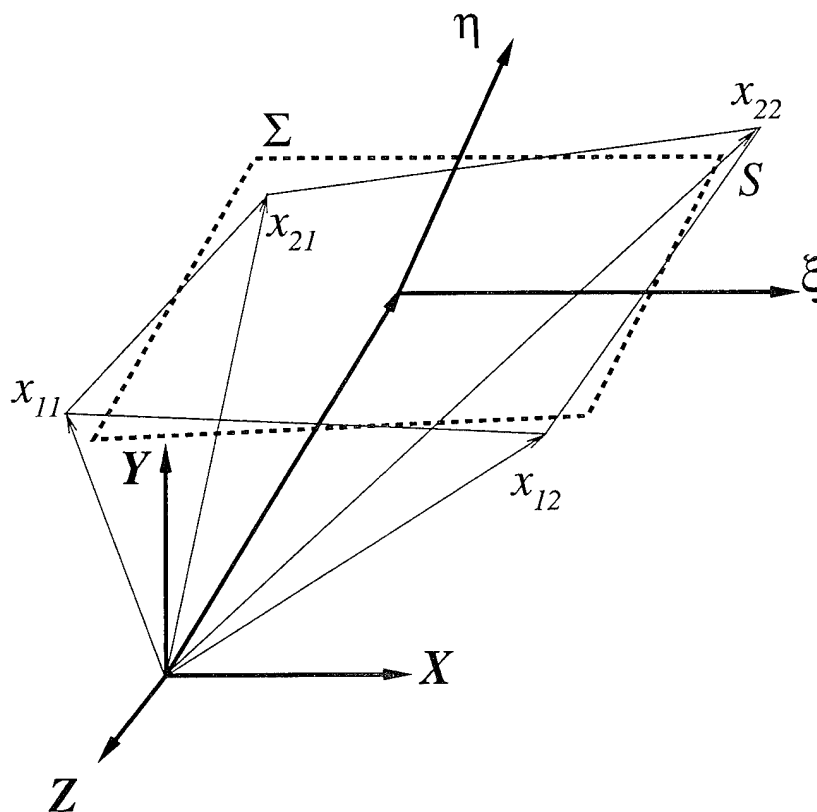
Figure 3-15: The geometry of hyperboloidal panel.

The velocities at the control points on the vortex sheet are computed first , and the velocities at the edges of the panels are extrapolated from those at the control points. Then the panel moves with velocity $(u + U, v + V, w + W)$, where (U, V, W) are the components of the incoming velocity.
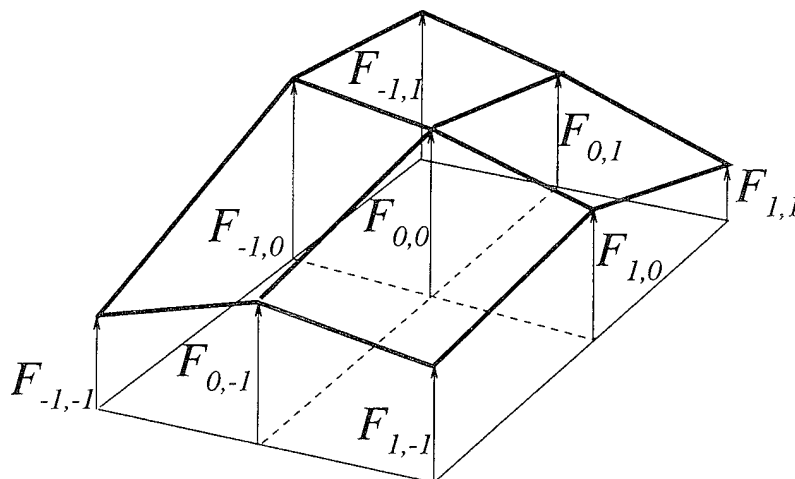
Figure 3-16: Bi-quadratic dipole distribution on a panel with nine nodes.

This procedure is repeated until the geometry of the vortex sheet converges. The result for a lifting line with elliptic loading, is shown in Figure 3-14. The low-order panel method has failed after three iterations. It seems that the planar quadrilateral panel can not model the highly rolled-up region accurately, due to the discontinuity (gap) in geometry and in strength of adjacent panels. As a more accurate and reliable tool, a hyperboloidal panel and a high order strength of the dipole are used.

A hyperboloidal panel is defined in Figure 3-15. Surface Σ is a hyperboloidal surface determined by four vertices $x_{1,1}$, $x_{1,2}$, $x_{2,1}$, $x_{2,2}$, and the surface S is a projected

surface on a local coordinates (ξ, η). All the points on the panel can be expressed as

$$\vec{x}(\xi, \eta) \;=\; a_0 + a_1\xi + a_2\eta + a_3\xi\eta$$

$$-1 \le \xi \le 1, \quad -1 \le \eta \le 1 \tag{3.15}$$
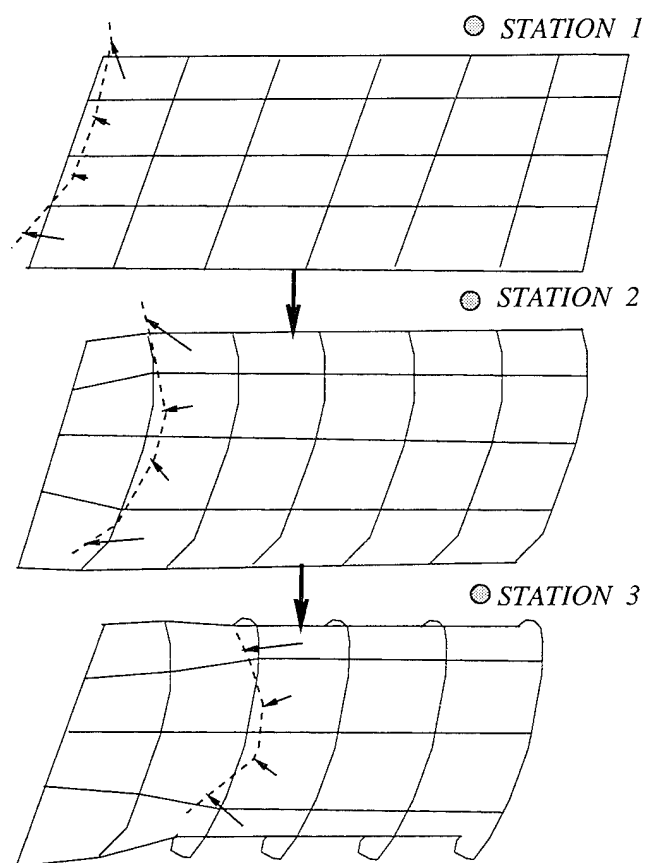
Figure 3-17: The first iteration of the iteration scheme.

The vertices thus can be expressed as follows ;

$$
\begin{bmatrix} \vec{x}_{1,1} \\ \vec{x}_{1,2} \\ \vec{x}_{2,1} \\ \vec{x}_{2,2} \end{bmatrix} = \begin{bmatrix} 1 & -1 & -1 & 1 \\ 1 & 1 & -1 & -1 \\ 1 & -1 & 1 & -1 \\ 1 & 1 & 1 & 1 \end{bmatrix} \begin{bmatrix} a_0 \\ a_1 \\ a_2 \\ a_3 \end{bmatrix}
$$
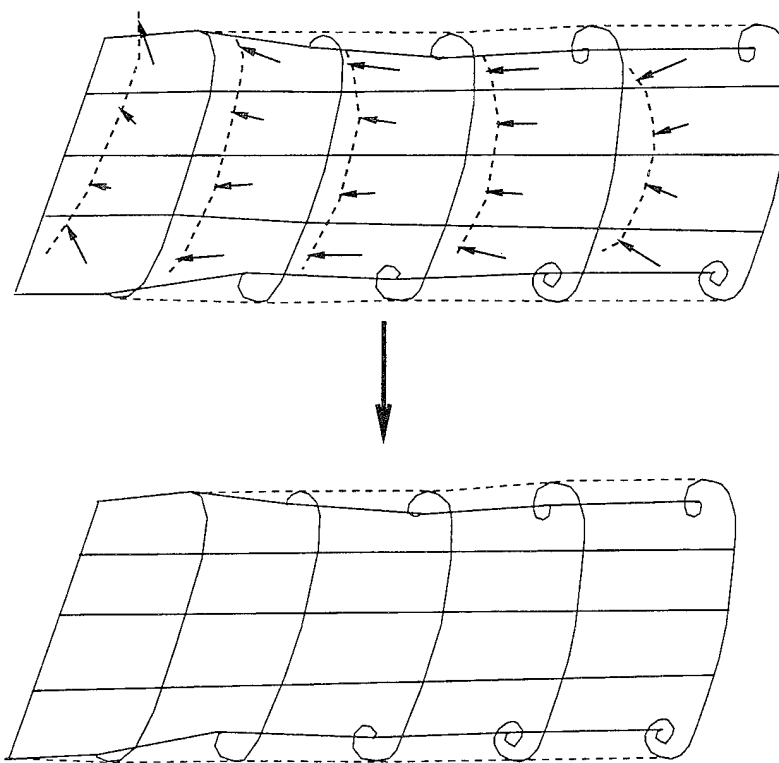
Figure 3-18: Second or higher iteration of the scheme.

By inverting this matrix, a_0, a_1, a_2 and a_3 can be obtained from the vertices, (Hsin

$$
\begin{bmatrix} a_0 \\ a_1 \\ a_2 \\ a_3 \end{bmatrix} = \frac{1}{4} \begin{bmatrix} 1 & -1 & -1 & 1 \\ 1 & 1 & -1 & -1 \\ 1 & -1 & 1 & -1 \\ 1 & 1 & 1 & 1 \end{bmatrix} \begin{bmatrix} \vec{x}_{1,1} \\ \vec{x}_{1,2} \\ \vec{x}_{2,1} \\ \vec{x}_{2,2} \end{bmatrix}
$$

A bi-quadratic dipole strength is assumed on the panel. The strength of the dipole in the local coordinate system can then be expressed as

$$
\Gamma(\xi, \eta) = b_0 + b_1\xi + b_2\eta + b_3\xi\eta + b_4\xi^2 + b_5\eta^2 + b_6\xi\eta^2 + b_7\xi^2\eta + b_8\xi^2\eta^2 \tag{3.16}
$$

The coefficients b_i can be determined from the dipole strengths at the nine node points on the panel, as shown in Figure 3-16. The 9×9 matrix equation, which must be solved, is

$$
\begin{bmatrix} F_{-1,-1} \\ F_{-1,0} \\ F_{-1,1} \\ F_{0,-1} \\ F_{0,0} \\ F_{0,1} \\ F_{1,-1} \\ F_{1,0} \\ F_{1,1} \end{bmatrix} = \begin{bmatrix} 1 & -1 & 1 & -1 & 1 & -1 & 1 & -1 & 1 \\ 1 & -1 & 1 & 0 & 0 & 0 & 0 & 0 & 0 \\ 1 & -1 & 1 & 1 & -1 & 1 & 1 & -1 & 1 \\ 1 & 0 & 0 & -1 & 0 & -1 & 1 & 0 & 0 \\ 1 & 0 & 0 & 0 & 0 & -1 & 0 & 0 & 0 \\ 1 & 0 & 0 & 1 & 0 & -1 & 1 & 0 & 0 \\ 1 & 1 & 1 & -1 & -1 & -1 & 1 & 1 & 1 \\ 1 & 1 & 1 & 0 & 0 & 0 & 0 & 0 & 0 \\ 1 & 1 & 1 & 1 & 1 & 1 & 1 & 1 & 1 \end{bmatrix} \begin{bmatrix} b_0 \\ b_1 \\ b_2 \\ b_3 \\ b_4 \\ b_5 \\ b_6 \\ b_7 \\ b_8 \end{bmatrix}
$$

Now, from equations (3.15) and (3.16), equation (3.13) can be rewritten as,

$$
\nabla \phi_i = \frac{1}{4\pi} \sum_j \int_{S_j} (b_0 + b_1\xi + b_2\eta + b_3\xi\eta + b_4\xi^2 + b_5\eta^2 + b_6\xi\eta^2 + b_7\xi^2\eta
$$
$$
+ b_8\xi^2\eta^2)\nabla \left(\frac{\partial}{\partial n_j} \frac{1}{r_{i,j}} \right) dS_j \tag{3.17}
$$

84

The calculation of the integrals in equation (3.17) over the hyperboloidal panel (S_j), is described in Appendix C. The following iteration scheme is introduced in order to satisfy the force-free condition on each panel in the vortex sheet. To accelerate the iteration process, an idea similar to that in over-relaxation schemes is adopted in the first iteration (Nagati et al. [61]). Namely, in the first iteration the calculation of the wake surface is proceeding from the first station to the last section downstream of the trailing edge as follows (shown also schematically in Figure 3-17).
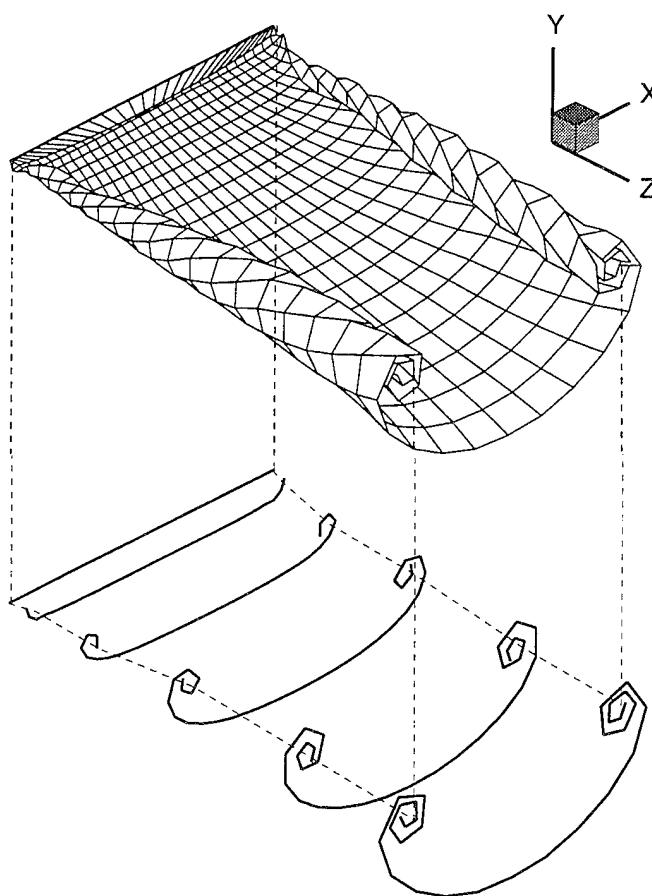
Figure 3-19: The geometry of vortex sheet behind a lifting line with elliptic loading. Predicted by the present method.

- The total velocities at the control points of the current row of the panels are computed from equation (3.17). The velocity at the edge of the vortex sheet is computed from extrapolation.

- Use these velocities to find new location of panels on the current row.

- The panels downstream of the current row are moved by the same amount as those at the current row.

- Repeat the computation until the last row of panels.

At the second or higher iteration, the procedure is altered due to the fact that the geometry of the upstream vortex sheet will be affected by the relocation of the vortex sheet downstream, which is ignored in the first iteration. The following steps are used, as also shown in Figure 3-18,
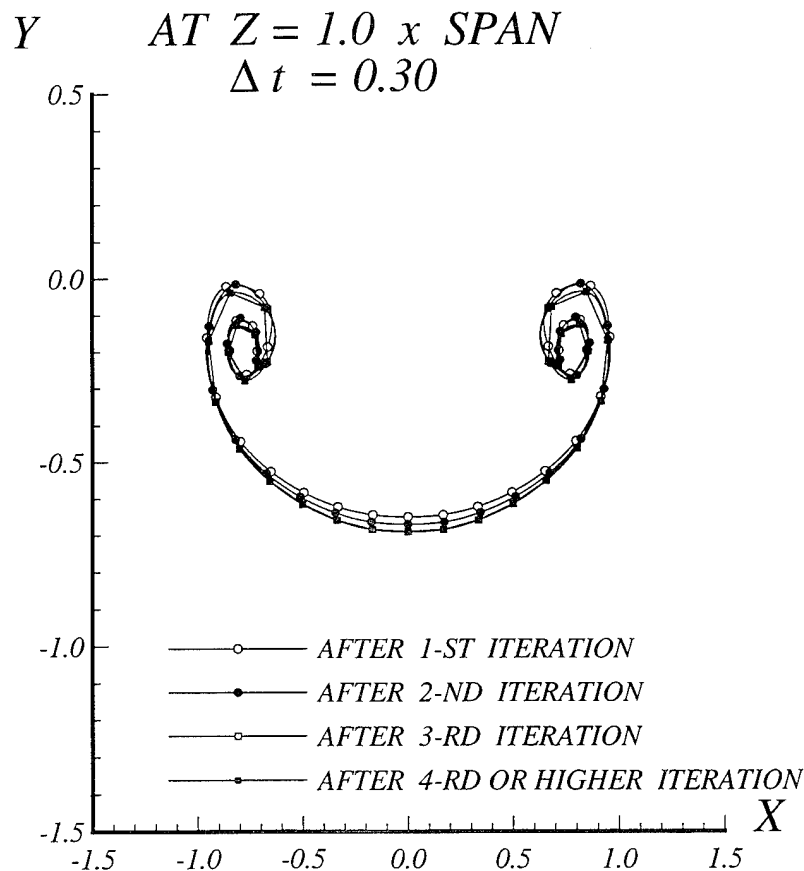
Figure 3-20: Shape of the vortex sheet with number of iterations.

- Calculate the total velocities at all the control points in the vortex sheet.

- Move all the panels simultaneously and find the new location of the vortex sheet.

- Repeat the previous steps until the vortex sheet geometry is converged.

To maintain the accuracy of the spatial discretization for a stretching vortex sheet, a rediscretization scheme is applied as the roll-up region increases. The discretization scheme has to be refined in regions where large variations in geometry or dipole distribution appear during the computation.

Figure 3-21: Convergence test of a lifting line with elliptic loading with respect to the number of spanwise panels.

To accommodate these requirements, the adapted curvature-dependent panel scheme is used at each iteration, similar to that used in the two-dimensional panel method as

explained in section 3.1.3. The basic panel size Δ_{max} is chosen such that the desired degree of accuracy in regions where no large variations occur is ensured. The second parameter θ_{max} then ensures that at highly curved parts of the sheet the panel size is reduced so that in each region the accuracy is maintained. Usually θ_{max} is chosen such that a circle having a radius equal to the radius of curvature is represented by 12-18 panels. This numerical scheme is applied to a lifting line with elliptic loading. The resulting geometry of the vortex sheet roll-up is shown in Figure 3-19. Note that this method predicts the vortex sheet roll-up very smoothly with more turns (i.e. at larger distance from the trailing edge) than that in the discrete vortex method.
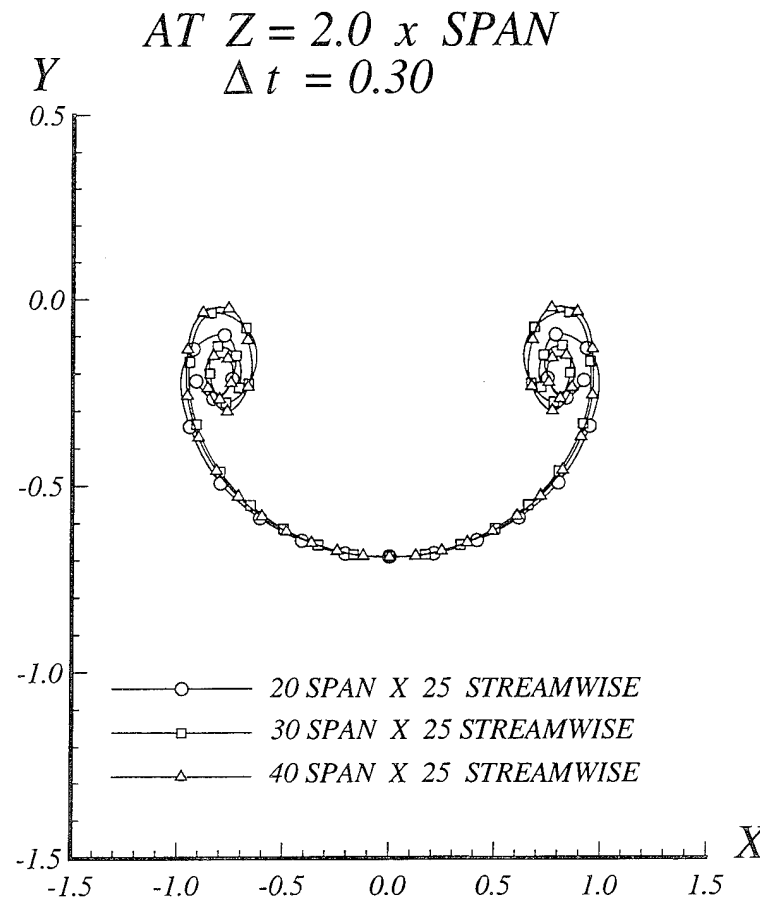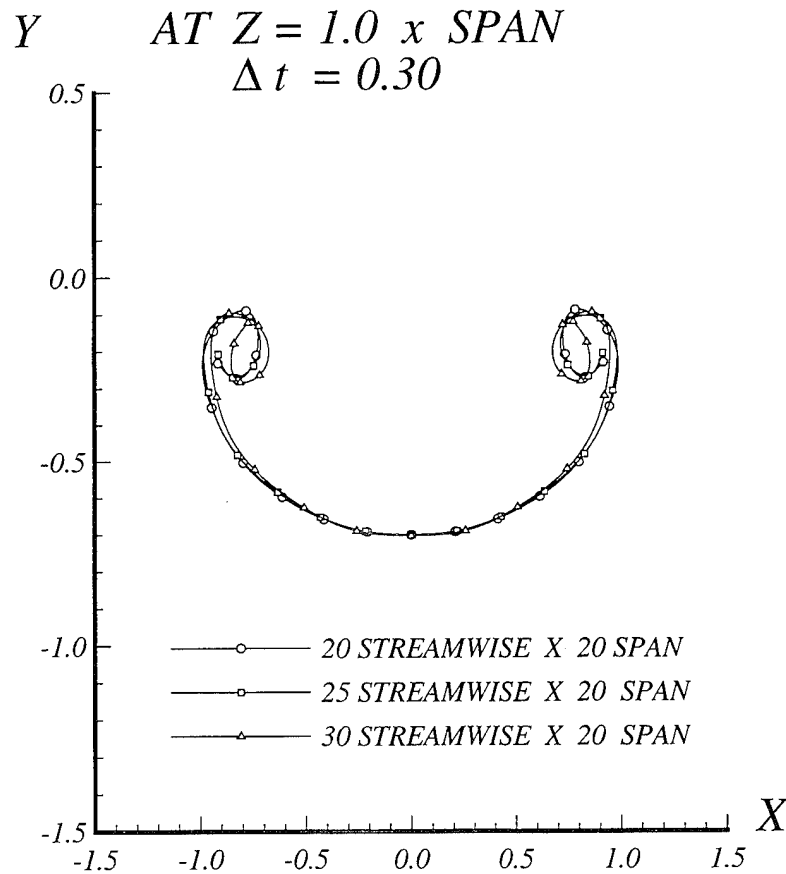

Figure 3-22: Convergence test of a lifting line with elliptic loading with respect to the number of streamwise panels.

The difference among the iterations is shown in Figure 3-20. This figure shows that

two iterations is enough usually to get a converged result. Finally, more convergence tests are shown in Figures 3-21 and Figure 3-22. Note that as the number of panels along the spanwise and streamwise direction increases, the geometries of the vortex sheet appear to converge to a limit. It can be concluded that the present high-order panel method predicts a smooth and reliable (*convergent*) geometry of the vortex sheet roll-up in a computationally efficient manner.

Chapter 4

The FLAG with the Wake Sheet Roll-Up

In Chapter 2, the flow adapted grid was incorporated in the panel method for lifting surface flows. It was shown that using the flow adapted grid in the panel method, the numerical results for a highly skewed propeller and a propeller with a large tip chord, especially in the tip region, were improved substantially. However, the flow adapted grid does not include the effect of a wake sheet roll-up, which changes the trajectory of the tip vortex as well as the pitch of the wake sheet. In this chapter, the flow adapted grid with the effect of the wake sheet roll-up will be incorporated in the panel method. In calculating the wake sheet roll-up, the higher order panel described in the previous chapter will be used. The flow adapted grid will be constructed by using the geometry of the wake sheet roll-up, in an iterative sense.

The essential elements of the present flow model, as mentioned in Appendix B, are : the lifting body, the trailing wake sheet, the sheet emerging from the tip (sheath) and the roll-up core fed by the tip vortex sheet. On each of these elements, the following boundary conditions must be imposed:

- The body surface is impermeable.

- The wake sheet cannot support a pressure difference and is impermeable as well.

- The Kutta condition is imposed along the trailing edge of the blade.

The panel method will be modified to satisfy the boundary conditions on the body as well as in the wake sheet. The enhanced panel method is expected not only to improve the accuracy of the predicted pressure distributions at the blade tip, but also to provide the foundation for predicting the tip vortex evolution.
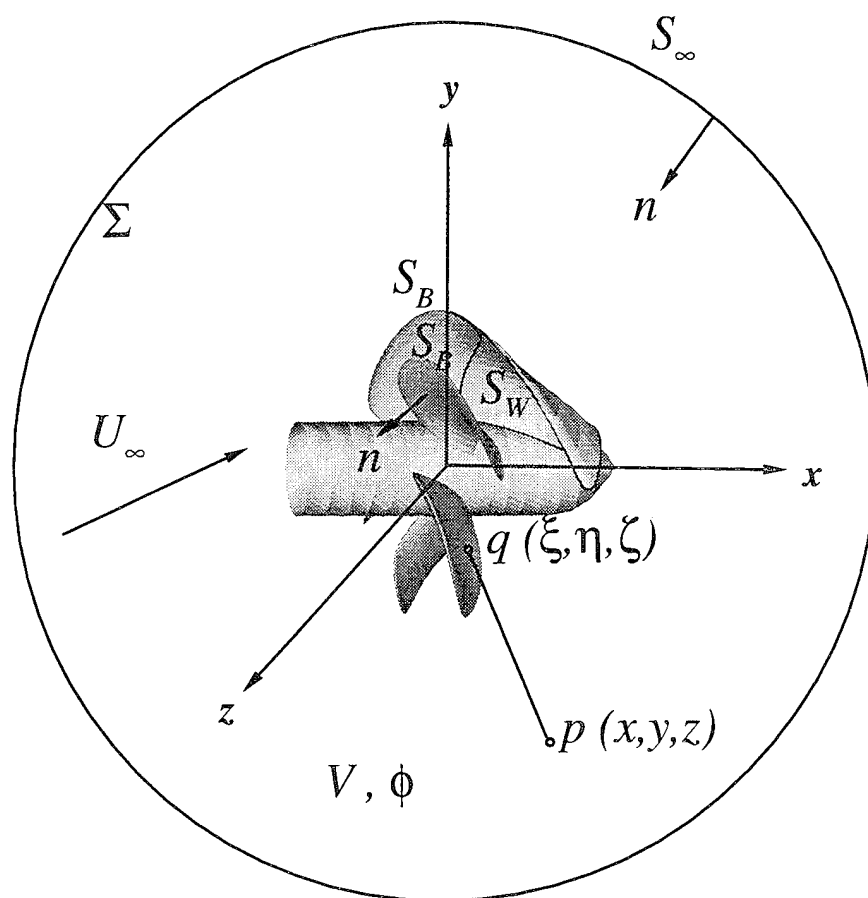
4.1 Mathematical Formulation

Figure 4-1: A control volume for a multidomain problem.

The flow is assumed to be inviscid, incompressible and irrotational everywhere, except in the thin wake sheet. The flow velocity can be written as a superposition of the incoming flow U_∞, the velocities induced by the body, V_B, and by the wake sheet,

V_W. The velocity vector, thus has the form

$$V = U_\infty + V_B + V_W = U_\infty + \nabla\phi$$

where ϕ is an induced potential due to the body and the wake.

In the fluid domain Σ, as shown in Figure 4-1, the potential satisfies the Laplace equation ;

$$\nabla^2\phi \;=\; 0. \tag{4.1}$$

Denoting the body surface as S_B, the kinematic boundary condition on S_B is

$$\nabla\phi \cdot n \;=\; -U_\infty \cdot n \tag{4.2}$$

Applying the Green's theorem with the Laplace equation (4.1), the induced velocity can be expressed by ;

$$
\begin{aligned}
\nabla_p\phi(p) \;=\; & \frac{1}{4\pi}\int\!\!\int_{S_B}\left[\phi(q)\frac{\partial}{\partial n_q}\nabla\frac{1}{R(p;q)} - \frac{\partial\phi}{\partial n_q}\nabla\frac{1}{R(p;q)}\right]dS \\
& + \frac{1}{4\pi}\int\!\!\int_{S_W}\Delta\phi(q)\frac{\partial}{\partial n_q}\nabla\frac{1}{R(p;q)}dS
\end{aligned}
\tag{4.3}
$$

where q is a variable point in the integration and p is a fixed point which may be located anywhere in the space. S_B is the propeller blade and S_W is the wake surface.

Equation (4.3) shows that the induced velocity due to the body and the wake can be calculated by distributing dipoles and sources on the body and dipoles in the wake.

4.2   Discrete Formulation

For the numerical implementation, the propeller surface and the wake sheet are discretized into hyperboloidal panels [24]. Constant strength sources and dipoles are

92

distributed on each panel on the body and bi-quadratic strength dipoles on each panel in the wake. The effect of the hub is also included by distributing panels on the hub surface. A collocation method is applied, with the control points being the centroids of the panels. Using equations (3.16) and (4.3), the discretized form of the induced velocity becomes :

$$
\begin{aligned}
\nabla \phi_i = & \sum_{K=1}^{N_{BLADE}} \sum_{j=1}^{N_{PANEL}} a_{i,j}^K \phi_j^K - \sum_{K=1}^{N_{BLADE}} \sum_{j=1}^{N_{PANEL}} b_{i,j}^K \frac{\partial \phi_j^K}{\partial n} \\
& + \sum_{K=1}^{N_{BLADE}} \sum_{m=1}^{M} \sum_{l=1}^{N_W} W_{i,m,l}^K \\
a_{i,j} = & \frac{1}{4\pi} \int \int_{S_j} \frac{\partial}{\partial n_j} \nabla \frac{1}{R_{i,j}} dS_j \\
b_{i,j} = & \frac{1}{4\pi} \int \int_{S_j} \nabla \frac{1}{R_{i,j}} dS_j \\
W_{i,m,l} = & \frac{1}{4\pi} \int \int_{S_{m,l}} (b_0 + b_1 \xi + b_2 \eta + b_3 \xi \eta + b_4 \xi^2 + b_5 \eta^2 + b_6 \xi \eta^2 + \\
& b_7 \xi^2 \eta + b_8 \xi^2 \eta^2) \frac{\partial}{\partial n_{m,l}} \nabla \frac{1}{R_{i,m,l}} dS_{m,l}
\end{aligned}
\tag{4.4}
$$

where N_{BLADE} is the number of blades and N_{PANEL} is the total number of panels on a blade, which has N chordwise panels and M spanwise panels (i.e. $N_{PANEL} = N \times M$). N_W is the number of streamwise panels on each strip in the wake.

The influence coefficients $a_{i,j}$ and $b_{i,j}$ are defined as the velocities induced at panel i by a unit strength dipole and source, respectively, located at panel j on blade K. The wake influence coefficient $W_{i,m,l}^K$ is defined similarly, as the induced velocity at panel i due to the unit dipole at (m, l) in the wake on the blade K. The numerical computation of these coefficients are explained in Appendix C. The strength of the source $(\frac{\partial \phi_j}{\partial n}^K)$ and the dipole (ϕ_j^K) on the body and the dipole $(\Delta \phi_{m,l}^K)$ in the wake can be found from the typical panel method after applying the kinematic condition on the body and the iterative pressure Kutta condition at the trailing edge [42], [24], in which case the geometry of the trailing wake sheet is assumed to be aligned with the inflow.

93

4.3 Numerical Procedure

In order to include the effect of the wake sheet roll-up in the flow adapted grid, the following method is implemented. The method proceeds by computing the induced velocities at the control points in the wake, as follows.
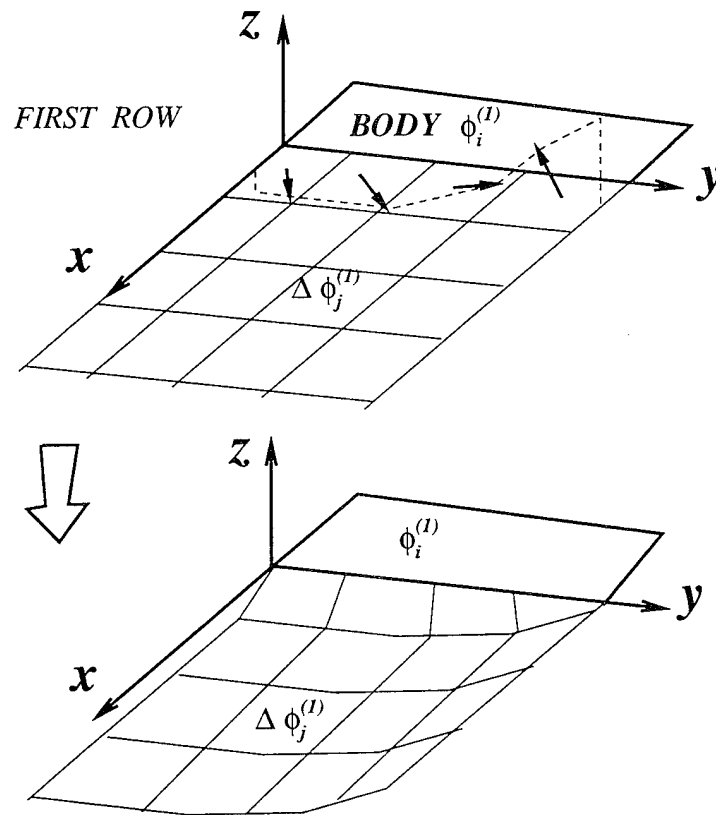

Figure 4-2: The first iteration for the FLAG with a wake sheet roll-up. Velocity vectors are evaluated at the control points.

1. Solve a boundary value problem by using the BEM with a geometry of the trailing wake sheet, which is aligned with the inflow. In the case of a wing, the

trailing wake will be planar or cylindrical (with very high curvature) and have the same direction as the inflow. In the case of a propeller, the trailing wake will be helicoidal without any contraction at the tip.

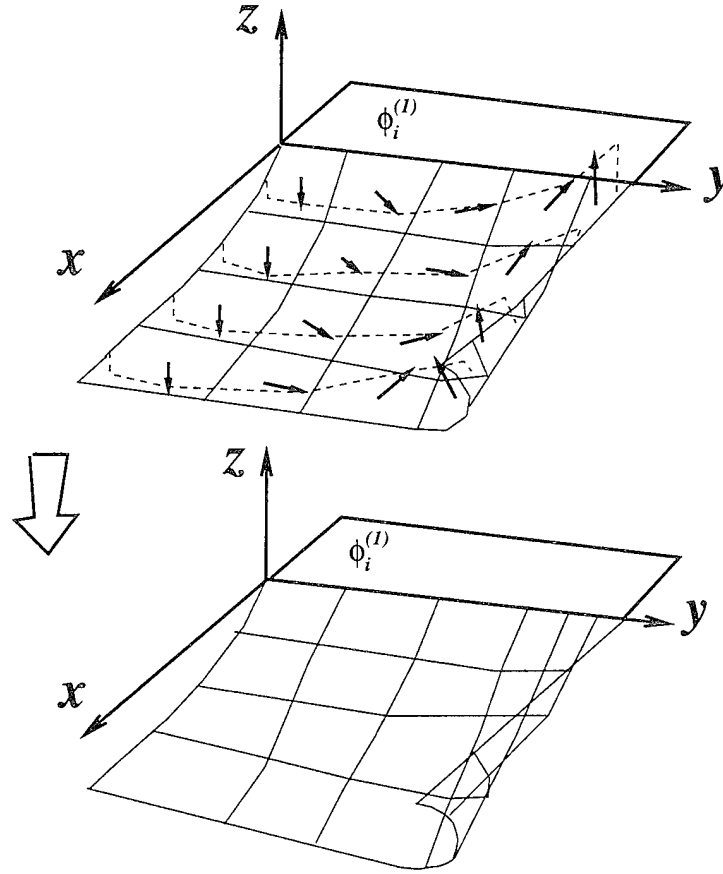Figure 4-3: The second or higher iteration. Velocity vectors are at the control points.

2. Compute the induced velocities ($\nabla \phi_i$) at the control points of the first row of panels in the wake from the equation (4.4). Then move the first row of panels to the second row by using a first order Euler scheme, which is given as,

$$x_{m,2} = x_{m,1} + (U_\infty + \nabla\phi_{m,1}) \cdot \frac{\Delta t_1}{2}$$
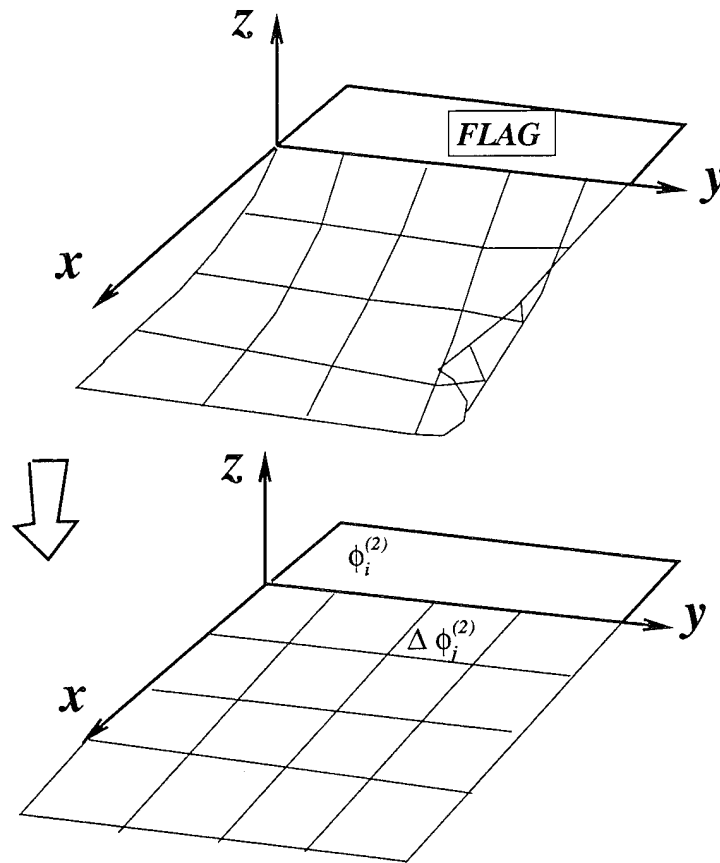
Figure 4-4: Construct FLAG with wake sheet roll-up from previous iteration.

3. Adjust the downstream wake shape so that it has the same shape as the wake at the previous row. In other words, set $y_{k,j} = y_{i,j}$ and $z_{k,j} = z_{i,j}$ for $k = i+1, i+2, \cdots, N_{W+1}$, as shown in Figure 4-2. Also check the panel size. If the panel size is greater than the criteria Δ_{max}, then rediscretize the panel.

4. Repeat steps 2. and 3. until the last row of the panels. With this initial geometry, compute induced velocities at all control points in the wake and move the panels all together as shown in Figure 4-3. Repeat this calculation until the geometry of the wake sheet is converged. Usually, two iterations have

been found to be enough.

```
┌─────────────────────────────────────────────────┐
│  RUN PANEL CODE WITH CONVENTIONAL GRID          │
└─────────────────────────────────────────────────┘
```

COMPUTE THE INDUCED VELOCITY
$\vec{u}$ FOR STATION $i = 1$

FIND NEW POSITION VECTORS
$x_{2,j} = x_{1,j} + 0.5\,(U_\infty + \nabla_x \phi)\,\Delta t_1$

SET $y_{kj} = y_{ij}$ & $z_{kj} = z_{ij}$ for $k = i+1, \dots, N_w+1$
REPEAT for STATION $i = 3, 4, \dots, N_w+1$

REPEAT PREVIOUS TWO STEPS for
STATION $i = 2, 3, 4, \dots, N_w+1$

COMPUTE u for ALL STATIONS
& MOVE PANELS ALL TOGETHER

NO

CONVERGE ?

YES

CONSTRUCT FLAG &
RUN PANEL CODE WITH FLAG

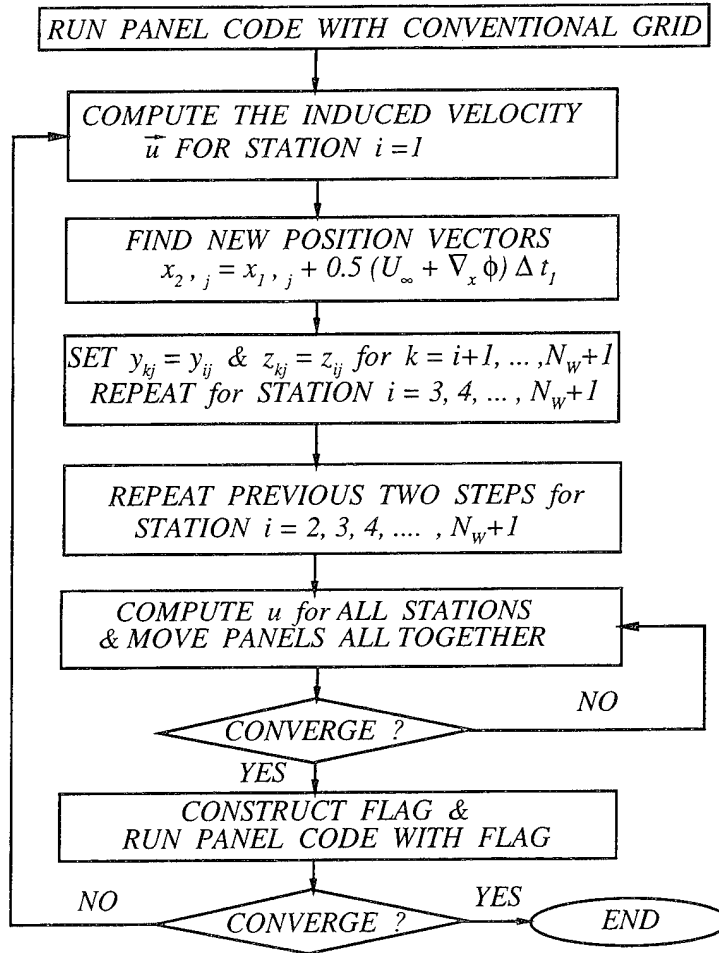NO   YES

CONVERGE ?   END

Figure 4-5: Flow diagram for construction of the FLAG with wake sheet roll-up in three dimensions.

5. With the converged wake sheet, construct FLAG and solve the BEM with the known wake sheet roll-up surface, to get the potentials on the body and potential jumps in the wake, as shown schematically in Figure 4-4.

6. Repeat steps 2 to 5 until the geometry of the wake sheet is converged.

The summary of this procedure is shown in Figure 4-5. In the calculation of the wake sheet roll-up, it usually takes two iterations with given potentials on the body and

the potential jumps in the wake. On the other hand, for the construction of FLAG with wake sheet roll-up, two iterations are usually enough. As for the CPU, it takes about three times as long as the panel method without wake sheet roll-up. In the next chapter, this method will be applied to several wing and propeller geometries The sensitivity of the results to the discretization parameters will be investigated, and results of the method will be validated against existing experiments.

Chapter 5

Analysis of Computational Results

In the earlier chapters of this thesis, the flow adapted grid and a new wake sheet roll-up computation method were described and incorporated in the panel method. In this chapter, the new method will be applied to a number of lifting surface configurations. Two groups of applications will be presented. The first group is applications for a series of wings and the second group is applications for a series of propellers. In order to validate the method, the results will be compared to those from other numerical methods and to published experimental measurements.

5.1 Wing

In Chapter 3, a new higher order panel method has been developed in order to predict the geometry of the vortex sheet roll-up in three dimensions. The method was applied to a lifting line with elliptic loading. In this section, in order to examine the body effect on the geometry of the vortex sheet roll-up, the method will be applied to a series of wings.

5.1.1 Rectangular Wing

The method is first applied to a rectangular wing of aspect ratio AR=8 at 10 degrees angle of attack, as shown in Figure 5-1. In this calculation, the panels in the wake

are distributed using cosine spacing in the spanwise and the streamwise directions to emphasize the details near the body and the tip. Following the procedure explained in the last chapter, the wake sheet roll-up is obtained as shown in Figure 5-1.
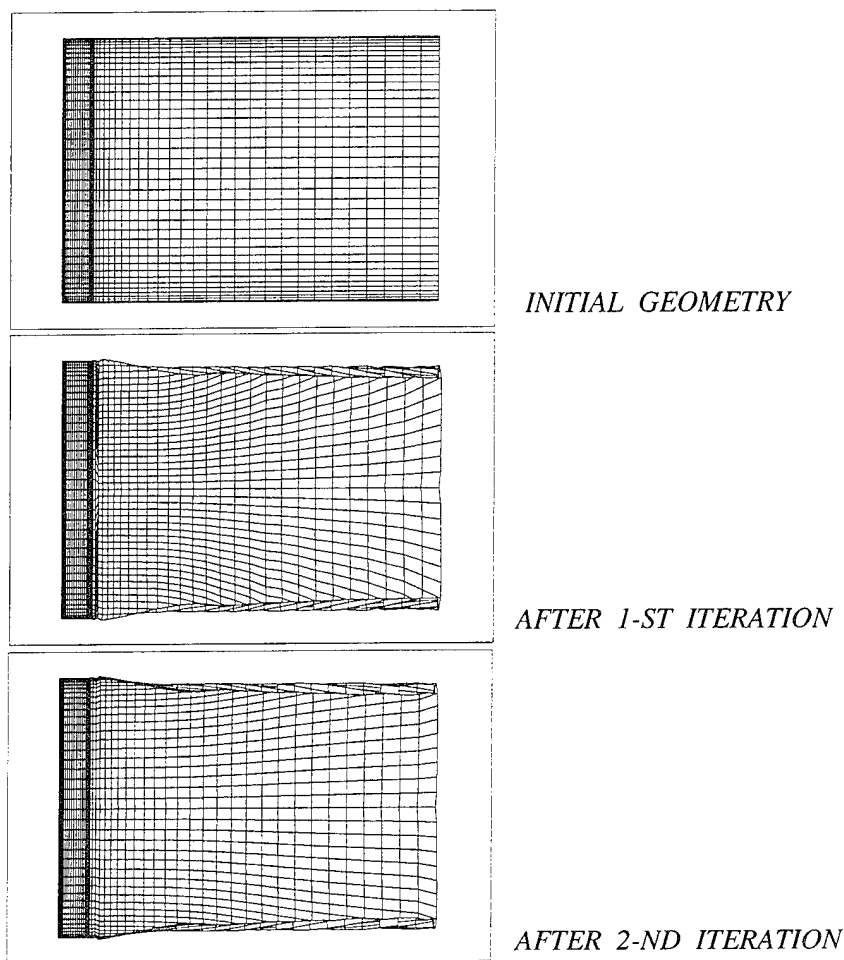

INITIAL GEOMETRY

AFTER 1-ST ITERATION

AFTER 2-ND ITERATION

Figure 5-1: Trailing wake sheet behind a rectangular wing; $AR = 8$, $\alpha = 10^o$, $(\tau/c)_{max} = 0.01$. 40 chordwise and 30 spanwise panels on the wing and 20 streamwise panels in the wake. Constant thickness distribution in spanwise direction.

The wing is discretized into 40 chordwise and 20 spanwise panels. The trailing wake sheet is discretized into 20 spanwise and 20 streamwise panels. In this particular case, it took two iterations for the wake shape to converge. The geometry of the wake sheet at each iteration is also shown in Figure 5-1. The geometries after the first and

second iterations are practically identical to each other. The roll-up pattern shown in the bottom of Figure 5-2, has a smooth appearance. However, near the tip at the trailing edge of the wing, there is a non-smooth behavior.
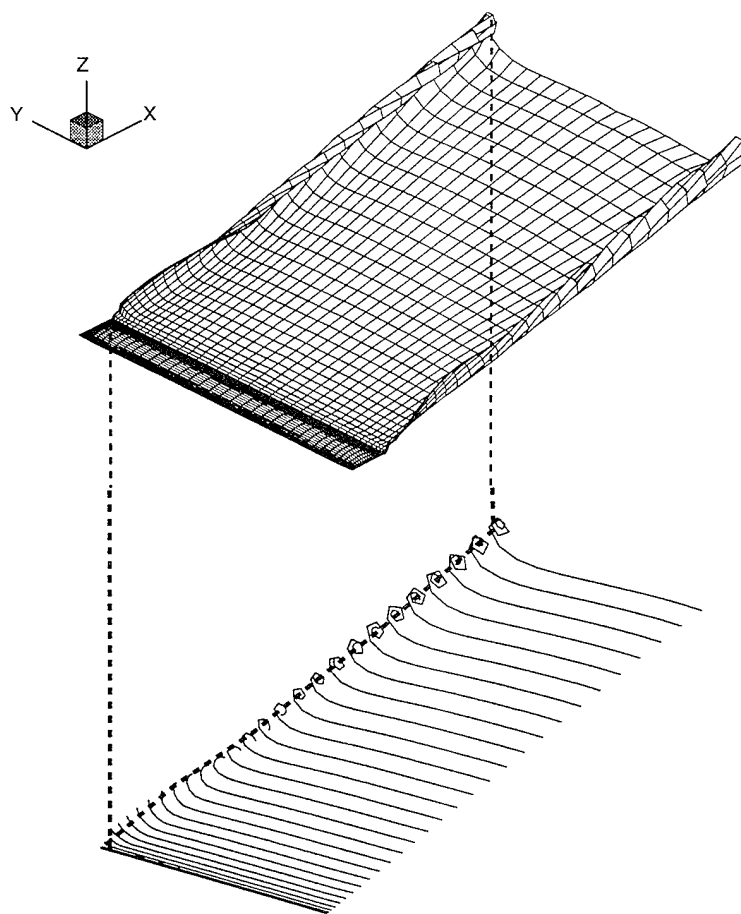

Figure 5-2: The geometry of the trailing wake sheet and its cross sections.

That may be because the position of the tip is set at the trailing edge of the tip chord. In reality, the position of the tip would be somewhere along the tip chord. The present method cannot handle the side edge separation yet. The geometry of the wake sheet is compared to that from Suciu and Morino's method [72] at two axial positions, which are at 4 and 9 times the wing chord downstream from the trailing edge. Suciu

and Morino's method uses constant strength singularities and hyperboloidal panels on the wing and in the wake.
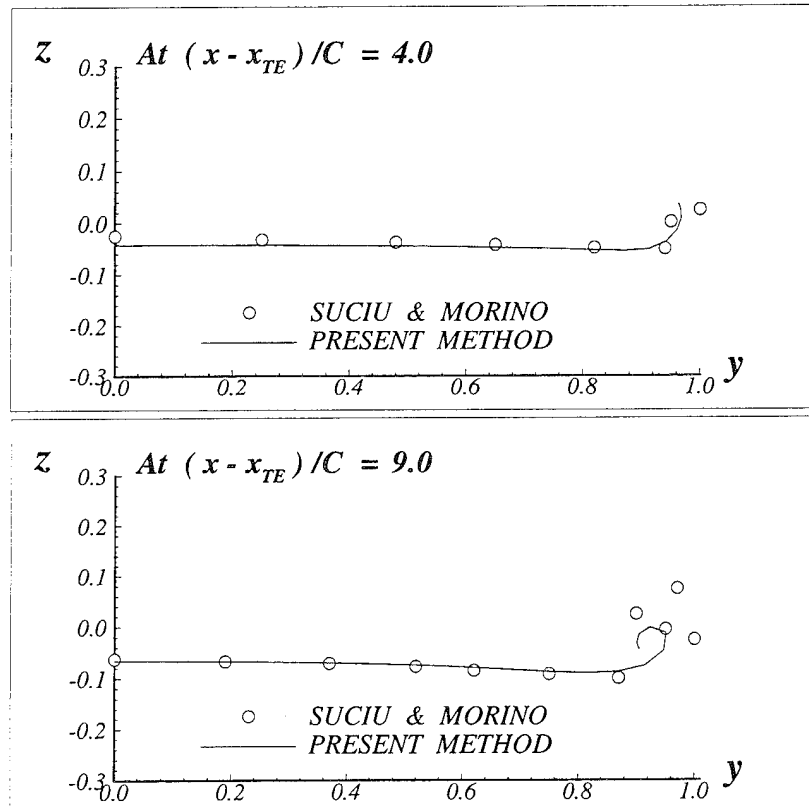

Figure 5-3: Wake cross section at $(x - x_{TE}) = 4$ and $9 \times c$ for a rectangular wing with 1% maximum thickness/chord ratio, $AR = 8$, $\alpha = 10^o$.

The comparison is shown in Figure 5-3. Even though the size of the two roll-up regions is different, the center of the core and the geometry of the rest of the wake sheet shows good agreement.

5.1.2 An Elliptic Wing

In Chapter 2, the flow adapted grid without the wake sheet roll-up, was applied to several wings and propellers, and validated via convergence and consistency tests.
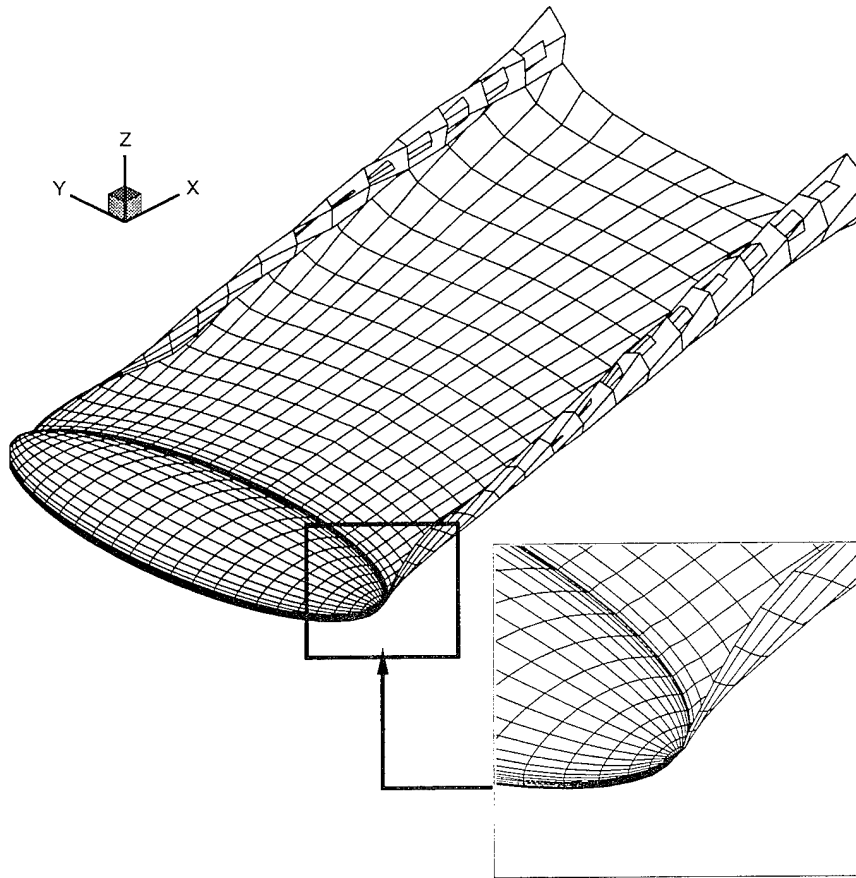

Figure 5-4: The geometry of the trailing wake sheet roll-up behind an elliptic wing with 15% maximum thickness/chord ratio, $\alpha - \alpha_{ideal} = 6^o$.

To examine the effect of the vortex sheet roll-up on the flow adapted grid, an elliptic wing is considered. The cross section of the wing has a $NACA66_2 - 415$ shape with an a=0.8 mean camber line. The ideal angle of attack (α_{ideal}) is -2.5^o and the maximum thickness/chord ratio is 15%. The aspect ratio is 3. The resulting flow

adapted grid on the wing and the geometry of the wake sheet roll-up are shown in Figure 5-4.
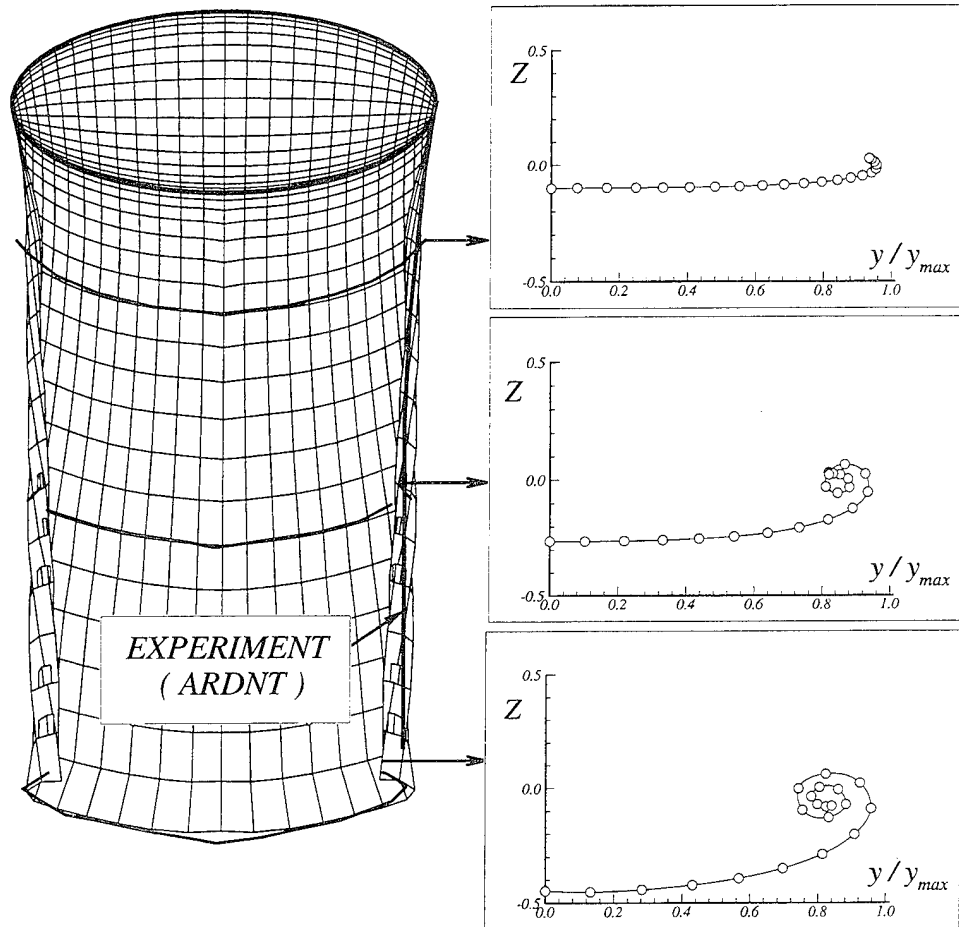

Figure 5-5: The tip vortex trajectory of an elliptic wing with 15% maximum thickness/chord ratio, $\alpha - \alpha_{ideal} = 12.5^o$; the thick line is the tip vortex trajectory from the experiment given by Arndt(1991).

The tip is moved backward along the trailing edge and the grid lines on the wing seems to align well with those in the wake. In the close-up picture near the tip of the wing shown in Figure 5-4, the tip vortex is shown to depart from the tip of the wing and to roll up very smoothly. In this case, 40 spanwise, 40 chordwise and 20 streamwise panels are used on the wing and in the wake. It took two iterations for the

104

converged geometry of the wake sheet roll-up and three iterations for the flow adapted grid. Figure 5-5 shows the cross sections of the wake sheet roll-up at three different locations. In the same figure, the numerical tip vortex trajectory is compared to that from the experiment, which is given by Arndt [2].
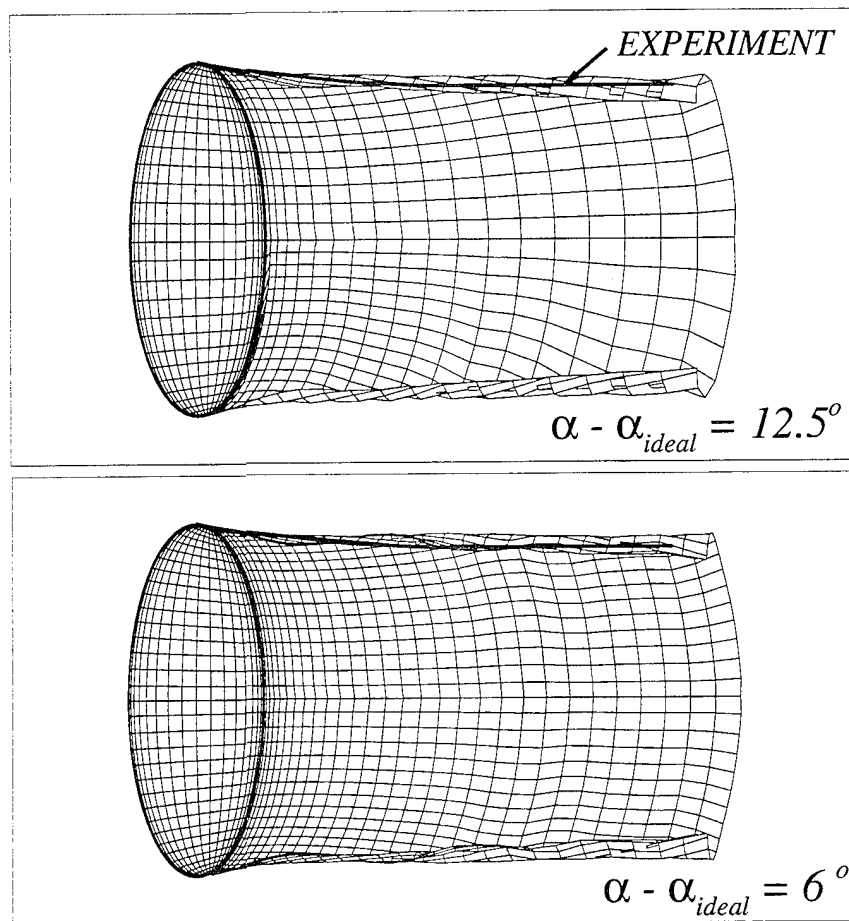

Figure 5-6: The tip vortex trajectory of an elliptic wing with 15% maximum thickness/chord ratio, $\alpha - \alpha_{ideal} = 6.0^o$ and 12.5^o; the thick line is the tip vortex trajectory from the experiment as given by Arndt(1991).

The two trajectories agree very well with each other. Arndt also showed that in his experiment, the trajectory of the tip vortex did not depend on the angle of attack. In the numerical calculation of Krasny [37] for the same wing the trajectory

was found to be dependent on the angle of attack, i.e. as the angle of attack increased, the contraction of the tip vortex increased as well.

WAKE SHAPE FOR A BACKWARD SWEPT WING
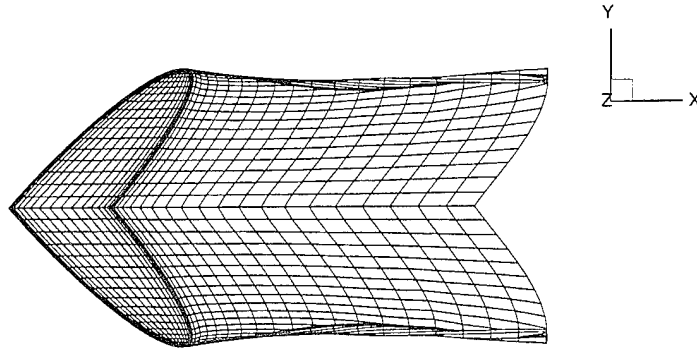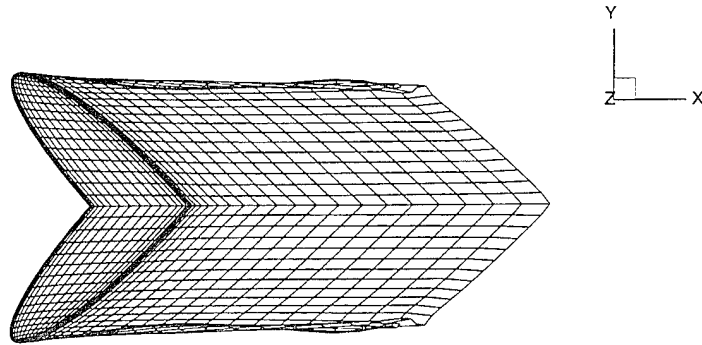

WAKE SHAPE FOR A FORWARD SWEPT WING

Figure 5-7: The geometry of the trailing wake sheet roll-up behind the swept elliptic wings; $[\tau/c]_{max} = 0.2$, $\alpha = 5.73^o$, aspect ratio AR=3. 45° backward sweep (top) 45° forward sweep (bottom).

In the present method, as the angle of attack (loading) decreases, the position of the tip moves backward along the wing trailing edge. Thus, the tip vortex trajectory remains practically the same as shown in Figure 5-6. In other words, the loading does not affect on the tip vortex trajectory as also was observed in Arndt's experiment.

5.1.3 Swept Elliptic Wings

To examine the effect of sweep on the geometry of the wake sheet roll-up, the present method is applied on two swept elliptic wings. The first wing has 45° degree forward sweet and the other wing has 45° backward sweet.
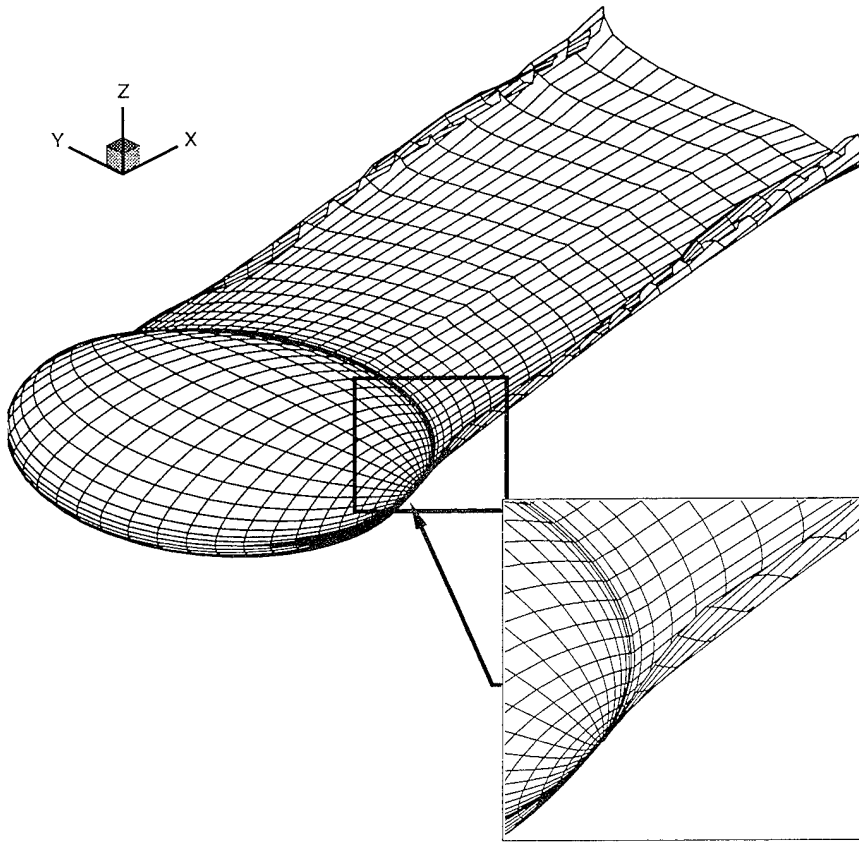

Figure 5-8: The geometry of the trailing wake sheet roll-up behind a circular wing with 20% maximum thickness/chord ratio, $\alpha = 0.1 rad$.

The results for the swept elliptic wings are shown in Figure 5-7. The aspect ratio of the wings is 3 and the angle of attack is 5.73 degrees. For both cases, the same number of panels are used as that for the non-swept elliptic wing. Since the backward

107

swept wing has usually steeper slope in circulation distribution near the tip than that for the forward swept wing as shown in Figure 2-13, the backward swept wing has a more advanced shape of the roll-up in the wake, as shown in Figure 5-7.
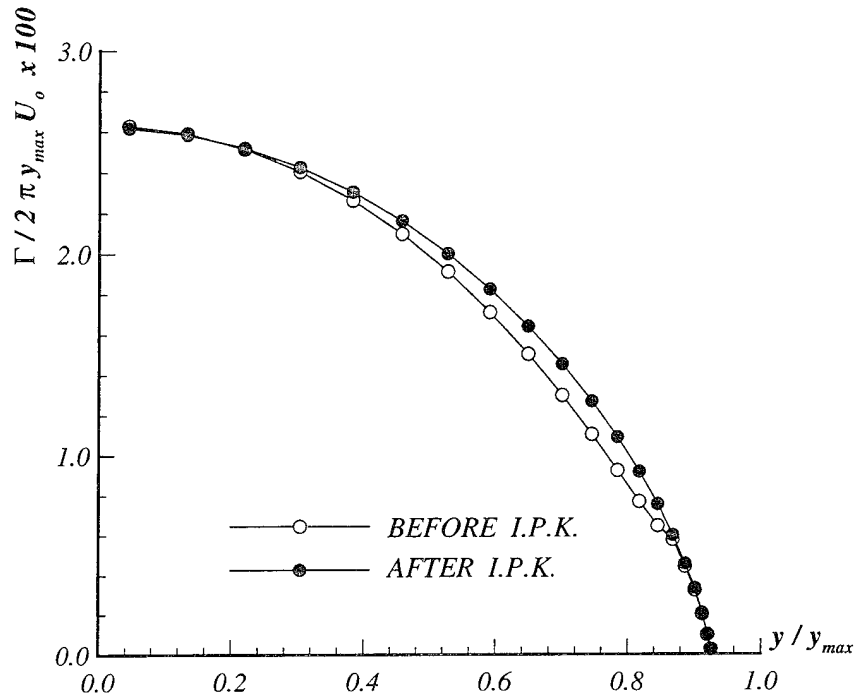

Figure 5-9: Circulation distribution on a circular wing planform hydrofoil; $[\tau/c]_{max} = 0.2, \alpha = 5.73°$. Predicted by applying the BEM on the flow adapted grid with roll-up ; before and after applying the IPK condition.

From the same figure, it can be also concluded that as the wing is swept backward, the contraction angle of the tip vortex trajectory becomes larger. This is a different trend from that shown in Figure 2-15. It appears that when the roll-up in the wake is included the final tip vortex contraction is smaller than that predicted when only the effects of thickness are included.

108

5.1.4 Circular Wing

As mentioned in Chapter 2, since a circular wing has a very large chord at the tip, it is very difficult to get a converged solution and also to predict a correct shape of the wake sheet roll-up. In particular, when an iterative Kutta condition is applied to a thick circular wing, the circulation distribution near the tip becomes non-physical, when the conventional or the blade orthogonal grid are used. In this section, the present method is applied to a circular wing with 20% maximum thickness/chord ratio. The angle of attack is 0.1 rad. The resulting shape of the rolled-up wake sheet is shown in Figure 5-8. The position of the tip moved more backward than that in the case of the elliptic wing. In the same figure, the gridlines on the wing and in the wake are shown to be smoothly connected along the trailing edge of the wing. The tip vortex also leaves the tip and rolls-up very smoothly. The circulation distribution is shown in Figure 5-9. The difference between before and after applying the IPK condition is much smaller that those from the conventional grid and the flow adapted grid without roll-up as shown in Figures 2-4 and 2-14. The flow adapted grid with roll-up has made the necessity for the iterative pressure Kutta condition less *crucial* since the results before and after IPK condition are very close to each other.

5.2   Propeller

The present method is applied to propellers in the same manner as in the case of the wings. The difference between this computation and that for the wing is that each trailing vortex is now assumed to travel in a helical trajectory rather than a straight line downstream. Also for the far field calculation, the sink disk is used instead of vortex lines, which were used in the wing problem. The far field calculation starts at $x = 1.5R$, which is usually used in the propeller application [16].

Consider a propeller subject to a spatially uniform flow $V_A(r)$ as shown in Figure 5-10. The flow around the propeller will be analyzed with respect to the propeller fixed coordinate system (x, y, z). If the propeller rotates with angular velocity ω,

then the inflow U_{in} at the x, relative the propeller is given as

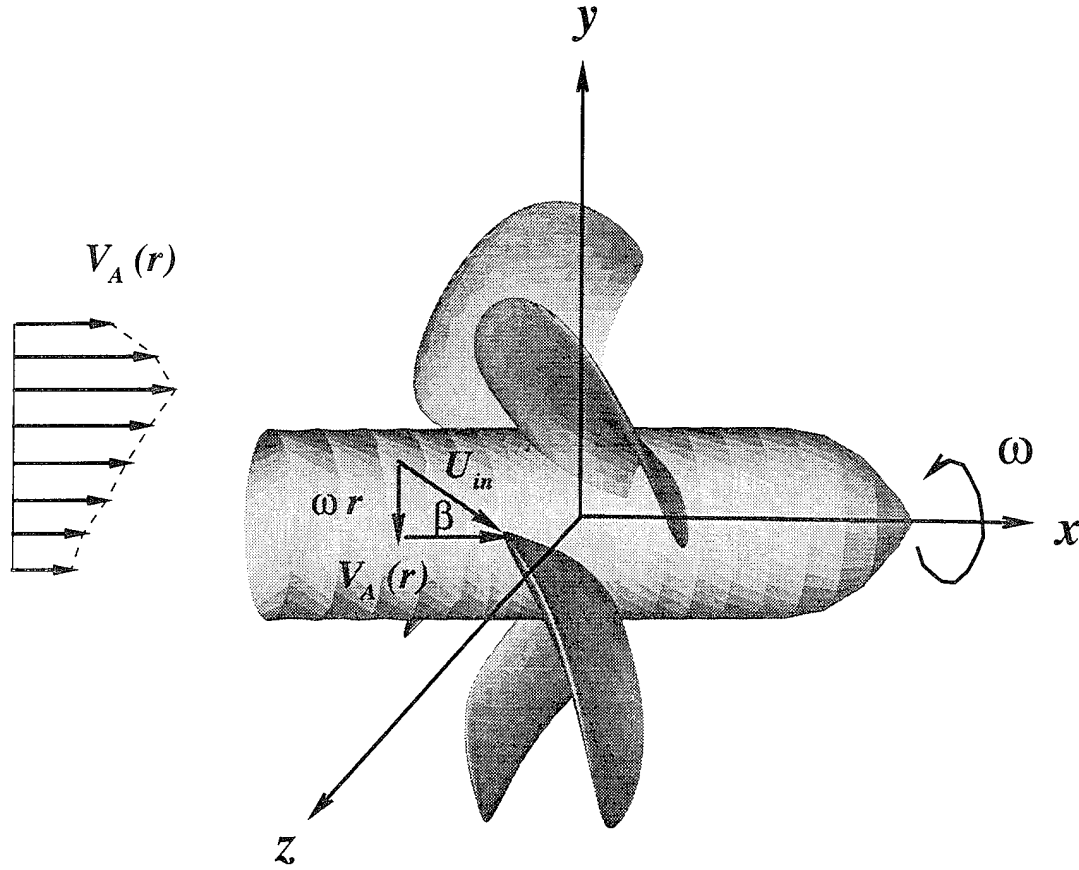$$U_{in}(x) = V_A(r)i - \omega \times x$$

Figure 5-10: Flow velocity diagram.

For all the computations described in this section, the values of the ultimate wake radius and the tip vortex contraction angle are computed by the method, rather than being given from experimental information.

Following the numerical procedure described earlier, the flow adapted grid with the wake sheet roll-up, is applied to three different kinds of DTMB propellers. The results are compared to the experimental data.

5.2.1 Propeller 4990

The first case is propeller 4990, which is a typical modern marine propeller with a large hub and nonlinear skew distribution.
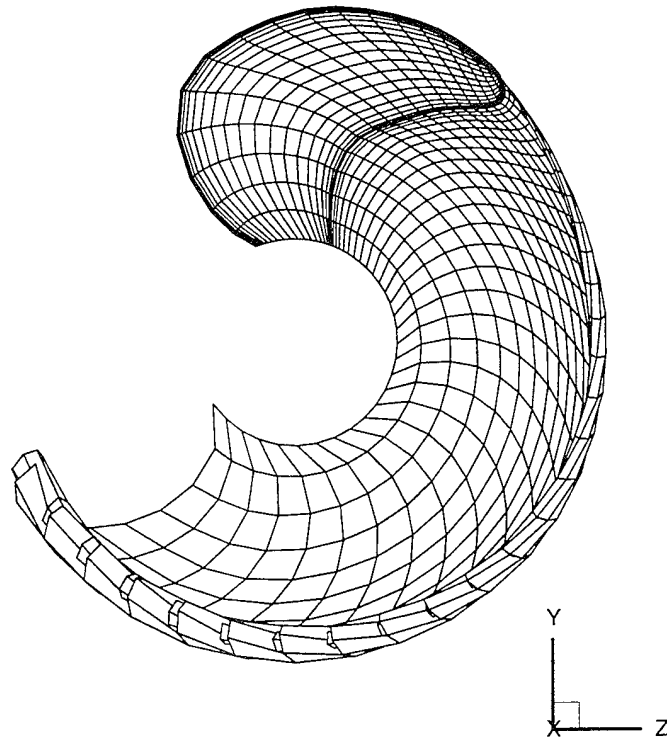

Figure 5-11: Trailing wake sheet of a propeller 4990.

In this calculation, only one blade is considered and no hub is included. The propeller 4990 has a high skew distribution and a big chord length at the tip. The calculation is performed at the design advance coefficient ($J_A = 1.270$). The number of panel on the blade is 40 and 20 in chordwise and spanwise directions, respectively. In the wake, 30 streamwise number of panels are used. The resulting shape of the wake sheet roll-up is shown in Figure 5-11. The trailing wake sheet leaves the trailing edge of the blade and smoothly rolls up downstream. In addition, the cross sections
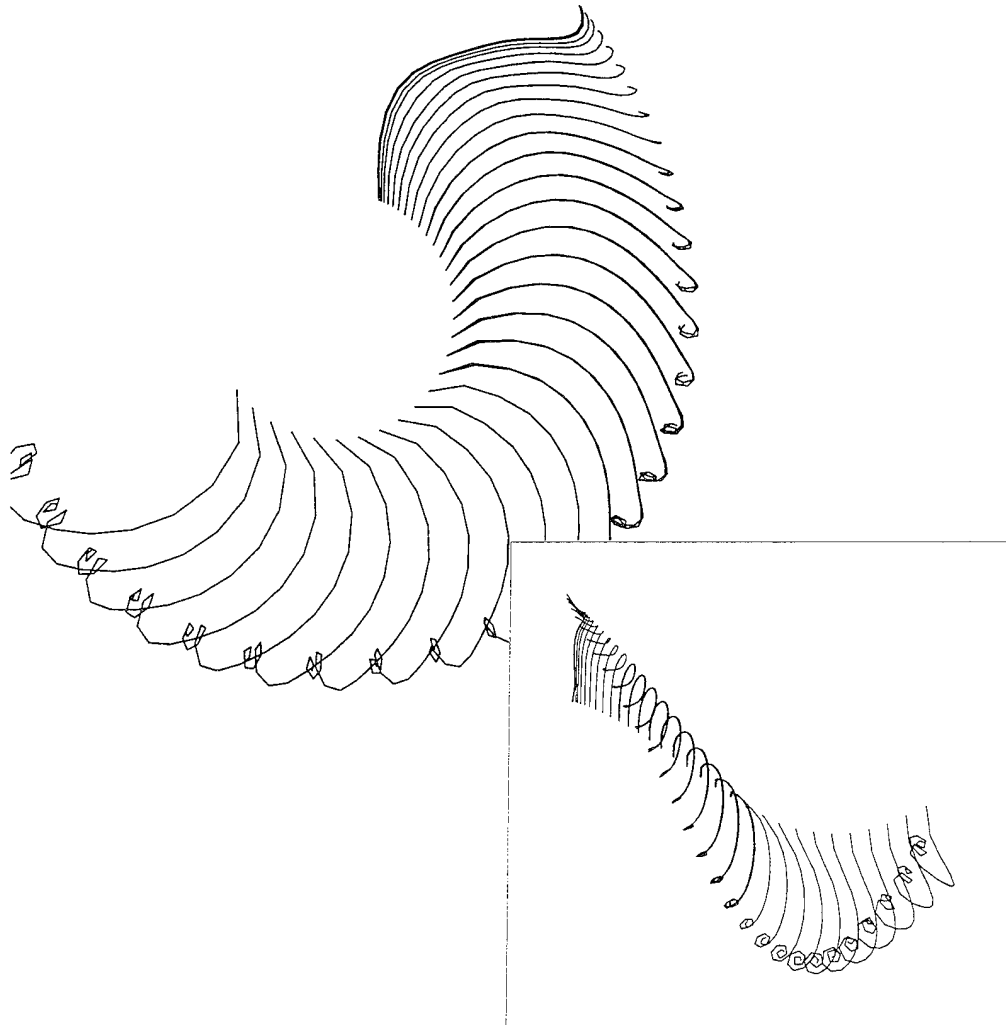
of the wake sheet are shown in Figure 5-12.

Figure 5-12: Cross section of the wake sheet of a propeller 4990.

In this figure, it is shown that the core region advances faster than the rest of the wake sheet. It seems that the axial flow in the core becomes accelerated. This is explained in Appendix B.1.1.

5.2.2 Propeller 4119

The propeller 4119 is a typical three bladed propeller. The blade has a big chord length at the tip and no skew distribution. The blade section has an NACA 66

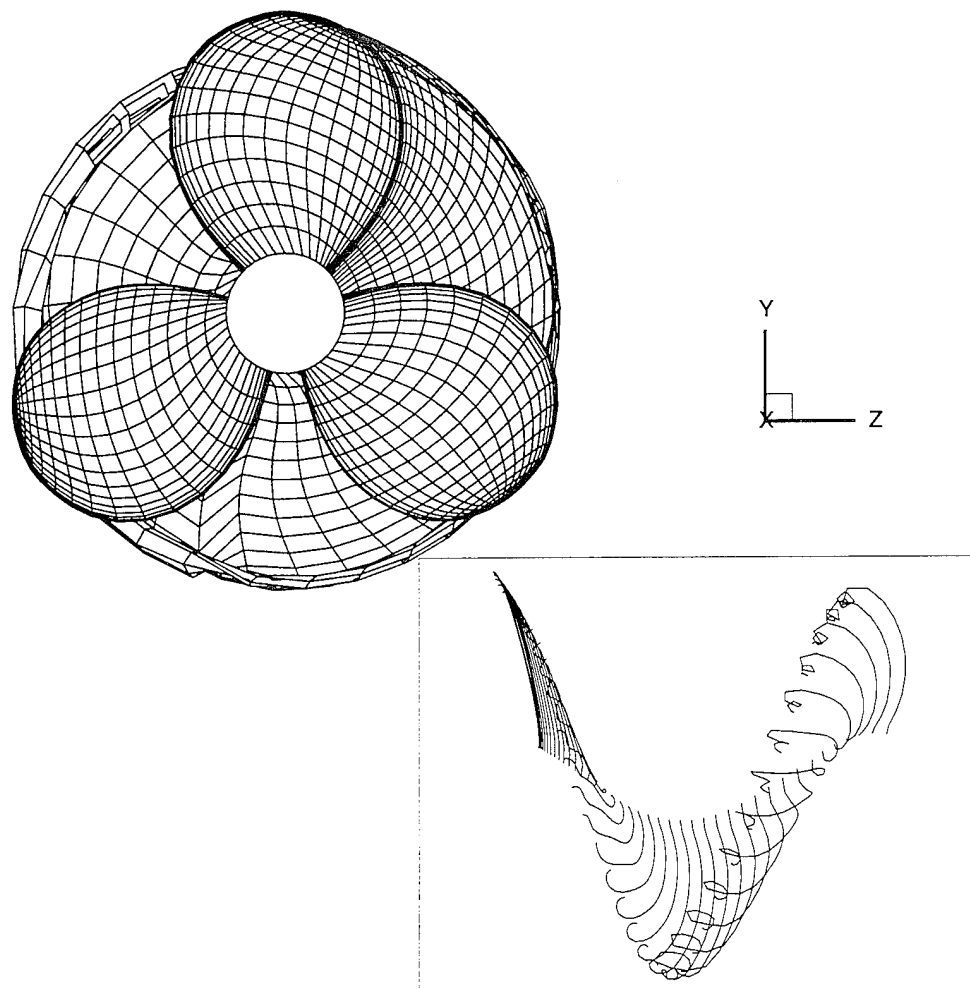modified thickness form superimposed on an a=0.8 mean camber line.

Figure 5-13: The shape of the wake sheet of a propeller 4119.

The calculation is performed at design advance coefficient equal to 0.833. The hub is not included in this calculation. Figure 5-13 shows a general shape of wake sheet roll-up and also the cross sections. This case also shows good convergence and geometry of the wake sheet roll-up. In the cross section, unlike the propeller 4990, the core region is decelerated. This is also explained in Appendix B.1.1. For this propeller, experimental results are available in [27]. Figure 5-14 shows the trajectory of the tip vortex along the x-direction for the propeller 4990. The tip vortex trajectory from

the present method gives an identical trajectory to that measured in the experiment. In addition, the pitch of the tip vortex is predicted very well, as shown in Figure 5-15.
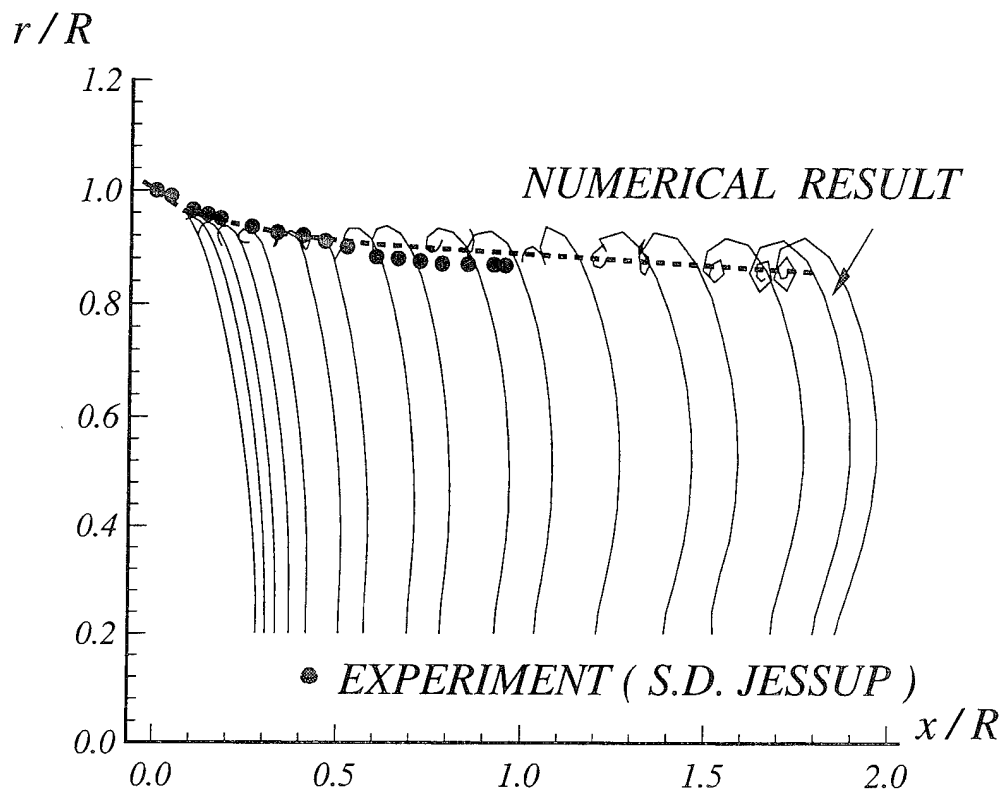
Figure 5-14: Radial location of the tip vortex for a propeller 4119.

To compare the circulation deformations behind the propeller blades, two axial locations are chosen, which are at $x/R = 0.328$ and 0.951. Figure 5-16 shows these two locations and the circulations from the present method and the experiment. The present method gives multivalues of circulation distribution near the tip. That is because the circulation is calculated along the roll-up sheet. In the rolled-up region, the radial position of the sheet goes up and down as many times as the number of turns of the roll-up. On the other hand, for the experiment, the circulation is calculated from the distribution of mean tangential velocity along the cut in the wake. This method is described by Kerwin [32] and later Wang [73] and provides

a simple comparison between the measured and the calculated circulation. From Kerwin [32],

$$\frac{\Gamma}{2\pi RV} = \frac{1}{K} \cdot \frac{r}{R} \cdot \frac{V_t}{V}$$

where V is a incoming flow and K is the number of blades and V_t is the measured mean tangential velocity.
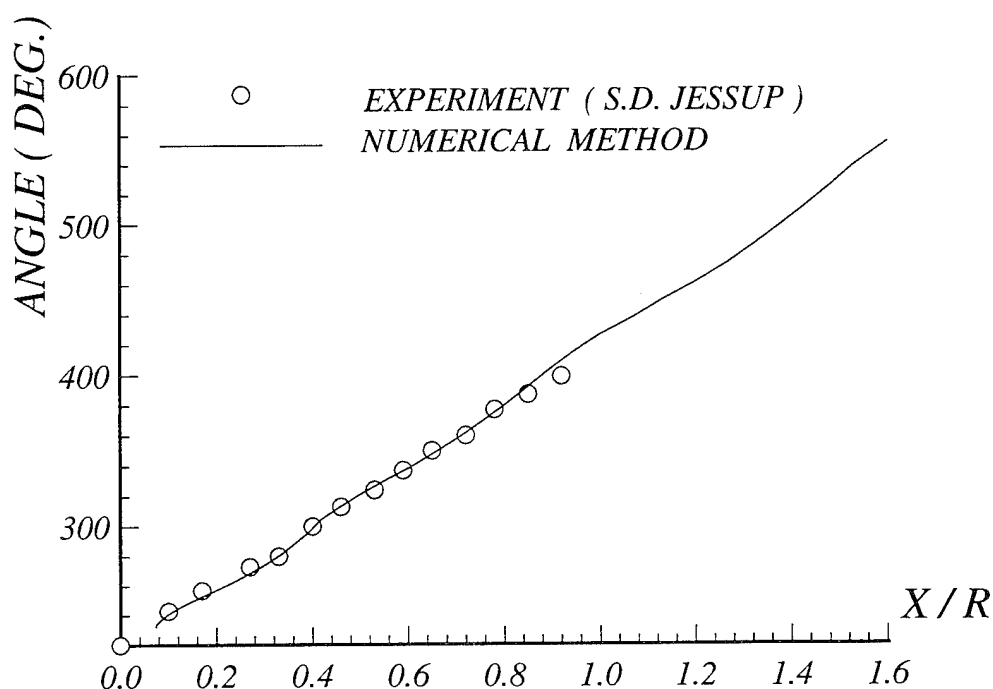

Figure 5-15: Angular position of the tip vortex for a propeller 4119.

The circulations from the experiment and the calculation at two axial locations agree well with each other.

5.2.3 Propeller 4660

Finally, in order to examine the hub effect on the wake sheet roll-up, a propeller 4660 is calculated. The propeller 4660 has five blades and high skew distribution.
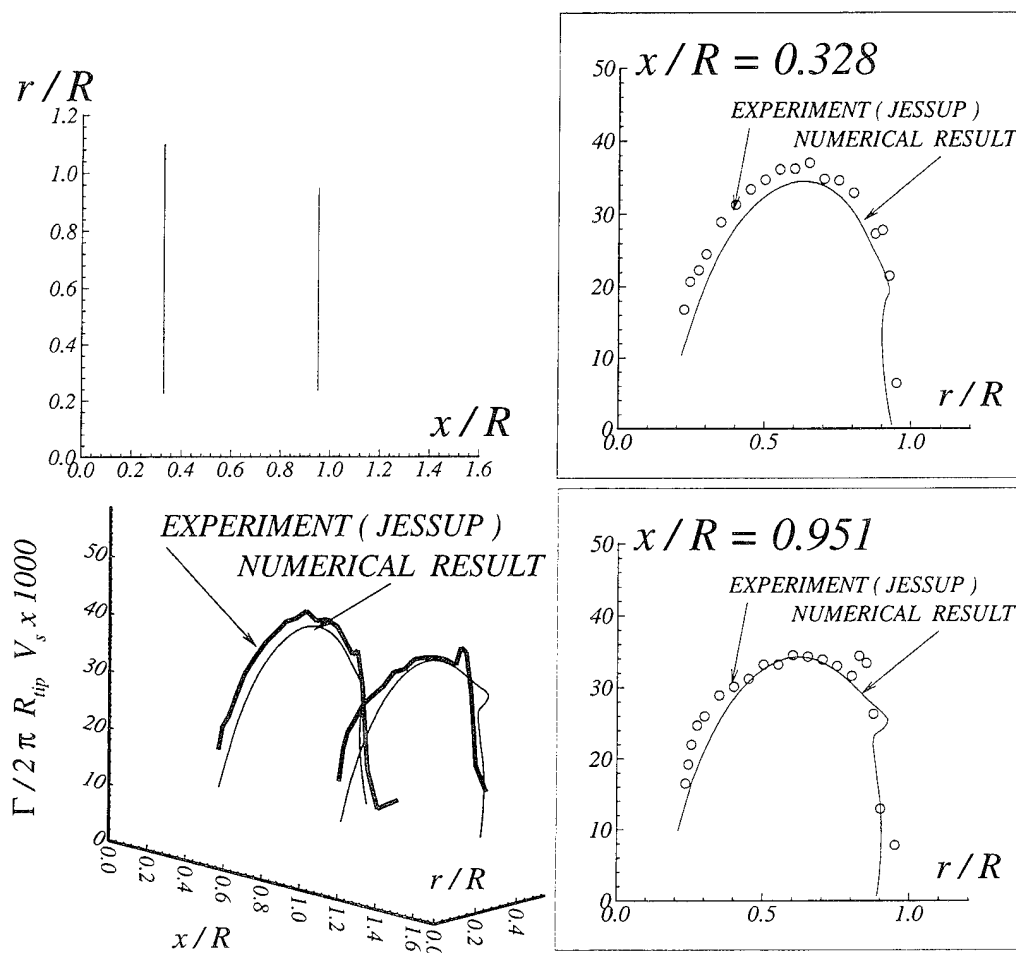

Figure 5-16: Circulation deformation in the trailing wake for a propeller 4119; At x/R = 0.328 and 0.951 .

The geometry of this propeller is given in Table 5.1. The calculation is performed at J=0.976, which is smaller than the design advance coefficient. In the computation, the hub is modeled with a fairwater downstream and constant radius upstream as

shown in Figure 5-17. In addition, the ultimate hub vortex radius is assumed as $0.1R$. Figure 5-17 shows the predicted general shape of the wake sheet roll-up. The flow leaves the tip of the blade and starts to roll up smoothly. Near the hub, the flow follows the hub surface and leaves at the ultimate hub radius.

Number of Blades   : 5
Hub/Diameter Ratio   : 0.3
Section Meanline   : NACA a=0.8
Section Thickness Form   : NACA66 (Modified)
Design Advanced Coefficient : 1.038

r/R	P/D	x_m/D	$\theta(degree)$	c/D	f/c	t/D
0.30	1.165	0.0091	2.985	0.178	0.0000	0.0420
0.35	1.296	0.0103	3.481	0.210	0.0050	0.0372
0.45	1.480	0.0103	4.810	0.271	0.0209	0.0290
0.55	1.566	0.0103	6.631	0.327	0.0267	0.0226
0.65	1.566	0.0103	8.978	0.374	0.0256	0.0178
0.75	1.498	0.0103	11.895	0.406	0.0209	0.0146
0.85	1.381	0.0103	15.410	0.409	0.0151	0.0122
0.90	1.306	0.0102	17.403	0.387	0.0122	0.0110
0.95	1.222	0.0103	19.557	0.326	0.0094	0.0091
1.00	1.128	0.0102	21.876	0.000	0.0000	0.0000

Table 5.1: The geometry of the propeller 4660.

From the figure, it is clearly shown behind the propeller blades that as the wake goes downstream, the tip vortex position is contracted. For this propeller experimental results are available in [73]. To examine the change of the circulation behind the propeller blades, three axial locations are chosen, which are at $x/R = 0.281, 0.853$ and 1.253. Figure 5-18 shows these three locations and the circulations from the present method and the experiment. The agreement between the computed and the measured circulation distributions behind the propeller blades is remarkable. From these applications, it could be concluded that the present method predicts the geometry of the wake sheet, especially the tip vortex trajectory, very smoothly and accurately. In addition, the computed circulations behind the propeller blades match well with
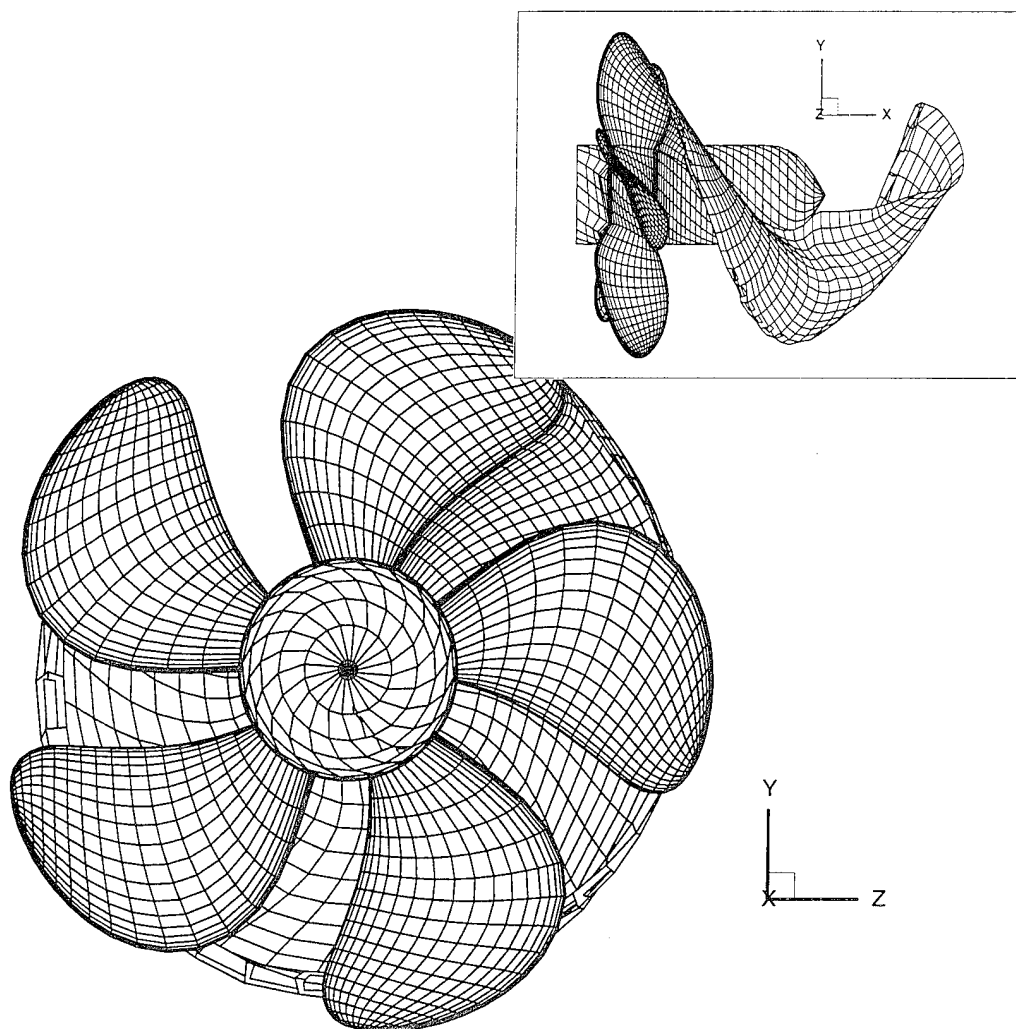
117

those from the experiment.

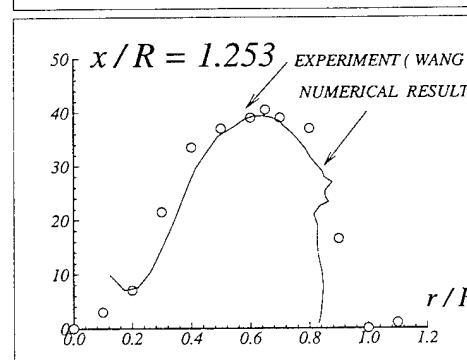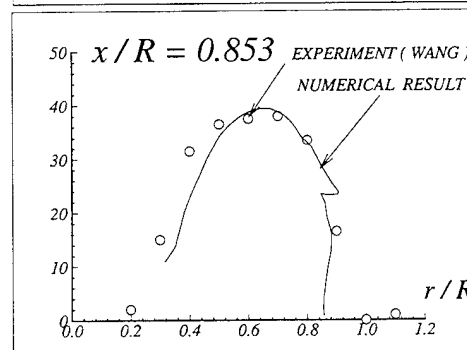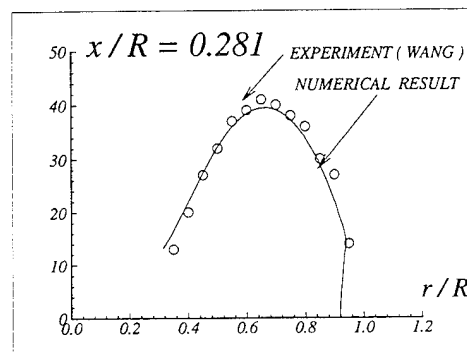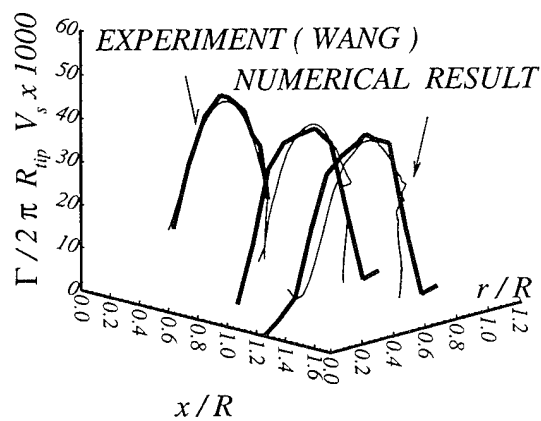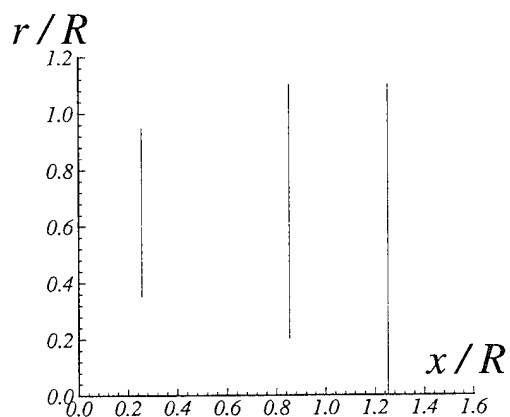Figure 5-17: The shape of the wake sheet on propeller 4660.

Figure 5-18: Circulation deformation in the trailing wake for a propeller 4660; At x/R = 0.281, 0.853 and 1.253 .

Chapter 6

Conclusions and

Recommendations

In this chapter, the accomplished improvements of the propeller steady flow panel method will be summarized and then future research topics related to the present method will be suggested.

6.1 Conclusions

In this thesis, a new grid arrangement, called by "FLow Adapted Grid", has been developed. The flow adapted grid has been implemented in a panel method and applied to a highly skewed propeller and a propeller with a large chord at the tip, which have had problems in satisfying the iterative pressure Kutta condition. The results from applying the flow adapted grid are convergent and also consistent to the results from the lifting surface method [16]. In particular, the 3% discrepancy in circulations between the panel method and the lifting surface method for propeller 4118 with zero thickness, which was found by Hsin [24], is decreased to less than 1%. In the case of wide tip blades with no skew the flow adapted grid was found to improve the predicted pressures at the tip substantially and at same time to affect the circulation distribution appreciably. For wide tip blades with high skew, the proposed grid improved the predicted pressures at the tip, even though it did not

affect the predicted circulation distribution. In order to validate the flow adapted grid, the force coefficients from using the flow adapted grid are compared to those from existing experimental data. The resulting forces and tip vortex trajectories from using FLAG are found to be closer to the experimental values than those from using the conventional grid. In the flow adapted grid the position of the tip, "the computational tip", is determined by searching among the streamlines for the one which starts at the largest blade radial location and does not intersect the propeller blade. The location of a computational tip depends on the loading (angle of attack).

A robust and efficient three-dimensional numerical method has been developed for accurately predicting the geometry of the wake sheet roll-up behind wings and propellers. A hyperboloidal panel is used in order to improve the accuracy in the highly roll-up region, where the curvature increases. By employing the hyperboloidal panel, the gap between the panels disappears and the surface of the trailing wake sheet can be modeled more accurately. In addition, in order to avoid discontinuities in the dipole strength in the wake, bi-quadratic strength dipoles are used. The panel method can predict the shape of the wake sheet smoothly. For the more advanced shape of the wake, a rediscretization scheme is applied at each iteration. In the first iteration, the vortex sheet moves from row to row in a stripwise sense. From the second and higher iteration, the vortex sheet moves altogether. The results of the high-order panel method are convergent and predict a smooth and reliable geometry of the wake sheet roll-up. The results of the method are also validated to those from other numerical methods.

Finally, the effect of the three-dimensional vortex sheet roll-up is included in the flow adapted grid. This method uses an iterative scheme to satisfy the boundary condition in the wake, where the pressure jump is forced to be equal to zero. For each iteration, the geometry of the wake sheet roll-up is obtained with a given circulation distribution, which is then updated by the panel method applied on the blade with the rolled-up wake sheet. The results of this scheme show good convergence with number of panels. In addition it has been found that when the FLAG and the completely rolled-up wake geometry are combined the results before and after IPK condition

become very close to each other. The method is applied to many wing and propeller geometries and the results are shown to agree with the existing experimental data.
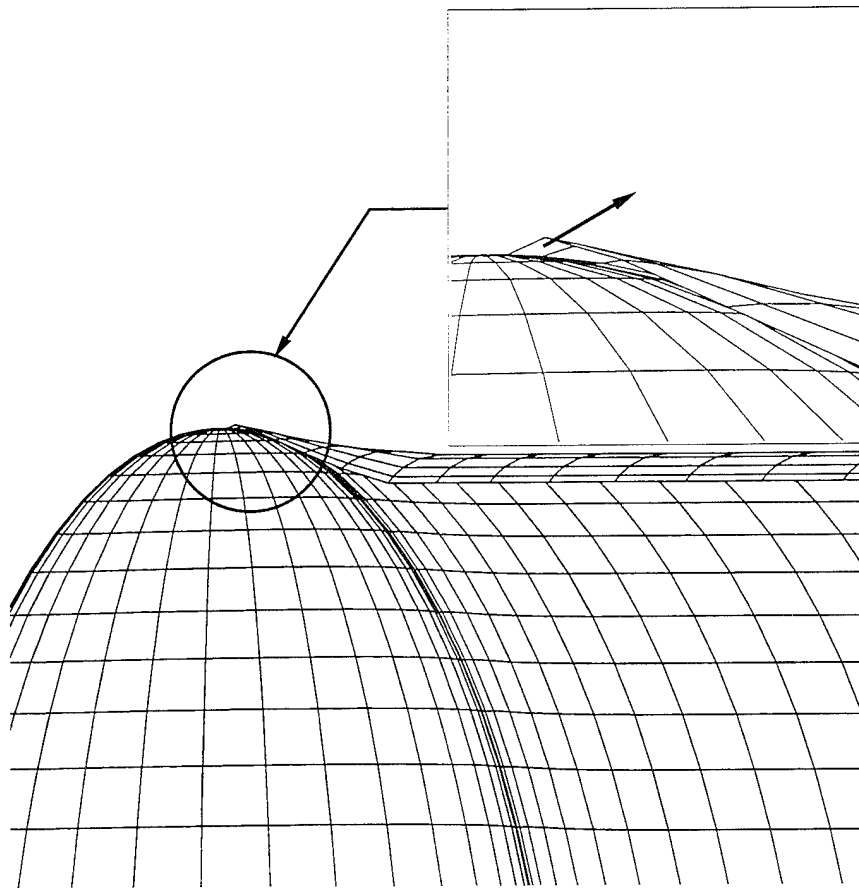

Figure 6-1: Incorrect location of the tip.

6.2 Recommendations for Future Research

The following improvements on both the physical modeling and the numerical scheme of the present method can be made.

- When a tip is assumed to be at the highest radial position, the wake sheet will not be contracted but instead, it will diverge as shown in Figure 6-1. From this examination, the position of the tip vortex detachment point, "the computational tip", may be determined numerically as shown in Figure 6-2.
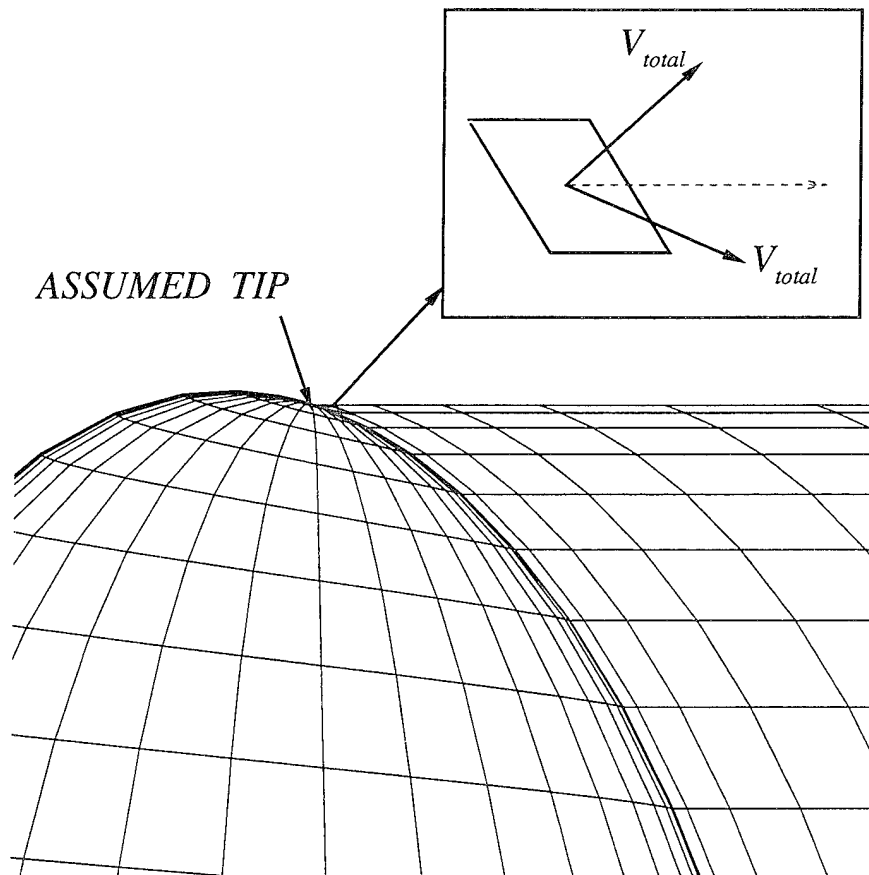

Figure 6-2: The tip vortex detachment point.

Assuming a position of the tip, the total velocity (V_{total}) is computed at a control point of the panel in the wake, which is just next to the assumed tip. If the radial component of the total velocity points outwards then move the tip downstream along the trailing edge of the blade until the rolled-up wake at the

tip leaves the blade smoothly. This scheme will work well but the panel method will have to be solved for each assumed tip. This will increase the CPU-times appreciably.
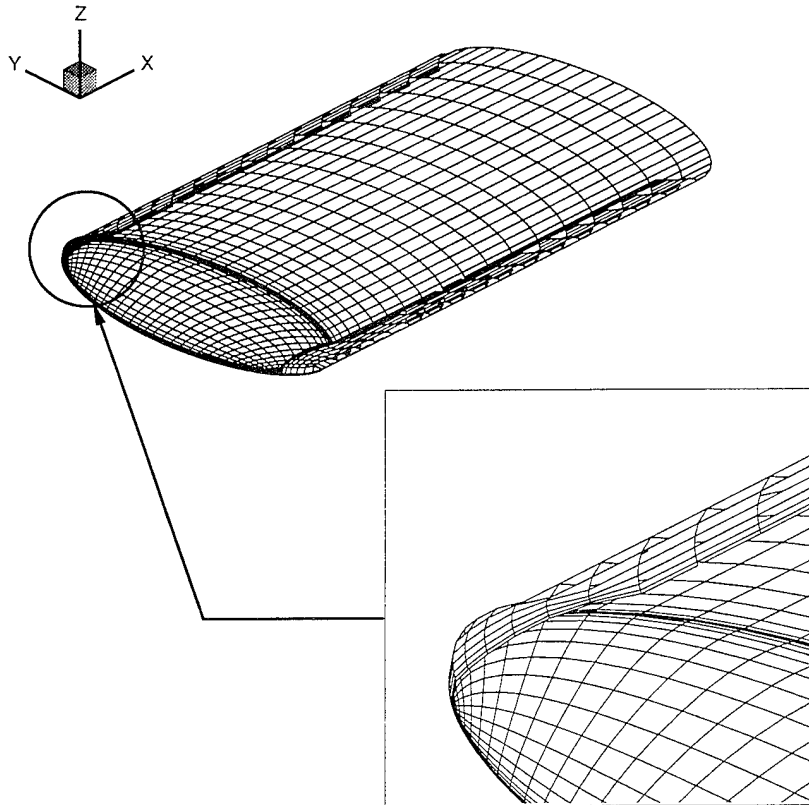

Figure 6-3: Initial paneling for the leading edge separation for an elliptic wing.

- The leading edge separation may be included by moving the tip forward along the leading edge of the propeller blade. The initial panel arrangement is shown in Figure 6-2. Applying IPK condition at the trailing edge and the part of leading edge downstream of the detachment point, the circulation distribution can be computed. With this circulation, the geometry of the trailing wake sheet

and the wake sheet separated from the leading edge may be computed.

Other improvements which are recommended for further research are :

- The modeling of a viscous core and the calculation of the boundary layer thickness at the tip.

- The prediction of the leading edge separation start point.

- The modeling of tip vortex cavitation.

Appendix A

A Numerical Kutta Condition

The circulation around the body, which is equal to the potential jump in the wake, is determined by applying the Kutta condition at the trailing edge. The Kutta condition requires that the velocity at the trailing edge be finite. In the numerical calculation, the first approximate Kutta condition, which is called Morino's condition [59], requires that the strength of the dipole in the wake be equal to the difference in the value of the dipole strengths of the two panels at the trailing edge. However, this condition does not include the free stream (cross flow), which is in the direction of a line connecting the control points of the two panels at the trailing edge. An iterative pressure Kutta condition (IPK condition) is thus introduced with the free stream correction [42], [24]. The strength of the dipole in the wake is adjusted until the pressure on the upper and lower panels become equal at the the trailing edge. However, some problems were found when this condition was applied to analyze a high skewed propeller or a propeller with a large tip chord [24]. In this appendix, these problems will be discussed and improvements to the numerical Kutta condition will be presented. These issues were first addressed by Kinnas et al. [36] but will be repeated in this Appendix for the sake of completeness.

The upper and lower panels at the trailing edge are considered. The total velocity vectors on both sides of the trailing edge are given as V^+ and V^- at the suction and pressure sides of the trailing edge, respectively, as shown in Figure A-1. The direction of the vorticity vector γ in the wake is also shown in the same figure. The

two velocity vectors have equal magnitudes as a result of the IPK condition[1]:

$$\left| V^+ \right| = \left| V^- \right| \tag{A.1}$$

On the other hand, the direction of the mean velocity vector, $V_m = [V^+ + V^-]/2$, is very different from that of the wake vorticity vector γ.
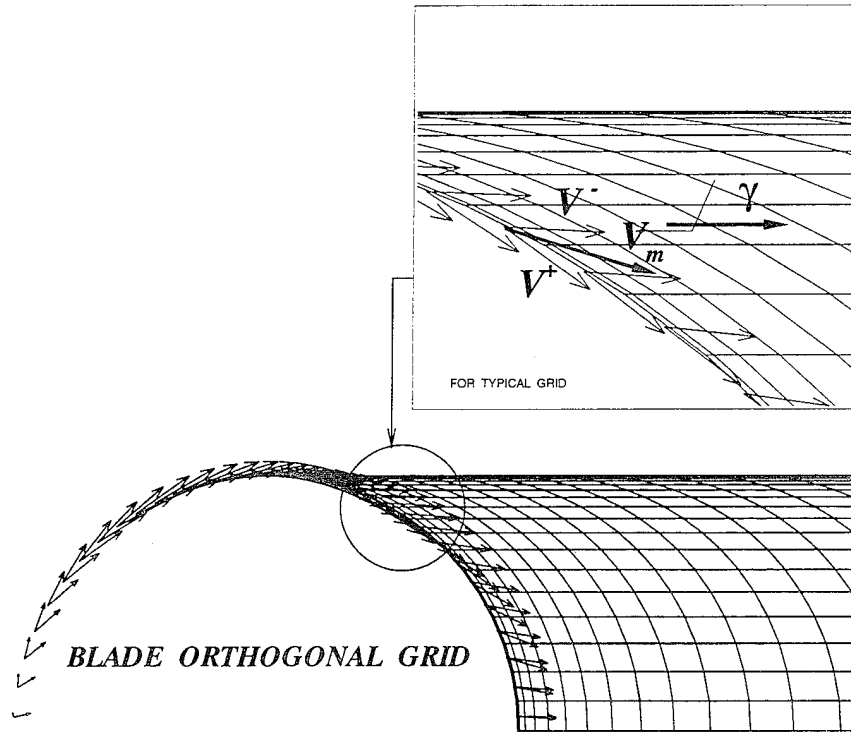

Figure A-1: Velocity vectors on the suction and pressure sides at the trailing edge of a circular planform wing; $[\tau/c]_{max} = 0.2, \alpha = 0.1 rad$. After an IPK condition.

This will result in a pressure jump in the wake given by:

$$\Delta p_W = \rho \left| V_m \times \gamma \right| \tag{A.2}$$

---

[1] The IPK condition was found to affect the magnitude of the trailing edge velocities more than their directions

127

where ρ is the flow density.

In other words, even though the IPK condition has ensured the equality of pressures at the trailing edge on the blade, it has no way to force the zero pressure jump condition in the wake. Instead, we have to align the vorticity vector, i.e. wake geometry, with the mean velocity vector at the trailing edge. It would also seem natural for the grid on the blade to be aligned with the mean velocity vector at the trailing edge. This can be explained as follows.
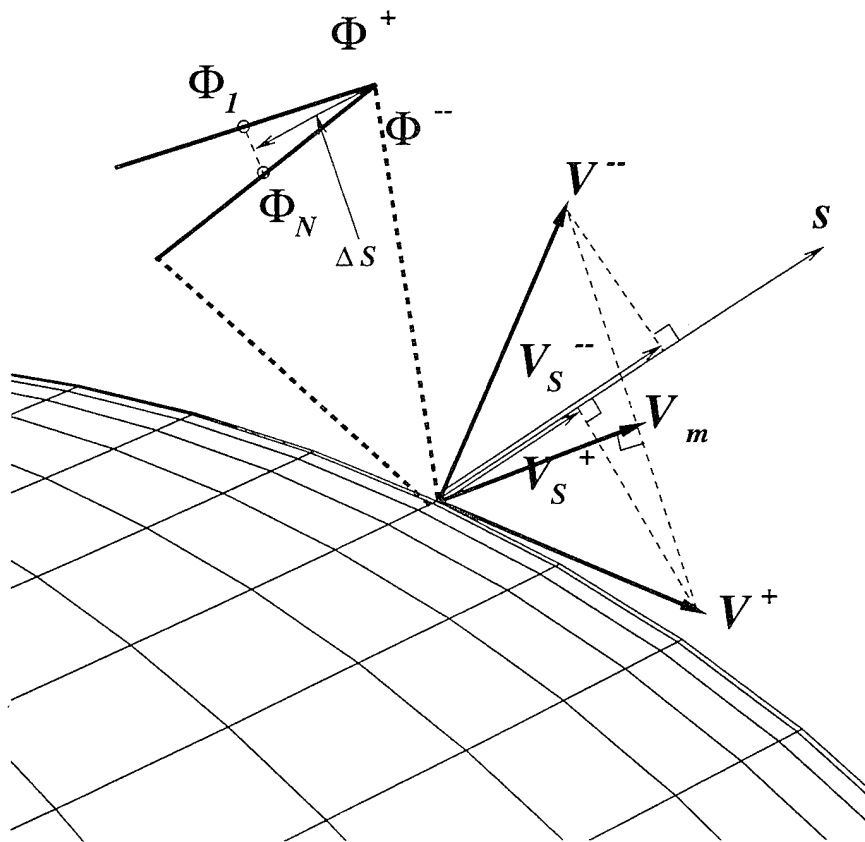

Figure A-2: Schematic of the paneling on a 3-D hydrofoil and its wake in the vicinity of the trailing edge.

The total potentials Φ^+ and Φ^- at the suction and pressure sides at the trailing edge , respectively, may be expressed as follows:

$$\Phi^+ = \Phi_1 + V_s^+ \Delta s$$
$$\Phi^- = \Phi_N + V_s^- \Delta s \tag{A.3}$$

where Φ_1 and Φ_N are the total potentials at the control points of the trailing edge panels at the suction and pressure sides, respectively; Δs is the distance of the control points from the trailing edge measured along the "chordwise" grid direction on the planform,s, as shown in Figure A-2; V_s^+ and V_s^- are the projections of the total trailing edge velocities V^+ and V^-, respectively, along s.

The Morino Kutta condition [59] at the trailing edge is:

$$\Delta \Phi = \Phi^+ - \Phi^- \tag{A.4}$$

On the other hand, the numerical implementation of equation (A.4) requires:

$$\Delta \Phi_M = \Phi_1 - \Phi_N \tag{A.5}$$

Thus, the discretization error, E, in implementing the Morino condition (i.e. before the IPK condition), may be expressed, by making use of equations (A.3), (A.4) and (A.5), as follows:

$$E = \Delta \Phi - \Delta \Phi_M = \Delta s \left[V_s^+ - V_s^- \right] \tag{A.6}$$

According to equation (A.6), in order to minimize the difference between the circulations before and after applying the IPK condition, we should have:

$$V_s^+ = V_s^- \tag{A.7}$$

In light of equation (A.1), equation (A.7) is equivalent to requiring that the mean velocity vector V_m is aligned with the grid direction s on the planform. This explains the larger difference between the circulation distributions before and after the IPK

condition, in the case of the blade orthogonal grid than in the case of the conventional grid, stated earlier. In the case of the blade orthogonal grid the angle between V_m and the s direction is larger than in the case of the conventional grid.

Appendix B

Modeling of The Roll-Up Region

This appendix is a brief summary of Lee [43] and Cummings [8] work, which explains the rationale behind modeling the roll-up region as a core, a subcore and a sheath. The nature of each region will be examined and the pressure calculation in the core will be expressed.

B.1 Definition

The clue toward a description of the roll-up region is provided by experiments [10]. In this section, these three regions, referred to as the core, the subcore and the sheath, are defined as follows :

- Core ; small changes in the tangential velocity.

- Subcore ; large changes in the tangential velocity close to the vortex axis.

- Sheath ; moderate changes in the tangential velocity surrounding the core.

These three regions are the outcome of the vortex sheet roll-up. The following summarizes each region :

B.1.1 The Core

As shown in Figure B-1, an orthogonal curvilinear coordinate system can be established in which the core axis s coincides with one of principal axes of this curvilinear system. The other coordinates (r, θ) are defined in a plane normal to the local tangent vector to s.
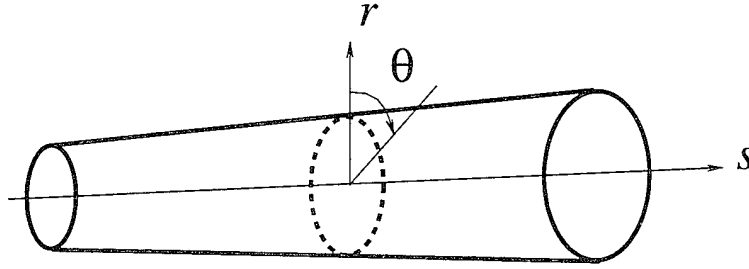

Figure B-1: The coordinate system (s, r, θ) along the core axis(s)

Then, the non-dimensionalized Navier-Stokes equation for steady incompressive laminar flow in this coordinate system are ;

$$
\begin{aligned}
v_r \frac{\partial v_r}{\partial r} &+ \frac{v_\theta}{r} \frac{\partial v_r}{\partial \theta} - \frac{v_\theta^2}{r} + v_s \frac{\partial v_r}{\partial s} = -\frac{\partial p}{\partial r} \\
&+ \frac{1}{Re} \left[\frac{\partial}{\partial r} \left(\frac{1}{r} \frac{\partial}{\partial r} (r v_r) \right) + \frac{1}{r^2} \frac{\partial^2 v_r}{\partial \theta^2} + \frac{\partial^2 v_r}{\partial s^2} - \frac{2}{r^2} \frac{\partial v_\theta}{\partial \theta} \right]
\end{aligned}
\tag{B.1}
$$

$$v_r \frac{\partial v_\theta}{\partial r} \quad + \quad \frac{v_\theta}{r}\frac{\partial v_\theta}{\partial \theta} + \frac{v_r v_\theta}{r} + v_s \frac{\partial v_\theta}{\partial s} = -\frac{1}{r}\frac{\partial p}{\partial \theta}$$
$$+ \quad \frac{1}{Re}\left[\frac{\partial}{\partial r}\left(\frac{1}{r}\frac{\partial}{\partial r}(rv_\theta)\right) + \frac{1}{r^2}\frac{\partial^2 v_\theta}{\partial \theta^2} + \frac{\partial^2 v_\theta}{\partial s^2} + \frac{2}{r^2}\frac{\partial v_r}{\partial \theta}\right] \quad \text{(B.2)}$$

$$v_r \frac{\partial v_s}{\partial r} \quad + \quad \frac{v_\theta}{r}\frac{\partial v_s}{\partial \theta} + v_s \frac{\partial v_s}{\partial s} = -\frac{\partial p}{\partial s}$$
$$+ \quad \frac{1}{Re}\left[\frac{1}{r}\frac{\partial}{\partial r}\left(r\frac{\partial v_s}{\partial r}\right) + \frac{1}{r^2}\frac{\partial^2 v_s}{\partial \theta^2} + \frac{\partial^2 v_s}{\partial s^2}\right] \quad \text{(B.3)}$$

The core is defined as the region with a relatively flat tangential velocity profile. From this definition, gradients in the tangential velocity are small. Also a Reynolds number can be assumed to be large. Therefore, at equation (B.2), the nondimensional laminar viscous term $\frac{1}{Re}\frac{\partial}{\partial r}\left(\frac{1}{r}\frac{\partial}{\partial r}(rv_\theta)\right)$ becomes much smaller that the convective terms. In addition, measurements from Schmucker and Gersten [70] indicate that in the core region the mean square quantities of the turbulent fluctuations are estimated as about 3%. It can be concluded that both laminar and turbulent shear stresses are small in the core, so that the core can be regarded as inviscid.

Inside the core, the axial velocity is usually accelerated [38], [44]. A simple explanation of this is follows. In Figure B-2, at two axial stations, A and B, the pressures on the same streamline, have the same value if the flow field in the core is assumed conical.

$$P_{2A} = P_{2B}$$

,where the first subscript refers to the position on the same streamline, and the second indicates the axial station. The radial momentum equation is

$$-\frac{\partial p}{\partial r} = \rho(\boldsymbol{v}\cdot\nabla\boldsymbol{v})_r$$
$$-\frac{1}{\rho}\frac{\partial p}{\partial r} = v_r\left(\frac{\partial v_r}{\partial r}\right) + v_r\frac{1}{r}\frac{\partial v_r}{\partial \theta} - \frac{v_\theta^2}{r} + v_z\left(\frac{\partial v_r}{\partial z}\right) \quad \text{(B.4)}$$

133

Assuming a slender vortex core, the radial momentum equation (B.4) reduces to

$$\frac{\partial p}{\partial r} = \rho \frac{v_\theta^2}{r} \geq 0$$

Thus

$$P_{2A} > P_{1A}$$

is obtained. This implies that there exists a favorable axial pressure gradient, which accelerates the flow in the core.
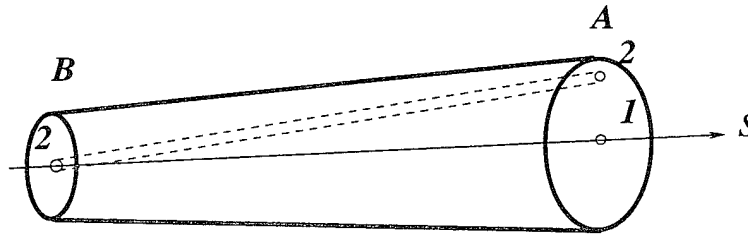

Figure B-2: Axial flow in the Core

This happens only if the conical approximation and the slender core assumption are valid. For the propeller 4990, the flow near the tip can be assumed as a conical flow because the propeller blade has high skew distribution and large tip chord. In addition the trailing wake sheet is not much rolled-up as shown in Min's experiment [54], in which the contraction is decreased as the skew becomes larger. That may be

134

a reason why the flow in the core region is accelerating in the numerical results as shown in Figure 5-11. On the other hand, propeller 4119 does not have skew. The flow near the tip is similar to that around the circular wing. In this case, the conical flow approximation is not valid anymore. Also since the trailing wake sheet has a bigger core size than that for the propeller 4990, the slender core assumption may not be valid. That may be one reason that in this case the flow is decelerated in the core, as shown in Figure 5-12.

B.1.2 The Subcore

The subcore is a small region, which is deep inside the core and close to the vortex axis. In this region, the tangential velocity changes rapidly. Inside the subcore, viscous effects can be no longer neglected because laminar viscous terms become large as r decreases. In this thesis, this region is ignored.
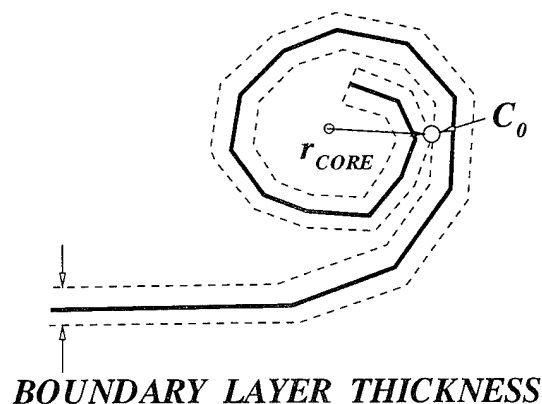
Figure B-3: Schematic diagram showing a roll-up shear layer and the cut-off location

B.1.3 The Sheath

This is the region shielding the core from the external flow. Unlike the core the sheath is a region in which both gradients in tangential velocity and viscous effects are substantial. The sheath itself is just a *remnant* of the wake sheet in the roll-up process. However, physically, this is the only medium from which irrotational flow, entering the rotational but inviscid core, can receive vorticity, thereby preserving Kelvin's theorem. In other words, if the sheath does not exist, the solutions inside the core and outside the core, cannot be matched.

B.2 The Size of the Core

This section will explain how the size of a core is determined. The center of the core coincides with the position of the trajectory of the tip vortex, which is determined by finding the centroid of the points near the core in the numerical calculation. The core boundary in a plane normal to the tip vortex trajectory is approximated as a circle. When the boundary layer thickness is added to the wake sheet at the tip, there will be a junction location at which neighboring arcs begin to touch ,C_0 in the Figure B-3. The core radius is defined as the distance between the core center and the junction point. Since the viscous calculation around the vortex core is beyond the limit of the present thesis, this will not be implemented in this thesis.

B.3 The Pressure in the Subcore

The accurate calculation of the pressure coefficient in the core is essential in the prediction of the tip vortex cavitation inception because the minimum pressure is inside the core. In this section, the calculation of the pressure inside the core will be explained.

Assume the motion is axisymmetric. The equation of motion follows.

$$u\frac{\partial u}{\partial x} + v\frac{\partial u}{\partial r} \;=\; -\frac{1}{\rho}\frac{\partial p}{\partial x} + \nu\nabla^2 u$$

136

$$u\frac{\partial v}{\partial x} + v\frac{\partial v}{\partial r} - \frac{w^2}{r} = -\frac{1}{\rho}\frac{\partial p}{\partial r} + \nu\left[\nabla^2 v - \frac{v}{r^2}\right]$$

$$u\frac{\partial w}{\partial x} + v\frac{\partial w}{\partial r} + v\frac{w}{r} = \nu\left[\nabla^2 w - \frac{w}{r^2}\right] \tag{B.5}$$

Assume axial gradients are small compared to radial gradients. Thus,

$$\frac{\partial}{\partial x} \quad << \quad \frac{\partial}{\partial r}$$

$$u \quad << \quad v$$

Then equations (B.5) become,

$$u\frac{\partial u}{\partial x} + v\frac{\partial u}{\partial r} = -\frac{1}{\rho}\frac{\partial p}{\partial x} + \nu\left[\frac{\partial^2 u}{\partial r^2} + \frac{1}{r}\frac{\partial u}{\partial r}\right] \tag{B.6}$$

$$\frac{w^2}{r} = \frac{1}{\rho}\frac{\partial p}{\partial r} \tag{B.7}$$

$$u\frac{\partial w}{\partial x} + v\frac{\partial w}{\partial r} + \frac{w}{r} = \nu\left[\nabla^2 w - \frac{w}{r^2}\right] \tag{B.8}$$

The integral form of equation (B.7) is ;

$$p = p_\infty - \rho\int_r^\infty \frac{w^2}{r}dr$$

In the region far downstream, Bachelor finds a solution for this equation of form;

$$w = \frac{\Gamma}{2\pi r}\left[1 - l^{\frac{-U_0 r^2}{4\nu x}}\right]$$

If the subcore radius is defined as the radius where the tangential velocity w is maximum, then the subcore radius a has a following form.

$$a^2 = 1.258 \cdot \frac{4\nu x}{U_0}$$

The change of subcore radius with the distance downstream is ;

$$\frac{da}{dx} = \frac{a}{2x}$$

137

From the above results, it can be concluded that the subcore radius does not change fast enough for viscosity to have any significant effect on results in the region close to the propeller blade. Therefore, the subcore can be modeled by a Rankine vortex with a group of trailing vorticies outside it, at each downstream section. The pressure in the subcore can be calculated assuming axial symmetry and a constant radius subcore.

For $r \leq a$

$$
\begin{aligned}
p(r) &= p_\infty - \rho \int_r^\infty \frac{w^2}{r} dr \\
&= \frac{\rho \Gamma_c^2}{4\pi^2 a^2} \int_r^a r\, dr - \frac{\rho \Gamma_c^2}{4\pi^2} \int_a^\infty \frac{dr}{r^3} + p_\infty \\
&= p_\infty - \frac{\rho \Gamma_c^2}{8\pi^2 a^4}(a^2 - r^2) - \frac{\rho \Gamma_c^2}{8\pi^2 a^2}
\end{aligned}
$$

Therefore, the pressure coefficient C_p is ;

$$
\begin{aligned}
C_p = \frac{p - p_\infty}{\frac{1}{2}\rho U_\infty^2} &= -\left[\frac{\Gamma_c}{2\pi r U_\infty}\right]^2 & r \geq r_0 \\
&= \left[\frac{\Gamma_0}{2\pi r_0 V_\infty}\right]^2 \left[\left(\frac{r}{r_0}\right) - 2\right] & r \leq r_0
\end{aligned}
$$

Appendix C

The Calculation of The Induced Velocity

In the calculation of the three-dimensional trailing wake sheet roll-up, a new higher order panel method is applied. This method is developed in order to handle the arbitrary strength of singularities over a curved surface. A special algorithms has been developed for the calculation of induced potential by Maniar [45]. In this appendix, the induced velocity due to a distribution of normal dipoles on a curved panel is evaluated for the case where the density of the singularities is of arbitrary polynomial form. The same algorithm as Maniar [45] will be applied for the calculation.

As shown in Figure C-1, an orthogonal coordinate system (x, y, z) is taken as a global coordinate system. Then a panel is transformed to local coordinate system (ξ, η, ζ) with $\zeta = 0$. Let S be the curved panel surface and Σ be its transformed panel surface. Q is a point on S and P is a field point. Then the induced velocity at P due to a distribution of dipoles of order M on S is given as

$$
\begin{aligned}
\boldsymbol{\nabla}\phi(P) &= \frac{1}{4\pi} \sum_{i=0}^{M} \sum_{j=0}^{M} \int \int_{\Sigma} \xi^i \eta^j \boldsymbol{\nabla} \frac{\partial}{\partial n_j} \left(\frac{1}{R}\right)_{i,j} d\Sigma \\
&= \frac{1}{4\pi} \sum_{i=0}^{M} \sum_{j=0}^{M} \int \int_{\Sigma} \xi^i \eta^j \boldsymbol{\nabla} \left(\frac{\boldsymbol{n}_j \cdot \boldsymbol{R}_{i,j}}{R_{i,j}^3}\right) d\Sigma
\end{aligned}
$$

$$= \frac{1}{4\pi} \sum_{i=0}^{M} \sum_{j=0}^{M} \nabla \phi_{i,j} \tag{C.1}$$

where n is a normal vector at the centroid of the panel and R is a position vector from a collocation point on the curved surface of order N to a field point, which is expressed by

$$R = \sum_{m=0}^{N} \sum_{n=0}^{N} x_{m,n} \xi^m \eta^n$$
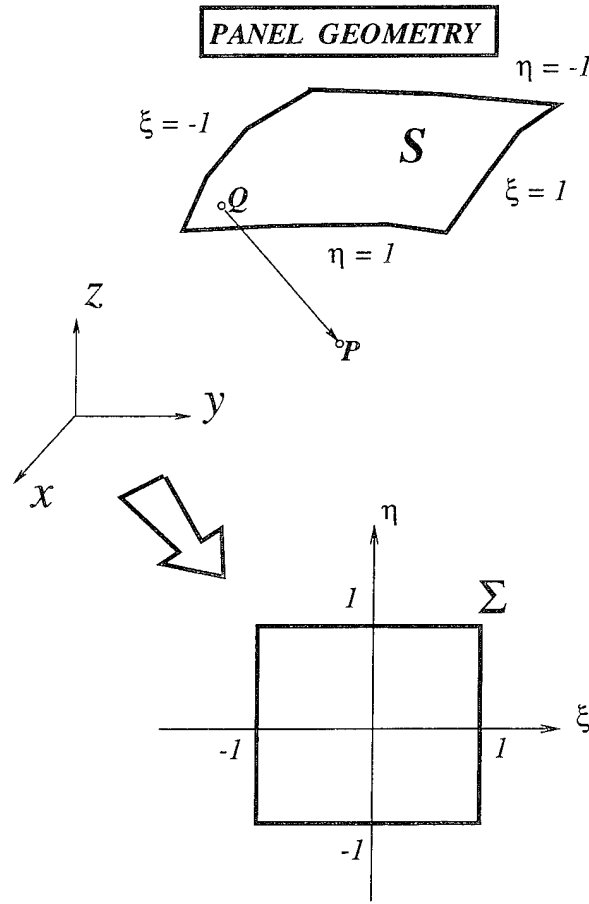
Figure C-1: The panel geometries in the global coordinate system and the transformed coordinate system.

Consider the evaluation of gradient of a weighted dipole integral in (C.1),

$$\nabla \phi_{i,j} = \int\int_{\Sigma} \xi^i \eta^j \nabla \cdot \left(\frac{\boldsymbol{n}_j \cdot \boldsymbol{R}_{i,j}}{\boldsymbol{R}_{i,j}^3} \right) d\Sigma \qquad (C.2)$$

The equation (C.2) can be rewritten in the (ξ, η, ζ) plane as,

$$\begin{aligned}
\nabla \phi_{i,j} &= \int\int_{\Sigma} \xi^i \eta^j \nabla \left(\frac{\boldsymbol{n} \cdot \boldsymbol{R}}{R^3} \right)_{i,j} d\Sigma \\
&= \int\int_{\Sigma} \xi^i \eta^j \left[\frac{\boldsymbol{n} R^2 - 3\boldsymbol{R}(\boldsymbol{n} \cdot \boldsymbol{R})}{R^5} \right]_{i,j} d\Sigma \\
&= \int_{\eta_1}^{\eta_2} \int_{\xi_1}^{\xi_2} \xi^i \eta^j \left[\frac{(\boldsymbol{x}_\xi \times \boldsymbol{x}_\eta)}{R^3} - 3\frac{\boldsymbol{R} \cdot (\boldsymbol{R} \cdot (\boldsymbol{x}_\xi \times \boldsymbol{x}_\eta))}{R^3} \right]_{i,j} d\xi d\eta \qquad (C.3)
\end{aligned}$$

This integral will be implemented in three categories, which are near field, far field and self induced coefficients. Each region is decided by the ratio between the maximum diagonal distance of the panel and the distance between the field point and the collocation point of the panel. The followings summarize the numerical formulation for each region;

- Far Field

  This is the case when the field point is far away from the panel. The ratio of the distance between the field point and the collocation point to the maximum diagonal distance is greater than 5. Usually all panels except themselves and neighboring panels are in this category. The integrals in equation (C.3) do not have a closed form solution. Therefore, the integrals have to be solved numerically. Gaussian Quadrature is used in this section.

  The discrete formulations are follows;

$$\begin{aligned}
\nabla \phi_{ij} &= \int_{-1}^{1} \int_{-1}^{1} \xi^i \eta^j \left[\frac{(\boldsymbol{x}_\xi \times \boldsymbol{x}_\eta)_{(\xi',\eta')}}{R^3} - 3\frac{\boldsymbol{R} \cdot (\boldsymbol{R} \cdot (\boldsymbol{x}_\xi \times \boldsymbol{x}_\eta)_{(\xi',\eta')})}{R^3} \right] \\
&\quad \times \left(\frac{\xi_2 - \xi_1}{2} \right) \left(\frac{\eta_2 - \eta_1}{2} \right) d\xi' d\eta' \\
&= \sum_{n_\xi=1}^{k} \sum_{n_\eta=1}^{k} \alpha_{n_\xi} \alpha_{n_\eta} \xi^i \eta^j \left[\frac{(\boldsymbol{x}_\xi \times \boldsymbol{x}_\eta)}{R^3} - 3\frac{\boldsymbol{R} \cdot (\boldsymbol{R} \cdot (\boldsymbol{x}_\xi \times \boldsymbol{x}_\eta))}{R^3} \right]
\end{aligned}$$

141

$$\times \left(\frac{\xi_2 - \xi_1}{2} \right) \left(\frac{\eta_2 - \eta_1}{2} \right) \qquad\qquad (C.4)$$

$$, \text{where} \quad \xi = \frac{\xi_2 - \xi_1}{2}\xi' + \frac{\xi_1 + \xi_2}{2}$$

$$\eta = \frac{\eta_2 - \eta_1}{2}\eta' + \frac{\eta_1 + \eta_2}{2}$$

$$\boldsymbol{R} = \boldsymbol{x}_p - \boldsymbol{x}$$

$$k \qquad \text{is the order of quadrature.}$$

$$\alpha_{n_\xi}, \alpha_{n_\eta} \qquad \text{are coefficients of the quadrature.}$$

In equation (C.4), the directed surface element $\boldsymbol{x}_\xi \times \boldsymbol{x}_\eta$ can be computed by follows.

$$\text{Let} \quad \boldsymbol{x}_\xi \times \boldsymbol{x}_\eta = \sum_{m=0}^{N_w} \sum_{n=0}^{N_w} w_{mn}\xi^m\eta^n \qquad , N_w \leq 2N - 1$$

$$\boldsymbol{x} = \sum_{m=0}^{N} \xi^m \boldsymbol{Q}_m \qquad , \boldsymbol{Q}_m = \sum_{n=0}^{N} \boldsymbol{x}_{m,n}\eta^n$$

$$\boldsymbol{x}_\xi = \sum_{m=0}^{N} m\xi^{m-1}\boldsymbol{Q}_m = \sum_{m=0}^{N-1} (m+1)\xi^m \boldsymbol{Q}_{m+1}$$

$$\boldsymbol{x}_\eta = \sum_{m=0}^{N} \xi^m (\boldsymbol{Q}_v)_m$$

$$\boldsymbol{x}_\xi \times \boldsymbol{x}_\eta = \sum_{m=0}^{2N-1} \xi^m \cdot \sum_{\mu=max(0,m-N)}^{min(m,N-1)} (\mu+1)\boldsymbol{Q}_{\mu+1} \times (\boldsymbol{Q}_v)_{m-\mu}$$

$$\boldsymbol{Q}_{\mu+1} \times (\boldsymbol{Q}_\eta)_{m-\mu} = \sum_{n=0}^{N} \boldsymbol{x}_{\mu+1,n}\eta^n \times \sum_{n=0}^{N} \boldsymbol{x}_{m-\mu,n}n\eta^{n-1}$$

$$= \sum_{n=0}^{N} \boldsymbol{x}_{\mu+1,n}\eta^n \times \sum_{n=0}^{N-1} \boldsymbol{x}_{m-\mu,n+1}(n+1)\eta^n$$

$$= \sum_{n=0}^{2N-1} \eta^n \cdot \sum_{\nu=max(0,n-N+1)}^{min(n,N)} \boldsymbol{x}_{\mu+1,nu} \times \boldsymbol{x}_{m-\mu,n-\nu+1}(n-\nu+1)$$

Therefore,

$$\boldsymbol{x}_\xi \times \boldsymbol{x}_\eta = \sum_{m=0}^{2N-1}\sum_{n=0}^{2N-1} \boldsymbol{w}_{m,n}\xi^m\eta^n$$

$$\boldsymbol{w}_{m,n} = \sum_{\mu=0}^{m}(\mu+1) \cdot \sum_{\nu=0}^{n}(n-\nu+1)(\boldsymbol{x}_{\mu+1,\nu} \times \boldsymbol{x}_{m-\mu,n-\nu+1})$$

$$\boldsymbol{w}_{n,m-n} = \sum_{\nu=0}^{m-n}(m-n-\nu+1) \times$$
$$\sum_{\mu=0}^{n}(\mu+1)(\boldsymbol{x}_{\mu+1,\nu} \times \boldsymbol{x}_{n-\mu,m-n-\nu+1}) \qquad (C.5)$$

From equations (C.4) and (C.5), the induced velocity can be computed.

- Near Field

In near field, the induced velocity is evaluated by an adaptive subdivision scheme, which will be explained below. When the field point is in the near field region, the panel is subdivided until the ratio between the distance from the field point to the collocation point and the maximum diagonal distance of the subdivided panel is out of the near field region. Then, we can use the same scheme for that for the far field. Let the number of subdivided panels along the ξ and η-direction be N_ξ, N_η respectively. Then

$$\boldsymbol{\nabla}\phi_{ij} = \sum_{n=1}^{N_\xi}\sum_{m=1}^{N_\eta} \int_{\eta_{n,m}}^{\eta_{n,m+1}} \int_{\xi_{n,m}}^{\xi_{n+1,m}} \xi^i\eta^j\boldsymbol{\nabla}\frac{\boldsymbol{R}}{R^3} \cdot (\boldsymbol{x}_\xi \times \boldsymbol{x}_\eta) \ d\xi d\eta \qquad (C.6)$$

When the panel is subdivided, N_ξ and N_η are determined from the panel aspect ratio. The Equation (C.6) can be computed by using the Gaussian quadrature as explained in case for the far field calculation.

- Self Induced Coefficient

This is the case when the field point is on the surface over which integration is

143

carried out. For the induced potential, the singularities are analytically removed and the desingularized integrands are expanded in a series with algebraic type terms which are integrable [45].

Figure C-2: An example for calculating self induced velocity.

In the case of self induced velocity, to this moment, there has been found no way to remove the singularities analytically. Instead, we divide a panel into smaller panels with the center panel having the same collocation point as the original panel. Then, find the self induced velocity by assuming that the strength of the dipole is constant on the central panel and its geometry flat. In the other panels the induced velocities are computed by using the same scheme as that for the near and the far field. In order to find an adequate number of subdivisions, an example is considered for a non-planar panel with bi-linear dipole distribution

144

as shown in Figure C-2. As shown in Table C.1, the self induced velocity has converged in 3 subdivisions. In the calculation of the wake sheet roll-up, three subdivision is used for the shorter side and for the longer side, the number of subdivisions is determined by the aspect ratio of a panel.

Number of Subdivisions	u	v	w
1	0.841592	0.841592	-1.683183
3	0.819042	0.810093	-1.642820
5	0.819042	0.810093	-1.642820

Table C.1: Convergence of the self induced velocity.

Bibliography

[1] D. Almosnino. High Angle-of-Attach Calculations of the Subsonic Vortex Flow on Slender Bodies. *AIAA Journal*, Vol 23(No 8):pp 1150–1156, 1985.

[2] R.E.A. Arndt, V.H. Arakeri, and H. Higuchi. Some Observations of Tip-Vortex Cavitation. *Journal of Fluid Mechanics*, Vol 229:pp 269–289, 1991.

[3] G.R. Baker. The 'Cloud in Cell' Technique Applied to the Roll-Up of Vortex Sheets. *Journal of Computational Physics*, Vol 31:pp 76–95, 1979.

[4] G.R. Baker. A Test of the Method of Fink and Soh for Following Vortex Sheet Motion. *Journal of Fluid Mechanics*, Vol 100(No 1):pp 209–220, 1980.

[5] G. K. Batchelor. *An Introduction to Fluid Dynamics*. Cambridge University Press, 1967.

[6] G. Birkhoff. Helmholtz and Taylor Instability. In *Proc. Symp. on Appl. Math. Am. Math. Soc.*, volume 13, pages 55–76, 1962.

[7] A.J. Chorin and P.S. Bernard. Discretization of a Vortex Sheet, with an Example of Roll-Up. *Journal of Computational Physics*, Vol 13:pp 423–429, 1973.

[8] D.E. Cummings. *Vortex Interactions In a Propeller Wake*. PhD thesis, Department of Ocean Engineering, MIT, June, 1968.

[9] P. Dupont and P. Cerrutti. Comparison between Tip Vortex Development Calculations and Measurements on an Elliptic Planform. *Third European FIDAP Users Group Meeting*, September 1991.

[10] P.B. Earnshaw. An Experimental Investigation of the Structure of a Leading-Edge Vortex. *Aeronautical Research Council, R & M*, (No 3281), March 1961.

[11] L. Eça, J. Falcão de Campos, and M. Hoekstra. Prediction of Incompressible Tip Vortex Flow. In *Proceedings of Twentieth Symposium on Naval Hydrodynamics*, Santa Barbara, California, August 1994.

[12] O.M. Faltinsen and B. Pittersen. Vortex Shedding Around Two Dimensional Bodies at High Reynolds Number. In *Proceedings of Fourteenth Symposium on Naval Hydrodynamics*, University of Michigan, Ann Arbor, August 1982.

[13] P.T. Fink and W.K. Soh. Calculation of Vortex Sheets in Unsteady Flow and Applications in Ship Hydrodynamics. In *Proceedings of Tenth Symposium on Naval Hydrodynamics*, pages 463–488, Massachusetts Institute of Technology, 1978.

[14] P.T. Fink and W.K. Soh. A New Approach to Roll-Up Calculations of Vortex Sheets. In *Proceedings of the Royal Society of London,Series A*, volume 362, pages 195–209, 1978.

[15] D. Fruman, C. Dugué, A. Pauchet, P. Cerruti, and L. Briançon-Marjolet. Tip Vortex Roll-Up and Cavitation. In *Proceedings of Nineteenth Symposium on Naval Hydrodynamics*, Seoul ,Korea, August 1992.

[16] D.S. Greeley and J.E. Kerwin. Numerical Methods for Propeller Design and Analysis in Steady Flow. *Trans. SNAME*, Vol 90, 1982.

[17] N.D. Ham. Aerodynamic Loading on a Two-Dimensional Airfoil During Dynamic Stall. *AIAA Journal*, Vol 6(No 10):pp 1927–1934, 1968.

[18] F.R. Hama. Progressive Deformation of a Perturbed Line Vortex Filament. *Phys. Fluids*, Vol 6:pp 526–534, 1963.

[19] J.L. Hess and A.M.O. Smith. Calculation of Nonlifting Potential Flow About Arbitrary Three Dimensional Bodies. *Journal of Ship Research*, Vol 8(No 2), September 1964.

[20] J.L. Hess and W.O. Valarezo. Calculation of Steady Flow About Propellers by Means of a Surface Panel Method. In *23rd Aerospace Sciences Meeting*, Reno, Nevada, January 1985. AIAA.

[21] H.W.M. Hoeijmakers. Methods for Numerical Simulation of Leading Edge Vortex Flow. In *Studies of Voretx Dominated Flows*, pages 223–269. Springer Verlag, 1985.

[22] H.W.M. Hoeijmakers and W. Vaatstra. A Higher Order Panel Method Applied to Vortex Sheet Roll-Up. *AIAA Journal*, Vol 21(No 4), April 1983.

[23] T. Hoshino. Hydrodynamic Analysis of Propellers in Steady Flow Using a Surface Panel Method. In *Proceedings of the Spring Meeting*, number 1–6. The Society of Naval Architects of Japan, May 1989.

[24] C-Y. Hsin. *Development and Analysis of Panel Method for Propellers in Unsteady Flow*. PhD thesis, Department of Ocean Engineering, MIT, September 1990.

[25] C-Y. Hsin, J.E. Kerwin, and S.A. Kinnas. A Panel Method for the Analysis of the Flow Around Highly Skewed Propellers. In *Proceedings of the Propellers/Shafting '91 Symposium*, pages 1–13 (paper No. 11), Virginia Beach, VA, September 1991. Soc. Naval Arch. & Marine Engnrs.

[26] D. Hummel and G. Redeker. Experimentelle Bestimmung der gebundene Wirbellinien sowie des Stromungs-Verlaufs in der Umgebung der Hinterkante eines Schlanken Deltaflugels. *Abh. Braunschweig, Wiss. Ges.*, Vol 22:pp 273–290, 1972.

[27] S.D. Jessup. *An Experimental Investigation of Viscous Aspects of Propeller Blade Flow*. PhD thesis, The Catholic University of America, 1989.

[28] F. T. Johnson and P. E. Rubbert. Advanced Panel-Type Influence Coefficient Methods Applied to Subsonic Flows. *AIAA Paper*, (No 75-50), 1975.

[29] F. T. Johnson, E. N. Tinoco, P. Lu, and M. A. Epton. Three-Dimensional Flow over Wings with Leading-Edge Vortex Separation. *AIAA Journal*, Vol 18(No 4):pp 367–380, 1980.

[30] O.A. Kandil. Computational Technique for Compressible Vortex Flows Past Wings at Large Incidence. *Journal of Aircraft*, Vol 22(No 9):pp 750–755, 1985.

[31] D. P. Keenan. *Marine Propellers in Unsteady Flow*. PhD thesis, M.I.T., Department of Ocean Engineering, May 1989.

[32] J.E. Kerwin. Flow Field Computation for Non-Cavitating and Cavitating Propellers. In *Proceedings of Fourteenth Symposium on Naval Hydrodynamics*, University of Michigan, Ann Arbor, August 1982.

[33] J.E. Kerwin, S.A. Kinnas, J.-T. Lee, and W-Z Shih. A Surface Panel Method for the Hydrodynamic Analysis of Ducted Propellers. *Trans. SNAME*, 95, 1987.

[34] S.A. Kinnas. A General Theory for the Coupling Between Thickness and Loading for Wings and Propellers. *Journal of Ship Research*, Vol 36(No 1):pp 59–68, March 1992.

[35] S.A. Kinnas and C-Y. Hsin. A Boundary Element Method for the Analysis of the Unsteady Flow Around Extreme Propeller Geometries. *AIAA Journal*, 30(3):688–696, March 1992.

[36] S.A. Kinnas, S. Pyo, C-Y. Hsin, and J.E. Kerwin. Numerical Modelling of Propeller Tip Flows. In *Proceedings of the Sixth International Conference on Numerical Ship Hydrodynamics*, 1993.

[37] R. Krasny. Computation of Vortex Sheet Roll-Up in the Trefftz plane. *Journal of Fluid Mechanics*, Vol 184:pp 123–155, 1987.

[38] D. Kuchemann and J. Weber. Vortex Motions. *ZAMM 45*, 457, 1965.

[39] K. Kuwahara. Numerical Study of Flow past an Inclined Flat Plate by an Inviscid Model. *Journal of Physical Society of Japan*, Vol 35(No 5):pp 1545–1551, November 1973.

[40] K. Kuwahara and H. Takami. Numerical Studies of Two Dimensional Vortex Motion by a System of Point Vortices. *Journal of Physical Society of Japan*, Vol 34:pp 247–253, January 1973.

[41] C.E. Lan. A Quasi Vortex-Lattice Method in Thin Wing Theory. *Journal of Aircraft*, vol. 11(No 9), 1974.

[42] J.-T. Lee. *A Potential Based Panel Method for The Analysis of Marine Propellers in Steady Flow.* PhD thesis, M.I.T., Department of Ocean Engineering, August 1987.

[43] N. Lee. *Evolution and Structure of Leading Edge Vortices over Slender Wings.* PhD thesis, Dept. of Aero. and Astro., MIT, March, 1991.

[44] K.W. Mangler and J. Weber. The Flow Field near the Center of a Roll-Up Vortex Sheet. *Journal of Fluid Mechanics*, Vol 30, 1967.

[45] H. D. Maniar. *A Three Dimensional Higher Order Panel Method.* PhD thesis, M.I.T. , Department of Ocean Engineering, June, 1995.

[46] B. Maskew. Subvortex Technique for the Close Approach to a Discretized Vortex Sheet. *Journal of Aircraft*, Vol 14:pp 188–193, Feburary 1977.

[47] B. Maskew. Prediction of Subsonic Aerodynamic Characteristics: A Case for Low-Order Panel Methods. *Journal of Aircraft*, Vol 19(No 2):pp 157–163, February 1982.

[48] B. Maskew and B.M. Rao. Calculation of Vortex Flows on Comlex Configurations. *ICAS Paper 82-6.2.3.*, 1982.

[49] K.W. McAlister and L.W. Carr. Water Tunnel Visualizations on Dynamic Stall. *Journal of Fluids Engineering*, Vol 101:pp 376–380, 1980.

[50] B.W. McCormick. On Vortex Produced By a Vortex Trailing From a Lifting Surface. *Journal of Basic Engineering*, pages 369–379, September 1962.

[51] B.W. McCormick. *A Study of the Minimum Pressure in a Trailing Vortex System*. PhD thesis, The Pennsylvania State University, June, 1954.

[52] M.F. McCranken and C.S. Peskin. A Vortex Method for Blood Flow Through Heart Valves. *J. Comp. Phy.*, Vol 35:pp 185–205, 1980.

[53] J.E. McCune and T.S. Tavares. Perspective: Unsteady Wing Theory – Kármán/Sears Legacy. *Transactions ASME*, Vol 115:pp 548–560, December 1993.

[54] K.S. Min. *Numerical and Experimental Methods for Prediction of Field Point Velocities around Propeller Blades*. PhD thesis, Department of Ocean Engineering, MIT, 1978.

[55] M. Mokry and W.J. Rainbird. Calculation of Vortex Sheet Roll-Up in a Rectangular Wind Tunnel. *Journal of Aircraft*, Vol 12:pp 750–752, September 1975.

[56] D.W. Moore. A Numerical Study of the Roll-Up of a Finite Vortex Sheet. *Journal of Fluid Mechanics*, Vol 63(No 2):pp 225–235, 1974.

[57] D.W. Moore. The Equation of Motion of a Vortex Layer of Small Thickness. *Stud. Appl. Math.*, Vol 58:pp 119–140, 1978.

[58] D.W. Moore. The Spontaneous Appearance of a Singularity in the Shape of an Evolving Vortex Sheet. In *Proceedings of the Royal Society of London,Series A*, volume 365, pages 105–119, 1979.

[59] L. Morino and C-C. Kuo. Subsonic Potential Aerodynamic for Complex Configurations : A General Theory. *AIAA Journal*, Vol 12(No 2):pp 191–197, February 1974.

[60] E.M. Murman and P.M. Stremel. A Vortex Wake Capturing Method for Potential Flow Calculations. *AIAA Paper*, (82-0947), 1982.

[61] M.G. Nagati, J.D. Iversen, and J.M. Vogel. Vortex Sheet Modeling with Curved High-Order Panels. *Journal of Aircraft*, Vol 24(No 11):pp 776–782, 1987.

[62] J.N. Newman. *Marine Hydrodynamics*. The MIT Press, Cambridge, Massachusetts, 1977.

[63] J.N. Newman. Distributions of Sources and Normal Dipoles Over a Quadrilateral Panel. *Journal of Engineering Mathematics*, Vol 20:pp 113–126, 1986.

[64] S. Pyo and S.A Kinnas. The Flow Adapted Grid (FLAG) Applied to the Analysis of Propeller Tip Flows. In *Proceedings of the Propellers/Shafting '94 Symposium*, pages 1–10 (paper No. 10), Virginia Beach, VA, September 20-21 1994. Soc. of Naval Arch. & Marine Engnrs.

[65] J. Rom, D. Almosnino, and R. Gordon. Method for the Calculation of the Non-Linear Aerodynamic Characteristics of Thick Wings and Bodies Including Symmetric Vortex Separation in Subsonic Flows. Technical Report No 437, Department of Aero. Eng., Technion, 1981.

[66] L. Rosenhead. The Formation of Vortices from a Surface of Discontinuity. In *Proceedings of the Royal Society of London,Series A*, volume 134, pages 170–192, 1931.

[67] N. Rott. Diffraction of a Weak Shock with Vortex Generation. *Journal of Fluid Mechanics*, Vol 1:pp 111–128, 1956.

[68] Z. Rusak, E. Wasserstrom, and A. Seginer. Numerical Calculation of Nonlinear Aerodynamics of Wing-Body Configurations. *AIAA Journal*, Vol 21(No 7):pp 929–936, 1983.

[69] T. Sarpkaya. An Inviscid Model of Two-Dimensional Vortex Shedding for Transient and Asymptotically Steady Separated Flow over an Inclined Flat Plate. *Journal of Fluid Mechanics*, Vol 68:pp 109–128, 1975.

[70] A. Schmucker and K. Gersten. Vortex Breakdown and its Control on Delta Wings. *Fluid Dynamics Research*, Vol 3:pp 268–272, 1988.

[71] F. Stern, B. Zhang, B. Chen, H. Kim, and S. Jessup. Computation of Viscous Marine Propulsor Blade and Wake Flow. In *Proceedings of Twentieth Symposium on Naval Hydrodynamics*, Santa Barbara, California, August 1994.

[72] E.O. Suciu and M. Morino. A Nonlinear Finite-Element Analysis of Wings in Steady Incompressible Flows with Wake Roll-Up. *AIAA Paper*, (No 76-64), 1976.

[73] M.H. Wang. Hub effects in propeller design and analysis. Technical Report No 85-12, Department of Ocean Engineering, MIT, May 1985.

[74] F.L. Westwater. Rolling Up of the Surface of Discontinuity Behind an Aerofoil of Finite Span. *Aeronautical Research Council, R & M*, (No 1962), 1935.